(12) INTERNATIONAL APPLICATION PUBLISHED UNDER THE PATENT COOPERATION TREATY (PCT)

(19) World Intellectual Property Organization
International Bureau

(43) International Publication Date
23 March 2017 (23.03.2017)

WIPO | PCT

(10) International Publication Number
WO 2017/048856 A1

(51) International Patent Classification:
A61B 5/00 (2006.01) *A61B 5/055* (2006.01)
A61B 6/03 (2006.01)

(21) International Application Number:
PCT/US2016/051755

(22) International Filing Date:
14 September 2016 (14.09.2016)

(25) Filing Language: English

(26) Publication Language: English

(30) Priority Data:
62/218,239 14 September 2015 (14.09.2015) US

(71) Applicant: **RENSSELAER POLYTECHNIC INSTITUTE** [US/US]; 110 8th Street, J Building, Troy, NY 12180 (US).

(72) Inventors: **WANG, Ge**; 20 Hilander Dr., Loudonville, NY 12211 (US). **XI, Yan**; 2101 Sousse Ave., Apt. 1C, Troy, NY 12180 (US). **CONG, Wenxiang**; 9 Keystone Ct., Albany, NY 12205 (US). **ZHAO, Jun**; 800 Dongchuan Road, Minhang District, Shanghai, 200240 (CN).

(74) Agents: **FRANK, Louis C.** et al.; Saliwanchik, Lloyd & Eisenschenk, PO Box 142950, Gainesville, FL 32614-2950 (US).

(81) Designated States *(unless otherwise indicated, for every kind of national protection available)*: AE, AG, AL, AM, AO, AT, AU, AZ, BA, BB, BG, BH, BN, BR, BW, BY, BZ, CA, CH, CL, CN, CO, CR, CU, CZ, DE, DK, DM, DO, DZ, EC, EE, EG, ES, FI, GB, GD, GE, GH, GM, GT, HN, HR, HU, ID, IL, IN, IR, IS, JP, KE, KG, KN, KP, KR, KW, KZ, LA, LC, LK, LR, LS, LU, LY, MA, MD, ME, MG, MK, MN, MW, MX, MY, MZ, NA, NG, NI, NO, NZ, OM, PA, PE, PG, PH, PL, PT, QA, RO, RS, RU, RW, SA, SC, SD, SE, SG, SK, SL, SM, ST, SV, SY, TH, TJ, TM, TN, TR, TT, TZ, UA, UG, US, UZ, VC, VN, ZA, ZM, ZW.

(84) Designated States *(unless otherwise indicated, for every kind of regional protection available)*: ARIPO (BW, GH, GM, KE, LR, LS, MW, MZ, NA, RW, SD, SL, ST, SZ, TZ, UG, ZM, ZW), Eurasian (AM, AZ, BY, KG, KZ, RU, TJ, TM), European (AL, AT, BE, BG, CH, CY, CZ, DE, DK, EE, ES, FI, FR, GB, GR, HR, HU, IE, IS, IT, LT, LU, LV, MC, MK, MT, NL, NO, PL, PT, RO, RS, SE, SI, SK, SM, TR), OAPI (BF, BJ, CF, CG, CI, CM, GA, GN, GQ, GW, KM, ML, MR, NE, SN, TD, TG).

Published:
— *with international search report (Art. 21(3))*

(54) Title: SIMULTANEOUS CT-MRI IMAGE RECONSTRUCTION

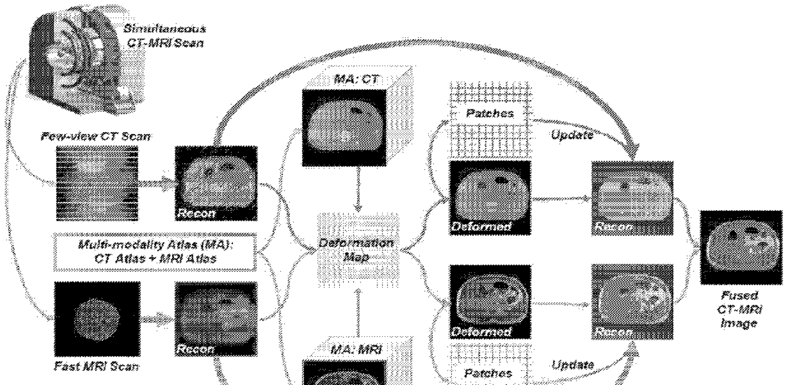

FIG. 21

(57) Abstract: Novel and advantageous systems and method for obtaining and/or reconstructing simultaneous computed tomography (CT) - magnetic resonance imaging (MRI) images are provided. Structural coupling (SC) and compressive sensing (CS) techniques can be combined to unify and improve CT and MRI reconstruction. A bidirectional image estimation method can be used to connect images from different modalities, with CT and MRI data serving as prior knowledge to each other to produce better CT and MRI image quality than would be realized with individual reconstruction.

WO 2017/048856 A1

DESCRIPTION

SIMULTANEOUS CT-MRI IMAGE RECONSTRUCTION

CROSS-REFERENCE TO A RELATED APPLICATION

This application claims the benefit of U.S. Provisional Application Serial No. 62/218,239, filed September 14, 2015, which is incorporated herein by reference in its entirety.

BACKGROUND

According to the National Center for Health Statistics, heart and oncologic diseases are the top two causes of mortality in the United States. Considerable strides have been made in imaging of these maladies with technologic innovations in computed tomography (CT), magnetic resonance imaging (MRI), single photon emission computed tomography / positron emission tomography (SPECT/PET), ultrasound, and optical imaging including optical coherence tomography (OCT) and fluorescence imaging. These imaging modalities are routinely used worldwide, producing critical tomographic information of the human body and enabling evaluation of not only anatomical and functional features but also cellular and molecular features in modern medicine. However, each individual imaging modality has its own contrast mechanism with strengths and weaknesses, and imaging protocols depend on many interrelated factors. Both individual (CT, MRI, PET, and SPECT) and hybrid modalities (PET/SPECT-CT and PET/MRI) are clinically accepted with strong evidence of healthcare benefits.

Prior to the availability of hybrid PET-CT, separate CT and PET scans were performed often with longer scanning time and poor anatomic localization of radionuclide uptake, due to post-acquisition image fusion errors. More recently, hybrid PET-CT has become an indispensable modality for cancer staging and assessing treatment response. Recent availability of hybrid PET-MRI goes a step further, providing both superior detection and characterization of abnormalities from MRI and metabolic information from PET. While PET provides critical functional information to PET-CT and PET-MRI, both CT and MRI help enhance PET information and enable better diagnostic performance.

Each tomographic modality has distinct advantages, including high temporal and spatial resolution with CT, excellent tissue characterization and nonionizing radiation with MRI; and high sensitivity for molecular imaging with SPECT or PET. However, no single modality is sufficient to depict the complex dynamics of mammalian physiology and pathology. As evidenced by SPECT-CT and PET-CT scanners, modality fusion imaging can be effective and synergistic and has had tremendous impact on both experimental discovery and clinical care. Even with current multi-modality imaging, though, limitations exist, including reconstruction techniques that are inefficient and/or inaccurate.

BRIEF SUMMARY

Embodiments of the subject invention provide novel and advantageous systems and method for obtaining and/or reconstructing simultaneous computed tomography (CT) - magnetic resonance imaging (MRI) images. Structural coupling (SC) and compressive sensing (CS) techniques can be combined to unify and improve CT and MRI reconstruction. A bidirectional image estimation method can be used to connect images from different modalities, with CT and MRI data serving as prior knowledge to each other to produce better CT and MRI image quality than would be realized with individual reconstruction.

In one embodiment, a method of reconstructing CT and MRI images can comprise: reconstructing a CT image from CT data; reconstructing an MRI image from MRI data; setting an iteration step to zero; transforming a CT-MRI dataset by the CT image and the MRI image; estimating the corresponded CT-MRI image according to the CT image and the MRI image aided by the CT-MRI dataset; reconstructing the CT image with the estimated CT-MRI image and the CT data; reconstructing the MRI image with the CT-MRI image and the MRI data; adding one to the iteration step; and repeating the steps between setting an iteration step to zero and adding one to the iteration step, until meeting stop criteria, at which point the current estimated reconstructed CT image is the reconstructed CT image and the current estimated reconstructed MRI image is the reconstructed MRI image.

In another embodiment, a system for simultaneous CT-MRI can comprise: a CT subsystem for obtaining CT data; an MRI subsystem for obtaining MRI data; at least one processor; and a machine-readable medium, in operable communication with the CT subsystem, the MRI subsystem, and the at least one processor, having machine-executable instructions stored thereon that, when executed by the at least one processor, perform a method of reconstructing CT and MRI images. The MRI subsystem can comprise superconducting magnets. Also, the method of reconstructing CT and MRI images can be such a method as described herein.

BRIEF DESCRIPTION OF THE DRAWINGS

Figure 1a shows a computed tomography (CT) image of a human abdomen, normalized into [0,1].

Figure 1b shows a magnetic resonance imaging (MRI) image of the human abdomen of Figure 1a, normalized into [0,1].

Figure 1c shows a line profile along the dotted line of Figure 1a.

Figure 1d shows a line profile along the dotted line of Figure 1b.

Figure 1e shows a joint histogram of Figures 1a and 1b.

Figure 2 shows structural coupling (SC) for image estimation.

Figure 3a shows a ground truth CT image (left), a ground truth MRI image (center), and a registration result image (right) for a modified NCAT phantom (mNCAT).

Figure 3b shows a ground truth CT image (left), a ground truth MRI image (center), and a registration result image (right) for a visible human project phantom (VHP).

Figure 3c shows a ground truth CT image (left), a ground truth MRI image (center), and a registration result image (right) for a porcine sample.

Figure 4 shows a diagram of examples of CT and MRI datasets deformation.

Figure 5a shows an image of a low magnetic field measurement in an MRI sub-system for mNCAT.

Figure 5b shows an image of a low magnetic field measurement in an MRI sub-system for VHP.

Figure 5c shows an image of a low magnetic field measurement in an MRI sub-system for a porcine sample.

Figure 6a shows a CT image for a mNCAT simulation, reconstructed using total variation (TV)-based reconstruction.

Figure 6b shows a CT image for a mNCAT simulation, reconstructed using simultaneous CT-MRI reconstruction according to an embodiment of the subject invention.

Figure 6c shows an MRI image for a mNCAT simulation, reconstructed using TV-based reconstruction.

Figure 6d shows an MRI image for a mNCAT simulation, reconstructed using simultaneous CT-MRI reconstruction according to an embodiment of the subject invention.

Figure 6e is an image of the residual error relative to ground truth for the reconstruction of Figure 6a.

Figure 6f is an image of the residual error relative to ground truth for the reconstruction of Figure 6b.

Figure 6g is an image of the residual error relative to ground truth for the reconstruction of Figure 6c.

Figure 6h is an image of the residual error relative to ground truth for the reconstruction of Figure 6d.

Figure 7a shows a plot of root-mean-square error (RMSE) with respect to patch size ($\sqrt{p_n}$) for simultaneous CT-MRI construction in a mNCAT experiment.

Figure 7b shows a plot of RMSE with respect to relaxation parameter (α) for simultaneous CT-MRI construction in a mNCAT experiment.

Figure 7c shows a plot of RMSE with respect to iteration index (k) for simultaneous CT-MRI construction in a mNCAT experiment.

Figure 8a shows a plot of RMSE with respect to various registration errors ($\Delta x, \Delta y$) for CT images in simultaneous CT-MRI construction in a mNCAT experiment.

Figure 8b shows a plot of RMSE with respect to various registration errors ($\Delta x, \Delta y$) for MRI images in simultaneous CT-MRI construction in a mNCAT experiment.

Figure 8c shows a plot of RMSE with respect to various noise levels for simultaneous CT-MRI construction (squares) and TV-based reconstruction ("x" data points) for CT images in a mNCAT experiment.

Figure 8d shows a plot of RMSE with respect to various noise levels for simultaneous CT-MRI construction (circles) and TV-based reconstruction ("x" data points) for MRI images in a mNCAT experiment.

Figure 9a shows a CT image for a VHP simulation, reconstructed using TV-based reconstruction.

Figure 9b shows a CT image for a VHP simulation, reconstructed using simultaneous CT-MRI reconstruction according to an embodiment of the subject invention.

Figure 9c shows an MRI image for a VHP simulation, reconstructed using TV-based reconstruction.

Figure 9d shows an MRI image for a VHP simulation, reconstructed using simultaneous CT-MRI reconstruction according to an embodiment of the subject invention.

Figure 9e is an image of the residual error relative to ground truth for the reconstruction of Figure 9a.

Figure 9f is an image of the residual error relative to ground truth for the reconstruction of Figure 9b.

Figure 9g is an image of the residual error relative to ground truth for the reconstruction of Figure 9c.

Figure 9h is an image of the residual error relative to ground truth for the reconstruction of Figure 9d.

Figure 10a shows a local enlarged view of a ground truth CT image for a VHP experiment.

Figure 10b shows a local enlarged view of a reconstructed CT image for a VHP experiment, reconstructed using TV-based reconstruction.

Figure 10c shows a local enlarged view of a reconstructed CT image for a VHP experiment, reconstructed using simultaneous CT-MRI reconstruction according to an embodiment of the subject invention.

Figure 10d shows a local enlarged view of a ground truth MRI image for a VHP experiment.

Figure 10e shows a local enlarged view of a reconstructed MRI image for a VHP experiment, reconstructed using TV-based reconstruction.

Figure 10f shows a local enlarged view of a reconstructed MRI image for a VHP experiment, reconstructed using simultaneous CT-MRI reconstruction according to an embodiment of the subject invention.

Figure 11a shows a plot of root-mean-square error (RMSE) with respect to patch size ($\sqrt{p_n}$) for simultaneous CT-MRI construction in a VHP experiment.

Figure 11b shows a plot of RMSE with respect to iteration index (k) for simultaneous CT-MRI construction in a VHP experiment.

Figure 12a shows a CT image for a porcine sample simulation, reconstructed using TV-based reconstruction.

Figure 12b shows a CT image for a porcine sample simulation, reconstructed using simultaneous CT-MRI reconstruction according to an embodiment of the subject invention.

Figure 12c shows an MRI image for a porcine sample simulation, reconstructed using TV-based reconstruction.

Figure 12d shows an MRI image for a porcine sample simulation, reconstructed using simultaneous CT-MRI reconstruction according to an embodiment of the subject invention.

Figure 12e is an image of the residual error relative to ground truth for the reconstruction of Figure 12a.

Figure 12f is an image of the residual error relative to ground truth for the reconstruction of Figure 12b.

Figure 12g is an image of the residual error relative to ground truth for the reconstruction of Figure 12c.

Figure 12h is an image of the residual error relative to ground truth for the reconstruction of Figure 12d.

Figure 13a shows a local enlarged view of a ground truth CT image for a porcine sample experiment.

Figure 13b shows a local enlarged view of a reconstructed CT image for a porcine sample experiment, reconstructed using TV-based reconstruction.

Figure 13c shows a local enlarged view of a reconstructed CT image for a porcine sample experiment, reconstructed using simultaneous CT-MRI reconstruction according to an embodiment of the subject invention.

Figure 13d shows a local enlarged view of a ground truth MRI image for a porcine sample experiment.

Figure 13e shows a local enlarged view of a reconstructed MRI image for a porcine sample experiment, reconstructed using TV-based reconstruction.

Figure 13f shows a local enlarged view of a reconstructed MRI image for a porcine sample experiment, reconstructed using simultaneous CT-MRI reconstruction according to an embodiment of the subject invention.

Figure 14a shows a plot of root-mean-square error (RMSE) with respect to patch size ($\sqrt{p_n}$) for simultaneous CT-MRI construction in a porcine sample experiment.

Figure 14b shows a plot of RMSE with respect to iteration index (k) for simultaneous CT-MRI construction in a porcine sample experiment.

Figure 15a shows a quantitative summary of the RMSE for mNCAT, VHP, and porcine sample experiments, for MRI results with compressive sensing (CS), MRI results with SC and CS, CT results with CS, and CT results with SC and CS.

Figure 15b shows a quantitative summary of the structural similarity index (SSIM) for mNCAT, VHP, and porcine sample experiments, for MRI results with CS, MRI results with SC and CS, CT results with CS, and CT results with SC and CS.

Figure 16a shows an image of a retrospective combination of a CT coronary angiography scan and a cardiac MRI scan.

Figure 16b shows an image of a retrospective combination of a CT coronary angiography scan and a cardiac MRI scan.

Figure 17a shows parametric images (apparent diffusion coefficient (ADC) and pharmacokinetic (PK)) derived from measured data.

Figure 17b shows comparison of the pretreatment baseline scan of Figure 17a with a single cycle of therapy.

Figure 18a shows a schematic view of traditional X-ray tomographic reconstruction.

Figure 18b shows a reconstructed image of a sheep chest from a complete dataset (region of interest (ROI) in the circle).

Figure 18c shows an image of a reconstructed image of the ROI of Figure 18b, using interior tomography.

Figure 19 shows a schematic view of a simultaneous CT-MRI scanner according to an embodiment of the subject invention.

Figure 20a shows a pair of donut-shaped magnets that can be used in a simultaneous CT-MRI scanner according to an embodiment of the subject invention.

Figure 20b shows a pair of hexagonal magnet arrays that can be used in a simultaneous CT-MRI scanner according to an embodiment of the subject invention.

Figure 21 shows a flowchart for simultaneous CT-MRI image reconstruction according to an embodiment of the subject invention.

Figure 22 shows images of an interior scan with 15 views.

Figure 23a shows a PET-CT scan of a transverse section of the carotid plaque from a 64-yr-old man.

Figure 23b shows a dynamic contrast enhanced (DCE) MRI scan of a transverse section of the carotid plaque from a 64-yr-old man.

Figure 23c shows a dynamic contrast enhanced (DCE) MRI scan of a transverse section of the carotid plaque from a 64-yr-old man.

Figure 23d shows a dynamic contrast enhanced (DCE) MRI scan of a transverse section of the carotid plaque from a 64-yr-old man.

DETAILED DESCRIPTION

Embodiments of the subject invention provide novel and advantageous systems and method for obtaining and/or reconstructing simultaneous computed tomography (CT) - magnetic resonance imaging (MRI) images. Structural coupling (SC) and compressive sensing (CS) techniques can be combined to unify and improve CT and MRI reconstruction. A bidirectional image estimation method can be used to connect images from different modalities, with CT and MRI data serving as prior knowledge to each other to produce better CT and MRI image quality than would be realized with individual reconstruction.

Despite recent advances, CT as an independent imaging modality is limited by the associated radiation burden and lack of tissue characterization, and MRI as an independent imaging modality is limited by its longer imaging time and low signals from aerated lungs and calcified and/or ossified structures. Synchronized CT-MRI can address the limitations of each imaging modality individually while improving the diagnostic content and abbreviating the imaging processes.

Multimodality imaging has major clinical advantages. While there can be different versions, CT technologies has generally gone from the first generation for translation–rotation in parallel-beam geometry to the latest generation with spiral/helical multi-slice/cone-beam scanning. Analogous to CT generations, the development of multimodality imaging technologies progressed from sequential acquisition to simultaneous positron emission tomography (PET)-CT and PET-MRI scanners. Integrated multimodality imaging systems such as PET-CT, single photon emission computed tomography (SPECT)-CT, and PET-MRI have gained acceptance as clinical and research tools after initial skepticism, but CT-MRI has greater technical challenges. In many cases (e.g., vascular structures, osseous constructs, and some features of soft tissues/organs with exogenous contrast), CT offers exquisite anatomic information at fine resolution with fast speed. With photon-counting detectors, it is feasible to obtain spectral or multi-energy CT images for material characterization that promises significantly better diagnostic performance than current dual-energy CT techniques.

On the other hand, MRI captures functional, flow-related, and tissue-specific signals with excellent contrast. By using superconducting magnets (e.g., room-temperature superconducting magnets), embodiments of the subject invention can use localized and inhomogeneous field-based MRI techniques for higher imaging flexibility. Also, new pulse sequences can be designed to produce even richer physiological and pathological information, highly complementary to that from CT. For example, nanoparticles can be functionalized to target different peptides and receptors, made to enhance features for both CT and MRI, and have great clinical potential. In many embodiments, a simultaneous CT-MRI scanner can provide a synergistic imaging tool to study intrinsic complexity and dynamic character of real biological and pathological processes in non-contrast/contrast-enhanced cardiovascular and oncologic applications.

In existing clinical imaging, the synchronization of CT and MRI is the only missing link among the three most popular tomographic modalities: CT, MRI, and PET/SPECT. The two principal technical difficulties for simultaneous CT-MRI in the related art are: (1) space constraints given the physical bulkiness of CT and MRI scanners; and (2) the electromagnetic interference between them. Embodiments of the subject invention can take advantage of enabling technology for simultaneous CT-MRI in the form of interior tomography theory and methods. Simultaneous CT-MRI can enable synergistic physiological and morphologic imaging applications for cardiac diseases, stroke, and cancer, offering unique information for diagnosis and therapy of many common but complicated diseases.

Omnitomography can be considered an ultimate form of modality fusion, and a simultaneous CT-MRI scanner can be considered a special case of omnitomography that combines high spatial resolution of CT with high contrast resolution of MRI (see also Wang et al., Towards omnitomography—Grand fusion of multiple modalities for simultaneous interior tomography," PloS One, vol. 7, p. e39700, 2012; which is hereby incorporated by reference herein in its entirety). The advantages of merging tomographic imaging modalities can go beyond complementary attributes, potentially improving results for any individual modality and providing promise for improved functional imaging studies and radiation therapy.

Figures 16a and 16b show two retrospective combinations of a CT coronary angiography scan and a cardiac MRI scan. Referring to Figure 16a, a fused surface rendering of the segmented coronary artery tree from low-dose CT with the mask representing the myocardium of the left ventricle and the segmented data from late gadolinium enhancement (LGE) are shown. Lateral LGE can be assigned to a high grade stenosis (indicated by the arrow in Figure 16a) of the obtuse marginal (OM) branch of the circumflex artery (CX). The extent of transmurality of LGE can be displayed in a color-coded fashion. No stenosis can be seen in the segmented left anterior descending (LAD) artery and proximal CX. Referring to Figure 16b, segmented myocardial defects from cardiac MRI are integrated with a volume rendering based on low-dose CT. Low-dose CT can demonstrate the LAD and OM branch of circumflex artery and significant stenosis (indicated by arrow in Figure 16b) of the first diagonal branch (D1). The fused images show an anterolateral perfusion deficit (indicated by the asterisk in Figure 16b) in relation to the D1 stenosis (arrow). Figures 16a and 16b are adapted from Donati et al. (3D fusion of functional cardiac magnetic resonance imaging and computed tomography coronary angiography: Accuracy and added clinical value, Invest. Radiol. 46, 331–340, 2011), which is hereby incorporated by reference herein in its entirety.

Simultaneous CT-MRI has the potential to change the care of patients with cardiac diseases by allowing each modality to use its strengths to address the limitations of the other. Noninvasive identification and localization of vulnerable plaques may be optimally performed with synchronized CT (superior temporal and spatial resolution) and MRI (superior tissue contrast) scanning, which can substantially change prophylactic treatment of patients with vulnerable plaques. With simultaneous acquisition, CT can exclude significant coronary artery disease while synchronized MRI can assess plaque composition and myocardial function. In addition, simultaneous CT-MRI may have a crucial role in acute stroke. The window of opportunity is short to treat a patient with acute stroke, typically between three and six hours from the onset of symptoms. Simultaneous CT and MRI can help determine eligibility of the patient to receive thrombolytic therapy and recover or limit loss of neurological functions.

Simultaneous CT-MRI also has the potential to enrich information from dynamic contrast-enhanced (DCE) studies by cross calibrating each modality and coupling dynamic features. This can enable routine evaluation of sophisticated tumor perfusion metrics, which will help in tumor characterization and therapeutic assessment. Combined imaging modalities frequently use contrast agents - radiopharmaceuticals, intravascular agents, and multifunctional nanoparticles - to expand their capabilities. Because conventional CT and MRI use different dedicated agents, the potential for multifunctional CT-MRI nanoparticles is particularly important.

Figure 17a shows parametric images (apparent diffusion coefficient (ADC) and pharmacokinetic (PK)) derived from measured data, and Figure 17b shows comparison of the pretreatment baseline scan of Figure 17a with a single cycle of therapy.

Referring to Figure 17a, ADC was computed from pre-contrast diffusion weighted MRI images, and dynamic contrast enhanced (DCE)-PK from PK compartmental modeling coefficients determined using a temporal sequence of pre- and post-contrast images. The kinetic model is known and not shown. Referring to Figure 17b, the tumor displayed mostly high permeability red voxels before treatment and mostly green voxels (decreasing permeability and increasing extravascular fraction (EVF)) after treatment. The response to therapy is also depicted in the joint histograms at the right side of Figure 17b - baseline above and "after 1 cycle" below. The color scale shows benign characteristics of DCE response in blue and malignant response in yellow red. The axes include EVF (abscissa) versus reciprocal permeability (ordinate). The results show major changes between baseline and therapy, indicating that the response to therapy can be known using parametric images long before morphologic changes, such as change in tumor size, may be detected. Figures 17a and 17b are reproduced from Jacobs et al. (Multiparametric and multimodality functional radiological imaging for breast cancer diagnosis and early treatment response assessment, J. Natl. Cancer Inst. Monogr. 2015, 40–46; see also the "References" section).

Multimodality imaging may be required for effective multimodality therapy, and modality integration can facilitate the principal tasks including target definition, treatment planning, verification, and monitoring. The advantage to acquiring CT and MRI data simultaneously during dynamic contrast enhancement comes from the fact that both modalities provide contrast kinetic parameters, but the assumptions, intrinsic errors, and limitations of the modeling processes are quite different and hence potentially synergistic. Therefore, better characterization of the imaged tissues may become available once simultaneously imaged.

While CT and MRI are the two most utilized tomographic modalities, their physical combination has not been attempted in a clinical setting. A CT scanner works with high-speed rotating metallic parts including at least one X-ray tube and a detector assembly. An MRI scanner relies on high-strength and high-frequency magnetic fields. The combination of the CT and MRI scanners is made challenging at least by the geometric constraints and electromagnetic interference. Interior tomography is a key strategy to overcome both in simultaneous CT-MRI, along with X-ray radiation dose reduction.

Interior tomography is a unique feature of simultaneous CT-MRI. The classic strategy in the CT field has been that a whole cross section must be completely covered by a fan- or cone-beam of X-rays, and resultant measures must be transformed into sufficient radon (line or planar integral) data, or equivalently the Fourier space must be fully sampled for accurate and reliable image reconstruction. However, biomedical applications often focus on a region of interest (ROI), for example, a cardiac chamber, a tumor mass, and/or a surgical region. Therefore, data truncation for theoretically exact tomographic quantification can be useful.

Mathematically speaking, cone-beam spiral CT reconstruction is essentially handling longitudinal data truncation complicated by the divergence of X-rays. Orthogonal to the longitudinal data truncation is the transverse data truncation problem. The conventional fan-beam scanning involves no data truncation. On the other hand, the interior problem is associated with a narrow scanning beam. Only X-rays that go through an interior ROI are used to generate truncated projection data, as shown in Figure 18a. This interior problem has no unique solution, but if there is a known subregion in the ROI, the interior problem can be uniquely and stably solved. The assumption of a known subregion is practical such as air in an airway or blood in an aorta. However, once contrast material is injected for cardiac CT, blood density cannot be assumed as known. If the attenuation coefficients in a ROI can be well approximated by a piecewise constant/polynomial function, the solution to the interior problem is unique. For a piecewise polynomial ROI the solution to the interior problem is not only unique but also stable. Interior tomography produces excellent local reconstruction in practice, as shown in Figures 18b and 18c.

Figure 18a shows a schematic view of traditional X-ray tomographic reconstruction; Figure 18b shows a reconstructed image of a sheep chest from a complete dataset (region of interest (ROI) in the circle); and Figure 18c shows an image of a reconstructed image of the ROI of Figure 18b, using interior tomography (Wang et al., Can interior tomography outperform lambda tomography?, Proc. Natl. Acad. Sci. U. S. A. 107, E92–E93, 2010; see also the “References” section). Referring to Figure 18a, an internal region (the red disk on the left) can be reconstructed from truncated data (the red (innermost) rectangle on the right), and, in principle, line integrals along paths not directly involving the local region (the green (outer) rectangles on the right) can be irrelevant. Traditional X-ray tomographic reconstruction can be theoretically exact or very accurate if all the data are precisely acquired along paths through an object support.

Based on X-ray interior tomography results, it can be the case that accurate and reliable local image reconstruction only needs indirect measurement that directly involves a ROI. Indeed, this is theoretically valid for other medical imaging modalities. For interior MRI, the requirement of the background magnetic field can be relaxed. In contrast to the popular concept that a homogeneous background magnetic field large enough to contain a whole cross section through a patient is needed, a much smaller homogeneous background magnetic field can be used. Then, focused RF excitation and truly interior algorithms can be used for image reconstruction. Interior MRI with an inhomogeneous field can also be used. With interior tomography, CT and MRI systems can be made compact to provide space for coexistence and facilitate shielding for seamless integration.

In many embodiments, a unified reconstruction framework can be used for simultaneous and integrated CT-MRI image reconstruction. Structural coupling (SC) and compressive sensing (CS) techniques can be combined to unify and improve CT and MRI reconstruction. In some embodiments, a bidirectional image estimation method can be used to connect images from different modalities. CT and MRI data can serve as prior knowledge to each other to produce better CT and MRI image quality than would be realized with individual reconstruction. The SC method is similar to dictionary learning (DL), yet the former is more efficient and flexible than the latter for modality fusion imaging and content-based image estimation (see also Xi et al., United iterative reconstruction for spectral computed tomography, IEEE Trans. Med. Imag., vol. 34, no. 3, pp. 769–778, Mar. 2015; and Xi et al., A hybrid CT-MRI reconstruction method, presented at the IEEE Int. Symp. Biomedical Imaging, Beijing, China, 2014; both of which are incorporated by reference herein in their entireties). SC is based on local features and establishes a connection between different modality images via a table of paired image patches.

Figure 19 shows a schematic view of a simultaneous CT-MRI scanner according to an embodiment of the subject invention, including a breakdown of components and some possible dimensions. With the use of superconducting magnets, the clinical magnetic field strength can be achieved for uncompromised MRI performance (see also, Wang et al., Toplevel design of the first CT-MRI scanner, in Proceedings of The 12th International Meeting on Fully Three-Dimensional Image Reconstruction in Radiology and Nuclear Medicine, 2013, pp. 150–153; which is hereby incorporated by reference herein in its entirety). Though dimensions are shown in Figure 19, these are for exemplary purposes only and should not be construed as limiting.

Based on the interior tomography oriented design, the peripheral magnetic field can be decreased rapidly (<0.5 Tesla) so as not to interfere with CT components significantly, and the static/quasistatic CT data acquisition system may not impose any substantial interference to the MRI process. Therefore, MRI image distortion may not be a problem in principle. To address conflicting space requirements by CT and MRI as well as suppress electromagnetic interference between CT and MRI for a simultaneous CT-MRI scanner, both CT and MRI can first be interiorized. A stationary multisource CT architecture with X-rays targeting a ROI can be used. Because the CT components stand still during data acquisition, the electromagnetic shielding can be greatly simplified. The physical complications can be handled using the same or similar techniques developed for X-ray/MRI. Correlation between CT and MRI datasets can be utilized to improve image quality. Superconducting design can be capable of offering clinically useful CT and MRI performance metrics.

In an embodiment, the CT-MRI instrumentation can target a relatively centralized ROI. Then, the extension from a centralized to a peripheral ROI can be attempted. There are multiple schemes to achieve this versatility. For example, a transversely elongated field of view could be used to accommodate the patient placement. Also, a local magnetic field can be developed that can be deflected using a superconducting technology and an adaptive X-ray beam collimation. Also, the CT setup can be either quasi-stationary or stationary. While the design in Figure 19 is feasible to rotate X-ray imaging chains slightly between MRI acquisitions to cover more projection angles (as indicated by the belt in the bottom-right portion of Figure 19), the heart motion can be utilized via biomechanical modeling and deformable matching based imaging in the ideal case of a stationary gantry with the sinogram limited to few views (e.g., 10 views or less).

Figure 20a shows a pair of donut-shaped magnets that can be used in a simultaneous CT-MRI scanner according to an embodiment of the subject invention. Also, Figure 20b shows a pair of hexagonal magnet arrays that can be used in a simultaneous CT-MRI scanner according to an alternative embodiment of the subject invention. In each of Figures 20a and 20b, the left side shows a 3-dimensional perspective view, the center section shows a cross-sectional side view, and the right side shows a top view. Though dimensions are shown in Figures 20a and 20b, these are for exemplary purposes only and should not be construed as limiting.

In a more cost-effective approach, permanent magnets can be used to replace superconducting magnets for simultaneous CT-MRI (e.g., in the designs shown in Figures 20a and 20b). The material for permanent magnets can be, for example, NdFeB (e.g., NdFeB 45 MGOe sintered). Referring again to Figure 20a, a pair of donut-shaped permanent magnets can form a regionally uniform magnetic field (e.g., of about 0.35 T) and leave room for a CT gantry. The imaging parameters can include, for example, about 10 centimeters (cm) field of view, about 0.5 millimeters (mm) CT and MRI resolution (MRI resolution can be presumably enhanced with the associated CT data), and 1 CT-MRI scan/s in a continuous working mode (i.e., to be able to deliver hybrid images over a ROI or a volume of interest (VOI) every second). Electromagnetic interfering CT and MRI components can be easily shielded, which would otherwise be susceptible to electromagnetic interference. To construct a cost-effective background magnetic field, Halbach technology can be used in collaboration with low-field magnetic imaging. Referring again to Figure 20b, a pair of hexagonal rings can be used to accommodate a patient and provide a gap for CT hardware. The hexagonal design can yield a magnetic field of, for example, about 0.3 T between the ring arrays. With appropriate shielding, shimming, and further refinements, the homogeneous field strength around the center of the magnet arrays can be brought up to about 0.5 T or more. The permanent magnets in any design can be upgraded to superconducting counterparts, for example, with a magnetic field of 1.5-3 T or more.

In an embodiment, an edge-guided dual-modality image reconstruction approach can be used. The key can be to establish a knowledge-based connection between the datasets in four steps: (1) image segmentation; (2) image initialization; (3) CT reconstruction; and (4) MRI reconstruction. One imaging modality can be significantly helped by the other imaging modality, even with highly under-sampled data. Generally speaking, such a synergistic CT-MRI reconstruction can be clinically beneficial. First, CT image noise and radiation dose can be reduced with correlative MRI data. Also, MRI spatial and temporal resolution may be improved with CT data. Furthermore, while CT-based motion mapping guides MRI reconstruction, MRI tagging information refines CT motion estimation.

Figure 21 shows a flowchart for simultaneous CT-MRI image reconstruction according to an embodiment of the subject invention. Referring to Figure 21, in an embodiment, a pair of co-registered CT and MRI atlases can be used to aid in the reconstruction process. Prior knowledge of CT and/or MRI results and inter-modality synergy can be utilized for reduced noise and biases. Multiple iterative loops can be performed.

Referring again to Figure 21, in an embodiment, the overall framework for joint CT-MRI image reconstruction (or general multimodality image reconstruction) can be to perform image estimation for each modality based on a current scan and a corresponding high-quality atlas. For this purpose, a unified deformation map can be jointly constructed from CT and MRI scans as well as CT and MRI atlases. With this deformation map, estimated CT and MRI images can be generated as prior knowledge. Other image estimation methods can also be possible. For example, a CT image (or a MRI image) can be estimated from the corresponding high-quality MRI (or CT) image using a CT-MRI atlas. In this case, with the high-quality MRI image, a displacement field can be computed to deform an MRI image in the atlas into the target MRI image. Then, the same displacement field can be applied to deform the corresponding CT image in the atlas into an estimated CT image. Similarly, an MRI image can be estimated from a given target CT image. These estimated images can be used to regularize the joint CT-MRI image reconstruction. One of these powerful techniques is locally linear embedding (LLE), which can be adapted to reduce image noise or bias. According to LLE theory, each image patch from an imaging modality can be linearly represented in terms of nearby K most-similar patches (which is in the same spirit of known nonlocal mean methods but can capture more structural information). For example, it is feasible to find a LLE at any anatomical location for a deformed MRI image from the atlas. Then, this LLE for the deformed atlas image can be applied to a current MRI image as a noise/bias filter. Similarly, a current CT image can be improved via LLE. Although Figure 21 shows global joint CT-MRI reconstruction, joint interior CT-MRI reconstruction can be done as long as interior CT and interior MRI algorithms replace the corresponding global reconstruction algorithms. In the case of an interior CT-MRI scan, an individualized patient surface contour can be captured using an optical imager for the associated atlas deformation.

Estimated CT and MRI images, as well as atlas-based embedding structures can be all incorporated into a single object function to facilitate a unified CT-MRI reconstruction.

In the case of cardiac imaging, both CT and MRI images should be used to meet demanding requirements for spatial, contrast, and temporal resolutions. However, there is a conflict between a stationary CT architecture and sufficient projections through a cardiac ROI. In other words, about 10 projections can acquired in parallel without mechanical motion of the CT subsystem, but this limited number of projections is generally not enough for excellent image quality. This challenge can be addressed by utilizing cardiac motion itself. Specifically, ventricular torsion can be taken advantage of to increase the number of X-ray projections of the stationary multisource CT subsystem. Left ventricular (LV) torsion refers to myocardial motion and deformation during systole and diastole. The cardiac myocytes are arranged in a spiral network from the apex to the base. As they contract during systole, the heart undergoes a twisting motion, which is largely due to opposite rotational contractions in the base and apex. Echo-tracking ultrasound imaging has shown rotation angles of $7.96^{\circ}\pm1.57^{\circ}$ and $9.49^{\circ}\pm1.71^{\circ}$ in the base and apex, respectively. ECG-gated acquisition protocols and/or tagged MRI would allow for sophisticated cardiac biomechanical modeling and model based image reconstruction that is equivalent to use of an increased number of views of the heart. This torsion is more complicated than a simple rotation as there are some linear displacements during a cardiac cycle. Nonetheless, an accurate and real-time depiction of the heart at any single time point can be obtained with imaging techniques as described herein.

A CT-MRI scanner can acquire MRI and CT measurements of the subject simultaneously. CT and MRI subsystems can be seamlessly integrated for local reconstruction, enabled by the generalized interior tomography principle (see also

Wang et al., The meaning of interior tomography, Phys. Med. Biol., vol. 58, pp. R161–R181, 2013; which is hereby incorporated by reference herein in its entirety). The CT components can be made quasi-stationary with X-ray sources and detectors distributed face-to-face along a circle to overcome space limitations and electromagnetic interference. Given the geometrical constraints, the number of X-ray sources may be limited and can represent a "few-view" reconstruction problem. A pair of magnets or magnet arrays can be used to define a relatively small homogeneous magnetic field in the gap between the magnets or magnet arrays for the MRI subsystem; this, in combination with open configuration, allows room for the CT subsystem. The pair of magnet or magnet arrays can be, for example, donut-shaped or hexagonal, though embodiments are not limited thereto (see also Figures 20a and 20b).

In an embodiment of a CT-MRI scanner, the CT imaging process can be the same as for the current commercial CT systems except that the X-ray sources are fixed during a scan, but they could be rotated between scans if needed. Hence, the CT imaging model can be expressed as

$$\mathbf{M}\mathbf{u}_{CT} = \mathbf{f} \qquad (1)$$

where $\mathbf{u}_{CT}$ describes an object to be imaged in terms of linear attenuation coefficients, **M** is a system matrix, and **f** is line integral data after preprocessing.

In the MRI subsystem, the imaging model can also be similar to the conventional model, expressed as

$$\mathbf{R}\mathbf{F}\mathbf{u}_{MRI} = \mathbf{g} \qquad (2)$$

where $\mathbf{u}_{MRI}$ describes the same object but in terms of MRI parameters related to T1, T2, proton density, etc. **F** denotes the Fourier transform, **R** is a sampling mask in the k-space, and **g** is data.

In the CT-MRI scanner, CT and MRI data can be spatially and temporally registered. Alternatively, separately acquired CT and MRI scans can be fused to simulate a simultaneous acquisition. This CT-MRI duality is the base of many embodiments of the simultaneous CT-MRI image reconstruction strategy described herein.

Given appropriate spatial and temporal co-registration of CT and MRI images, their features can be physically correlated despite their inherently different imaging characteristics. The physical correlation and image compressibility can be collectively utilized via CS, for example, using the PRISM method which was adapted for various applications (Wang et al., Towards omni-tomography—Grand fusion of multiple modalities for simultaneous interior tomography, PloS One, vol. 7, p. e39700, 2012). However, PRISM and similar CS methods capture correlation as low rank characteristics that are rather general but not very specific. Most other known methods cannot address the joint image reconstruction problem over imaging modalities. Embodiments of the subject invention can use SC to reflect local similarity more specifically and more effectively for joint multimodality image reconstruction.

Figures 1a and 1b show a CT image and an MRI image of a human abdomen, respectively, both normalized into [0,1]. Figures 1c and 1d show line profiles along the dotted line of Figure 1a and the dotted line of Figure 1b, respectively, and Figure 1e shows a joint histogram of Figures 1a and 1b. Referring to Figures 1a-1e, the reconstructed pixel values are not well correlated, as suggested by Figures 1c-1e. Nevertheless, their structural boundaries are quite consistent, and different human beings share very similar anatomic structures.

A principal concept for utilization of CT-MRI image correlation is to pair their local structures in intrinsic corresponding relations, which is a natural coupling of relevant image features. In many embodiments, the connection between CT and MRI image features is maintained in paired CT-MRI patches. They can be generated from one-to-one corresponding CT and MRI image datasets. Given such a CT-MRI dataset, one-to-one corresponding patches can be extracted.

First, prior CT and MRI images can be deformed according to currently reconstructed CT and MRI images. The deformed CT-MRI images can be much closer to target CT and MRI images under reconstruction. This step will be further described herein.

Next, bidirectional CT and MRI image estimations can be performed using the SC method. The SC method is inspired by the locally linear embedding (LLE) theory, in which each data point in a high-dimensional space can be linearly represented in terms of the surrounding data points (see also Roweis et al., "Nonlinear dimensionality reduction by locally linear embedding, Science, vol. 290, pp. 2323–2326, 2000; which is hereby incorporated by reference herein in its entirety). Specifically, in the SC method, each patch is treated as a point in a high-dimensional space. Any patch $\mathbf{p}_*$ in given images can be linearly expressed with its similar patches $\mathbf{p}_{*,i}$. Involved weights $\{w_{*,i}\}$ can be determined by a Gaussian function, similar to those used in the nonlocal mean filtering:

$$w'_{*,i} = \exp\left(-\|\mathbf{p}_* - \mathbf{p}_{*,i}\|_2^2 / h^2\right) \text{ and } w_{*,i} = w'_{*,i} / \sum_i^K w'_{*,i} \quad (3)$$
,

where h is an empirical value that controls contributions of involved patches, and K is the number of surrounding data points.

The fundamental principle of the SC method of embodiments is based on the LLE theory, and the corresponded CT image patch $\mathbf{p}_{\text{CT}}$ can be linearly approximated with the associated patches in CT dataset $\mathbf{T}_{\text{CT}}$ and the same weighting factors $\{w_i\}$, formulated as $\mathbf{p}_{\text{CT}}$, and $\approx \sum_i^K w_i\, \mathbf{p}_{\text{CT},i}$, $\mathbf{p}_{\text{CT},i} \in \text{T}_{\text{CT}}$, and $\mathbf{p}_{\text{CT},i} \neq \mathbf{p}_{\text{CT}}$, as that for $\mathbf{p}_{\text{MRI}}$ in MRI dataset $\mathbf{T}_{\text{MRI}}$. Thus, with the weights $\{w_{*,i}\}$ and the one-to-one correspondence in extracted patch pairs, CT and MRI images are correlated. To implement bidirectional CT and MRI image estimations, a selection vector β_i can be applied to both CT and MRI datasets

$$\min_{\beta_i} \left\| p_{\text{MRI}} - \sum_i w_i T_{\text{MRI}} \beta_i \right\|_2^2 + \left\| p_{\text{CT}} - \sum_i w_i T_{\text{CT}} \beta_i \right\|_2^2 \quad (4)$$
,

where w_i equals the average of CT and MRI weightings calculated according to Equation (3), $w_i = (w_{\text{CT},i} + w_{\text{MRI},i})/2$, β_i identifies surrounding high-dimensional data points. Thus, CT and MRI patches are linked based on prior CT-MRI datasets by sharing the same selection vector and weights. Given a CT image, its corresponding MRI image can be predicted based on prior CTMRI patches and representation weights. The same scheme can be also applied on the mapping from MRI image to CT image. Here, the optimization of Equation (4) is empirically implemented: first, find ten K-nearest data points in CT and MRI spaces; then, compute the objective function – Equation (4) - with the first step results; and finally, choose CT and MRI patches for the minimum value of Equation (4).

The SC method of embodiments utilizes the fact that a corresponding CT patch and MRI patch are correlated via $\mathbf{T}_{\text{CT-MRI}}$ in terms of patch pairs. This principle has been demonstrated to be valid in (see, e.g., the examples). An example of the random tests is demonstrated in Figure 2, where given an MRI patch $\mathbf{p}_{\text{MRI}}$ the corresponding CT patch $\mathbf{p}\frac{\text{est}}{\text{CT}}$ can be estimated using a pre-trained image pair table $\mathbf{T}_{\text{CT-MRI}}$, and the resultant $\mathbf{p}\frac{\text{est}}{\text{CT}}$ is very close to the true CT patch $\mathbf{p}\frac{\text{true}}{\text{CT}}$. Figure 3 shows the estimation results using the SC method from given MRI images. The ground truth CT images and input MRI images are in the first and second columns, respectively.

In detail, Figure 2 shows SC for image estimation. Referring to Figure 2, any given MRI patch $\mathbf{p}_{MRI}$ can be linearly represented with similar patches in $\mathbf{T}_{MRI}$. Then, the corresponding CT patch $\mathbf{p}_{CT}$ can be linearly represented by the corresponding patches in $\mathbf{T}_{CT}$ with the same weighting factors $\{w_i\}$ as used for representing $\mathbf{p}_{MRI}$.

Figure 3a shows a ground truth CT image (left), a ground truth MRI image (center), and a registration result image (right) for a modified NCAT phantom (mNCAT). Figure 3b shows a ground truth CT image (left), a ground truth MRI image (center), and a registration result image (right) for a visible human project phantom (VHP). Figure 3c shows a ground truth CT image (left), a ground truth MRI image (center), and a registration result image (right) for a porcine sample.

It should be noted that weighting factors $\{w_i\}$ defined in Equation (3), and used in Equation (4) are not the same results as that obtained by the classic LLE theory. One advantage of the methods described herein is that they measure weight by the Euclidean distance from the reference patch $\mathbf{p}_{\text{MRI}}$, and guarantee that $\{w_i\}$ is positive and in a proper range. In the CT-MRI reconstruction methods of many embodiments of the subject invention, Equation (4) plays a key role in bidirectional image estimation by sharing the same selection vector β_i and $\{w_i\}$ determined from both MRI and CT sides.

CS has been proven effective for most tomographic modalities. CS theory seeks a “sparse” solution for an underdetermined linear system. Total variation (TV) is a widely used sparsifying transformation for CS-based CT and MRI reconstruction (see also Rudin et al., Nonlinear total variation based noise removal algorithms, Phys. D, Nonlinear Phenom., vol. 60, pp. 259–268, 1992; and Chambolle, An algorithm for total variation minimization and applications, J. Math. Imag. Vis., vol. 20, pp. 89–97, 2004;

both of which are hereby incorporated by reference herein in their entireties). The TV based CT and MRI reconstruction algorithms are, respectively, written as

$$\min_{\mathbf{u}_{CT}} \|\mathbf{u}_{CT}\|_{TV} \text{ s.t.} \mathbf{M}\mathbf{u}_{CT} = \mathbf{f} \quad (5)$$

and

$$\min_{\mathbf{u}_{MRI}} \|\mathbf{u}_{MRI}\|_{TV} \text{ s.t.} \mathbf{R}\mathbf{F}\mathbf{u}_{MRI} = \mathbf{g} \quad (6)$$

,

where $\|\cdot\|_{TV}$ represents the TV transformation.

In simultaneous CT-MRI reconstruction, CT and MRI datasets can be assumed to be spatially and temporally registered. These datasets can be separately reconstructed, and then combined. Intuitively, a joint CT-MRI image reconstruction framework should offer significantly better image quality than individual reconstructions because there are substantial correlations and complementary features between CT and MRI images.

There are two main steps in the simultaneous CT-MRI reconstruction according to many embodiments of the subject invention: patch-based image estimation; and guided image reconstruction. They can be iteratively and alternatively performed. The image reconstruction can first be started with regular CS-based CT and MRI reconstructions as suggested in Equations (5) and (6). Then, in the image estimation step, the reconstructed CT and MRI images can be set as the basis to predict their MRI and CT counterparts with the SC method. In the reconstruction step, the estimated CT and MRI results can be used to guide CT and MRI reconstructions, respectively. Thus, individual CT and MRI reconstructions can be linked together to guide the composite reconstruction synergistically.

In the image reconstruction, prior CT-MRI image patches can serve as a bridge to connect the two modalities. The SC method can perform the mapping between reconstructed CT and MRI images. In the SC method, prior CT and MRI datasets can first be deformed according to the given reconstructed CT and MRI images, as shown in Figure 4. The newly deformed CT-MRI datasets can be much closer to target CT and MRI images in reconstruction. Then, corresponding image patches can be extracted from the deformed prior CT and MRI datasets. Subsequently, both reconstructed CT and MRI images can be decomposed into patches and updated according to the paired image patches that share the same weighting factors $\{w_i\}$ and the same selection vector β_i in the deformed table $\mathbf{T}_{\mathrm{CT-MRI}}$. This process can be performed by finding the most similar patches and refining intermediate image patches via linear embedding, as described above. In the guided image reconstruction, estimated CT and MRI images, which can be based on previously reconstructed MRI and CT images, can be used to regularize their images in each individual modality reconstruction. They can be written as

$$\min_{\mathbf{u}_{CT}} (1-\alpha)\left\|\mathbf{u}_{CT}\right\|_{TV} + \alpha\left\|\mathbf{u}_{CT} - \mathbf{u}_{CT}^{est}\right\|_{TV} \ \text{s.t.}\ \mathbf{M}\mathbf{u}_{CT} = \mathbf{f} \tag{7}$$

and

$$\min_{\mathbf{u}_{MRI}} (1-\alpha)\left\|\mathbf{u}_{MRI}\right\|_{TV} + \alpha\left\|\mathbf{u}_{MRI} - \mathbf{u}_{MRI}^{est}\right\|_{TV} \ \text{s.t.}\ \mathbf{F}\mathbf{u}_{MRI} = \mathbf{g} \tag{8}$$

,

where $\mathbf{u}\frac{\mathrm{est}}{\mathrm{CT}}$ and $\mathbf{u}\frac{\mathrm{est}}{\mathrm{MRI}}$ are estimated images using the SC method according to the corresponding CT and MRI images. Equations (7) and (8) are well-posed convex optimization problems and can be effectively solved using the Split–Bregman method (see also Xi et al., United iterative reconstruction for spectral computed tomography, IEEE Trans. Med. Imag., vol. 34, no. 3, pp. 769–778, Mar. 2015; and Goldstein et al., The split Bregman method for L1-regularized problems, SIAM J. Imag. Sci., vol. 2, pp. 323–343, 2009; both of which are hereby incorporated herein by reference in their entireties).

TABLE I
WORKFLOW FOR SIMULTANEOUS CT-MRI IMAGE RECONSTRUCTION

Inputs	CT projection data f and MRI k-space data g
Reconstruction:	1. Reconstruct a CT image $\mathbf{u}_{CT}$ from f by (5); 2. Reconstruct an MRI image $\mathbf{u}_{MRI}$ from g by (6); 3. $k = 0$; 4. Loop until meeting the stop criteria 5. Transform CT-MRI datasets $\mathbf{T}_{CT-MRI}$ by given $\mathbf{u}_{MRI}$ and $\mathbf{u}_{CT}$; 6. Estimate the corresponded CT-MRI image $\mathbf{u}_{CT}^{est}$ and $\mathbf{u}_{MRI}^{est}$ according to $\mathbf{u}_{MRI}$ $\mathbf{u}_{CT}$ aided by $\mathbf{T}_{CT-MRI}$ using the SC method (see Table II); 7. Reconstruct the CT image with $\mathbf{u}_{CT}^{est}$ and f by (7); 8. Reconstruct the MRI image with $\mathbf{u}_{MRI}^{est}$ and g by (8); 9. $k = k + 1$; 10. end

Overall, the simultaneous CT-MRI image reconstruction approach can be formulated as follows:

$$\min_{(\mathbf{u}_{CT},\mathbf{u}_{MRI},\beta)} \|\mathbf{u}_{CT}\|_{TV} + \lambda \|\mathbf{u}_{MRI}\|_{TV} + \gamma \sum_j \left(\left\| \mathbf{E}_j \mathbf{u}_{MRI} - \sum_i w_i \mathbf{T}_{MRI} \beta_{j,i} \right\|_2^2 + \left\| \mathbf{E}_j \mathbf{u}_{CT} - \sum_i w_i \mathbf{T}_{CT} \beta_{j,i} \right\|_2^2 \right)$$
$$\text{s.t.} \mathbf{M}\mathbf{u}_{CT} = \mathbf{f},\ \ \mathbf{R}\mathbf{F}\mathbf{u}_{MRI} = \mathbf{g} \quad (9)$$

where **E** is an operator to extract patches from an image, and β determines which patch is selected for linear approximation by assigning appropriate weighting factors $\{w_i\}$. It is underlined that the same weighting vector $\{w_i\}$ and the same selection vector β are used for both CT and MRI patches that reflect the physical correlation between the two images in Equation (9). Table I presents the workflow for simultaneous CT-MRI reconstruction according to an embodiment. Table II presents the workflow for SC-based CT and MRI image estimation.

In practice, SC can be implemented using the hashing method to accelerate the patch searching process (see also Xi et al., United iterative reconstruction for spectral computed tomography, IEEE Trans. Med. Imag., vol. 34, no. 3, pp. 769–778, Mar. 2015). For example, the hashing-based SC step can be implemented in MATLAB (Math-Works, Massachusetts, USA) or can be accelerated using a high-efficiency programing language, such as C++ (e.g., on a parallel computing framework such as CUDA, because the patch wise operations are naturally parallel).

Simultaneous CT-MRI reconstruction systems and methods of the subject invention are superior to individual TV-based reconstructions. A main reason for such improvement in image quality is utilization of physical correlation between CT and MRI images. The physical correlation can regularize and enhance the imaging performance of either CT or MRI (assuming accurate co-registration of involved datasets); and the synergy is more significant in challenging cases such as few-view CT and low-field MRI. The CT and MRI image registration error can degrade the CT image quality significantly, but has a diminished effect on the MRI image quality.

TABLE II
WORKFLOW FOR SC-BASED CT AND MRI IMAGE ESTIMATION

Input	MRI image $\mathbf{u}_{MRI}$, CT image $\mathbf{u}_{CT}$, the number of similar patches K
Data transformation	According to Fig. 4, deform CT and MRI datasets based on given CT and MRI images.
Estimation:	1. Decompose $\mathbf{u}_{CT}$ into patches $\mathbf{p}_{CT}^{j} = \mathbf{E}_j \mathbf{u}_{CT}$; 2. Decompose $\mathbf{u}_{MRI}$ into patches $\mathbf{p}_{MRI}^{j} = \mathbf{E}_j \mathbf{u}_{MRI}$; 3. Optimize (4) by finding K-best suitable patches $\left\{\mathbf{p}_{CT,i}^{j}\right\}$ and $\left\{\mathbf{p}_{MRI,i}^{j}\right\}$, and their weights $\{w_i\}$in $\mathbf{T}_{CT}$ and $\mathbf{T}_{MRI}$ to represent $\mathbf{p}_{CT}^{j}$ and $\mathbf{p}_{MRI}^{j}$; 4. Estimate CT and MRI image patches with the corresponded CT and MRI image pairs in $\mathbf{T}_{CT-MRI}$ and new weights $\{w_i\}$, $\mathbf{p}_{new,CT}^{j} \approx \sum_{i}^{K} w_i \mathbf{p}_{CT,i}^{j}$, $\mathbf{p}_{new,MRI}^{j} \approx \sum_{i}^{K} w_i \mathbf{p}_{MRI,i}^{j}$; 5. Estimate the corresponded CT image with $\mathbf{p}_{new,CT}^{j}$, $\mathbf{u}_{CT}^{est} = \left(\sum_j \mathbf{E}_j^T \mathbf{E}_j\right)^{-1} \left(\sum_j \mathbf{E}_j^T \mathbf{p}_{new,CT}^{j}\right)$. 6. Estimate the corresponded MRI image with $\mathbf{p}_{new,MRI}^{j}$, $\mathbf{u}_{MRI}^{est} = \left(\sum_j \mathbf{E}_j^T \mathbf{E}_j\right)^{-1} \left(\sum_j \mathbf{E}_j^T \mathbf{p}_{new,MRI}^{j}\right)$.

Although TV is discussed herein as being used for image sparseness, more advanced sparsifying transformations, such as DL can be used and may yield better image quality. In Table I, α was used to balance the regularization effects of TV in an image and TV between images in Equations (7) and (8), and was empirically set to 0.5 in Example 1 below. However, the iteratively estimated image should be increasingly closer to the true image, and the distance between the reconstructed and estimated images should gradually decrease. Thus, the parameter α can be adaptively set with respect to the iteration index for better image quality.

In simultaneous CT-MRI reconstruction according to embodiments of the subject invention, the SC method can link CT and MRI image reconstructions based on physical correlations in the form of paired image patches. The physical correlation can be important to improve the performance of each individual imaging modality. Thus, the size, amount, and type of these patches can be important. If the patch size were too small, there would be insufficient local features for close coupling of different modalities, and the image estimation workflow (see Table II) would be degraded. On the other hand, if the patch size were too large, it would be difficult to approximate a patch accurately via a linear combination of its K-most similar patches. Other important factors are the amount and types of patches that determine whether the K-most similar patches are powerful enough to represent a given patch. However, this does not imply that a larger number of patches is always preferred, because a longer image patch table will dramatically increase computational complexity.

In many embodiments, simultaneous CT-MRI image reconstruction uses SC and CS techniques as key components. A simultaneous CT-MRI scanner can give CT and MRI datasets that are spatially and temporally co-registered. Alternatively, separately acquired CT and MRI datasets can be preprocessed and retrospectively registered as inputs to the reconstruction framework. This retrospectively integrated CT-MRI reconstruction approach can improve studies acquired sequentially, when individual scans are separately acquired under suboptimal conditions due to technical limitations or patient issues (e.g., fast heart rate, unstable medical condition). The results in Example 1 have demonstrated that the performance of the CT-MRI reconstruction algorithm is superior to conventional decoupled CT and MRI reconstructions.

The reconstruction methodology described herein can be generalized to combinations of other tomographic modalities, such as SPECT-CT, PET-MRI, optical-MRI, and omnitomography in general. ROI-oriented scanning, simultaneous data acquisition, and advanced image reconstruction, modeling and analysis for *in vivo* tomographic sampling, can have important applications such as those suggested in Figures 23a-23d.

Figure 23a shows a PET-CT scan of a transverse section of the carotid plaque from a 64-yr-old man, and Figures 23b-23d show DCE-MRI scans of the same transverse section of the carotid plaque. Referring to Figure 23a, the lumen is delineated by the black line, and the plaque is delineated by the dashed black line. Figure 23b shows an image six minutes after contrast injection, and Figure 23c shows a

T1-weighted turbo spin echo MRI. Figure 23d shows parametric K-trans map overlaid on DCE-MRI. Voxel K-trans values are color-encoded from 0 to 0.2 min^{-1}. The lipid-rich necrotic core exhibits low K-trans values at the center of the plaque, and the highly vascularized adventitia (high K-trans values) at the outer rim (indicated by the arrow in Figure 23d) is clearly visualized. The star in Figure 23c denotes the external carotid artery, and the triangle in Figure 23 denotes the sternocleidoid muscle. Figures 23a-23d are adapted from Truijman et al. (Combined 18F-FDG PET-CT and DCE-MRI to assess inflammation and microvascularization in atherosclerotic plaques, Stroke 44, 3568–3570, 2013).

The synergistic reconstruction strategy and novel fusion of tomographic imaging modalities not only takes advantage of complementary attributes from each modality but also potentially optimizes the results of any individual modality and leads to hybrid imaging that is time efficient, cost effective, and more importantly, superior in imaging performance for biomedical applications, such as dynamic contrast enhancement studies on cancer and cardiovascular diseases.

Embodiments of the subject invention allow for simultaneous acquisition of CT and MRI data (e.g., during dynamic contrast enhancement), and advantageously enables both modalities to provide contrast kinetic parameters, while limiting assumptions, intrinsic errors, and limitations of the modeling processes. This synergistic approach can lead to better characterization of the imaged tissues. Simultaneous CT-MRI imaging systems and reconstruction methods fill a major gap of modality coupling and represent a key step toward omnitomography, which is the integration of all relevant imaging modalities for systems biology and precision medicine.

The methods and processes described herein can be embodied as code and/or data. The software code and data described herein can be stored on one or more machine-readable media (e.g., computer-readable media), which may include any device or medium that can store code and/or data for use by a computer system. When a computer system and/or processer reads and executes the code and/or data stored on a computer-readable medium, the computer system and/or processer performs the methods and processes embodied as data structures and code stored within the computer-readable storage medium.

It should be appreciated by those skilled in the art that computer-readable media include removable and non-removable structures/devices that can be used for storage of information, such as computer-readable instructions, data structures, program modules, and other data used by a computing system/environment. A computer-readable medium includes, but is not limited to, volatile memory such as random access memories (RAM, DRAM, SRAM); and non-volatile memory such as flash memory, various read-only-memories (ROM, PROM, EPROM, EEPROM), magnetic and ferromagnetic/ferroelectric memories (MRAM, FeRAM), and magnetic and optical storage devices (hard drives, magnetic tape, CDs, DVDs); network devices; or other media now known or later developed that is capable of storing computer-readable information/data. Computer-readable media should not be construed or interpreted to include any propagating signals. A computer-readable medium of the subject invention can be, for example, a compact disc (CD), digital video disc (DVD), flash memory device, volatile memory, or a hard disk drive (HDD), such as an external HDD or the HDD of a computing device, though embodiments are not limited thereto. A computing device can be, for example, a laptop computer, desktop computer, server, cell phone, or tablet, though embodiments are not limited thereto.

The simultaneous reconstruction methods and processes described herein can improve performance of a combined CT-MRI scanner by drastically improving image quality, time efficiency, cost effectiveness, and imaging performance in general.

The subject invention includes, but is not limited to, the following exemplified embodiments.

Embodiment 1. A system for simultaneous computed tomography (CT)-magnetic resonance imaging (MRI), the system comprising:

a CT subsystem for obtaining CT data;

an MRI subsystem for obtaining MRI data;

at least one processor; and

a machine-readable medium, in operable communication with the CT subsystem, the MRI subsystem, and the at least one processor, having machine-executable instructions stored thereon that, when executed by the at least one processor, perform a method of reconstructing CT and MRI images, the method comprising:

i) reconstructing a CT image $\mathbf{u}_{CT}$ from the CT data;

ii) reconstructing an MRI image $\mathbf{u}_{\mathrm{MRI}}$ from the MRI data;

iii) setting an iteration step $k = 0$;

iv) transforming a CT-MRI dataset $\mathbf{T}_{\mathrm{CT\text{-}MRI}}$ by the $\mathbf{u}_{\mathrm{CT}}$ and $\mathbf{u}_{\mathrm{MRI}}$;

v) estimating the corresponded CT-MRI image $\mathbf{u}_{\mathrm{CT}}^{\mathrm{est}}$ and $\mathbf{u}_{\mathrm{MRI}}^{\mathrm{est}}$ according to $\mathbf{u}_{\mathrm{CT}}$ and $\mathbf{u}_{\mathrm{MRI}}$ aided by the CT-MRI dataset $\mathbf{T}_{\mathrm{CT\text{-}MRI}}$;

vi) reconstructing the CT image $\mathbf{u}_{\mathrm{CT}}$ with $\mathbf{u}_{\mathrm{CT}}^{\mathrm{est}}$ and the CT data;

vii) reconstructing the MRI image $\mathbf{u}_{\mathrm{MRI}}$ with $\mathbf{u}_{\mathrm{MRI}}^{\mathrm{est}}$ and the MRI data;

viii) setting $k = k + 1$; and

ix) repeating steps iv) – viii) until meeting stop criteria, at which point the current $\mathbf{u}_{\mathrm{CT}}^{\mathrm{est}}$ is the reconstructed CT image and the current $\mathbf{u}_{\mathrm{MRI}}^{\mathrm{est}}$ is the reconstructed MRI image.

Embodiment 2. The system according to embodiment 1, wherein reconstructing a CT image $\mathbf{u}_{\mathrm{CT}}$ from the CT data comprises using the following equation:

$$\min_{\mathbf{u}_{\mathrm{CT}}} \|\mathbf{u}_{\mathrm{CT}}\|_{\mathrm{TV}} \ \ \mathrm{s.t.}\, \mathbf{M}\mathbf{u}_{\mathrm{CT}} = \mathbf{f},$$

where $\mathbf{M}$ is a system matrix, $\mathbf{f}$ is the (line integral) CT data (after preprocessing), and $\|\cdot\|_{\mathrm{TV}}$ represents a total variation (TV) transformation.

Embodiment 3. The system according to any of embodiments 1-2, wherein reconstructing an MRI image $\mathbf{u}_{\mathrm{MRI}}$ from the MRI data comprises using the following equation:

$$\min_{\mathbf{u}_{\mathrm{MRI}}} \|\mathbf{u}_{\mathrm{MRI}}\|_{\mathrm{TV}} \ \ \mathrm{s.t.}\, \mathbf{R}\mathbf{F}\mathbf{u}_{\mathrm{MRI}} = \mathbf{g},$$

where $\mathbf{F}$ denotes the Fourier transform, $\mathbf{R}$ is a sampling mask in the k-space, $\mathbf{g}$ is the MRI data, and $\|\cdot\|_{\mathrm{TV}}$ represents a total variation (TV) transformation.

Embodiment 4. The system according to any of embodiments 1-3, wherein estimating the corresponded CT-MRI image comprises using a structural coupling (SC) method.

Embodiment 5. The system according to embodiment 4, wherein the SC method comprises:

a) decomposing $\mathbf{u}_{\mathrm{CT}}$ into patches $\mathbf{p}^{j}_{\mathrm{CT}} = \mathbf{E}_j\, \mathbf{u}_{\mathrm{CT}}$;

b) decomposing $\mathbf{u}_{\mathrm{MRI}}$ into patches $\mathbf{p}^j_{\mathrm{MRI}} = \mathbf{E}_j\, \mathbf{u}_{\mathrm{MRI}}$;

c) optimizing the following equation by finding K-best suitable patches $\{\mathbf{p}^j_{\mathrm{CT},i}\}$ and $\{\mathbf{p}^j_{\mathrm{MRI},i}\}$, and their weights $\{w_i\}$ in $\mathbf{T}_{\mathrm{CT}}$ and $\mathbf{T}_{\mathrm{MRI}}$ to represent $\mathbf{p}^j_{\mathrm{CT}}$ and $\mathbf{p}^j_{\mathrm{MRI}}$

$$\min_{\beta_i} \left\| p_{\mathrm{MRI}} - \sum_i w_i T_{\mathrm{MRI}} \beta_i \right\|_2^2 + \left\| p_{\mathrm{CT}} - \sum_i w_i T_{\mathrm{CT}} \beta_i \right\|_2^2,$$

where w_i equals the average of CT and MRI weightings calculated according to the below equation, $w_i = (w_{\mathrm{CT},i} + w_{\mathrm{MRI},i})/2$, and β_i identifies surrounding high-dimensional data points,

$$w'_{*,i} = \exp\left(-\|\mathbf{p}_* - \mathbf{p}_{*,i}\|_2^2 / h^2\right) \text{ and } w_{*,i} = w'_{*,i} / \sum_i^K w'_{*,i},$$

where h is an empirical value that controls contributions of involved patches, and K is the number of surrounding data points;

d) estimating CT and MRI image patches with the corresponded CT and MRI image pairs in $\mathbf{T}_{\mathrm{CT\text{-}MRI}}$ and new weights $\{w_i\}$,

$$\mathbf{p}^j_{\mathrm{new,CT}} \approx \sum_i^K w_i \mathbf{p}^j_{\mathrm{CT},i}, \ \mathbf{p}^j_{\mathrm{new,MRI}} \approx \sum_i^K w_i \mathbf{p}^j_{\mathrm{MRI},i};$$

e) estimating the corresponded CT image with $\mathbf{p}^j_{\mathrm{new,CT}}$,

$$\mathbf{u}^{est}_{\mathrm{CT}} = \left(\sum_j \mathbf{E}_j^T \mathbf{E}_j\right)^{-1} \left(\sum_j \mathbf{E}_j^T \mathbf{p}^j_{\mathrm{new,CT}}\right); \text{ and}$$

f) estimating the corresponded CT image with $\mathbf{p}^j_{\mathrm{new,CT}}$,

$$\mathbf{u}^{est}_{\mathrm{MRI}} = \left(\sum_j \mathbf{E}_j^T \mathbf{E}_j\right)^{-1} \left(\sum_j \mathbf{E}_j^T \mathbf{p}^j_{\mathrm{new,MRI}}\right).$$

Embodiment 6. The system according to any of embodiments 1-5, wherein reconstructing the CT image $\mathbf{u}_{\mathrm{CT}}$ with $\mathbf{u}_{\mathrm{CT}}^{\mathrm{est}}$ and the CT data comprises using the following equation,

$$\min_{\mathbf{u}_{CT}} (1-\alpha)\left\|\mathbf{u}_{\mathrm{CT}}\right\|_{\mathrm{TV}} + \alpha\left\|\mathbf{u}_{\mathrm{CT}} - \mathbf{u}_{\mathrm{CT}}^{\mathrm{est}}\right\|_{\mathrm{TV}} \text{ s.t.} \mathbf{M}\mathbf{u}_{CT} = \mathbf{f}$$,

where **M** is a system matrix, **f** is the (line integral) CT data (after preprocessing), α is a relaxation parameter, and $\|\cdot\|_{\mathrm{TV}}$ represents a total variation (TV) transformation.

Embodiment 7. The system according to any of embodiments 1-6, wherein reconstructing the MRI image $\mathbf{u}_{\mathrm{MRI}}$ with $\mathbf{u}_{\mathrm{MRI}}^{\mathrm{est}}$ and the MRI data comprises using the following equation,

$$\min_{\mathbf{u}_{MRI}} (1-\alpha)\left\|\mathbf{u}_{\mathrm{MRI}}\right\|_{\mathrm{TV}} + \alpha\left\|\mathbf{u}_{\mathrm{MRI}} - \mathbf{u}_{\mathrm{MRI}}^{\mathrm{est}}\right\|_{\mathrm{TV}}$$

$$\text{s.t.} \mathbf{F}\mathbf{u}_{\mathrm{MRI}} = \mathbf{g}$$,

where **F** denotes the Fourier transform, **R** is a sampling mask in the k-space, **g** is the MRI data, α is a relaxation parameter, and $\|\cdot\|_{\mathrm{TV}}$ represents a total variation (TV) transformation.

Embodiment 8. The system according to any of embodiments 1-7, wherein steps iv) through vii) can be formulated as follows,

$$\min_{(\mathbf{u}_{CT},\mathbf{u}_{MRI},\beta)} \left\|\mathbf{u}_{\mathrm{CT}}\right\|_{\mathrm{TV}} + \lambda\left\|\mathbf{u}_{\mathrm{MRI}}\right\|_{\mathrm{TV}} + \gamma\sum_j \left(\left\|\mathbf{E}_j\mathbf{u}_{\mathrm{MRI}} - \sum_i w_i \mathbf{T}_{\mathrm{MRI}}\beta_{j,i}\right\|_2^2 + \left\|\mathbf{E}_j\mathbf{u}_{\mathrm{CT}} - \sum_i w_i \mathbf{T}_{\mathrm{CT}}\beta_{j,i}\right\|_2^2\right)$$

$$\text{s.t.} \mathbf{M}\mathbf{u}_{CT} = \mathbf{f},\quad \mathbf{R}\mathbf{F}\mathbf{u}_{\mathrm{MRI}} = \mathbf{g}$$,

where **E** is an operator to extract patches from an image, β determines which patch is selected for linear approximation by assigning appropriate weighting factors $\{w_i\}$, **M** is a system matrix, **f** is the (line integral) CT data (after preprocessing), **F** denotes the

Fourier transform, **R** is a sampling mask in the k-space, **g** is the MRI data, and $\|\cdot\|_{TV}$ represents a total variation (TV) transformation.

Embodiment 9. The system according to any of embodiments 1-8, wherein estimating the corresponded CT-MRI image comprises using an SC method implemented using a hashing method to accelerate the patch searching process.

Embodiment 10. The system according to any of embodiments 1-9, wherein the method of reconstructing CT and MRI images further comprises utilizing prior knowledge of CT images.

Embodiment 11. The system according to embodiment 10, wherein the prior knowledge of CT images comprises information from a CT image atlas.

Embodiment 12. The system according to any of embodiments 10-11, wherein the prior knowledge of CT images is utilized in step i).

Embodiment 13. The system according to any of embodiments 1-12, wherein the method of reconstructing CT and MRI images further comprises utilizing prior knowledge of MRI images.

Embodiment 14. The system according to embodiment 13, wherein the prior knowledge of MRI images comprises information from an MRI image atlas.

Embodiment 15. The system according to any of embodiments 13-14, wherein the prior knowledge of MRI images is utilized in step i).

Embodiment 16. The system according to any of embodiments 1-15, wherein the MRI subsystem comprises superconducting magnets.

Embodiment 17. The system according embodiment 16, wherein the superconducting magnets are room temperature superconducting magnets.

Embodiment 18. The system according to any of embodiments 1-17, wherein the MRI subsystem comprises two donut shaped magnets facing each other.

Embodiment 19. The system according to any of embodiments 1-18, wherein the MRI subsystem comprises two hexagonal magnet arrays facing each other.

Embodiment 20. The system according to any of embodiments 1-19, wherein the CT subsystem and the MRI subsystem are seamlessly integrated with one another.

Embodiment 21. The system according to any of embodiments 1-20, wherein components of the CT subsystem are quasi-stationary.

Embodiment 22. The system according to embodiment 22, wherein X-ray sources and detectors of the CT subsystem are distributed face-to-face along a circle.

Embodiment 23. The system according to any of embodiments 1-22, wherein the CT data comprises only a few-view set of CT data.

Embodiment 24. The system according to any of embodiments 1-23, wherein the method of reconstructing CT and MRI images comprises using an SC method and a compressive sensing (CS) method.

Embodiment 25. A machine-readable medium, having machine-executable instructions stored thereon that, when executed by at least one processor, perform a method of reconstructing CT and MRI images, the method comprising:

i) reconstructing a CT image $\mathbf{u}_{\mathrm{CT}}$ from CT data;

ii) reconstructing an MRI image $\mathbf{u}_{\mathrm{MRI}}$ from MRI data;

iii) setting an iteration step $k = 0$;

iv) transforming a CT-MRI dataset $\mathbf{T}_{\text{CT-MRI}}$ by the $\mathbf{u}_{\mathrm{CT}}$ and $\mathbf{u}_{\mathrm{MRI}}$;

v) estimating the corresponded CT-MRI image $\mathbf{u}\frac{\text{est}}{\text{CT}}$ and $\mathbf{u}\frac{\text{est}}{\text{MRI}}$ according to $\mathbf{u}_{\mathrm{CT}}$ and $\mathbf{u}_{\mathrm{MRI}}$ aided by the CT-MRI dataset $\mathbf{T}_{\text{CT-MRI}}$;

vi) reconstructing the CT image $\mathbf{u}_{\mathrm{CT}}$ with $\mathbf{u}\frac{\text{est}}{\text{CT}}$ and the CT data;

vii) reconstructing the MRI image $\mathbf{u}_{\mathrm{MRI}}$ with $\mathbf{u}\frac{\text{est}}{\text{MRI}}$ and the MRI data;

viii) setting $k = k + 1$; and

ix) repeating steps iv) – viii) until meeting stop criteria, at which point the current $\mathbf{u}\frac{\text{est}}{\text{CT}}$ is the reconstructed CT image and the current $\mathbf{u}\frac{\text{est}}{\text{MRI}}$ is the reconstructed MRI image.

Embodiment 26. The machine-readable medium according to embodiment 25, wherein reconstructing a CT image $\mathbf{u}_{\mathrm{CT}}$ from the CT data comprises using the following equation:

$$\min_{\mathbf{u}_{CT}} \|\mathbf{u}_{CT}\|_{TV} \ \text{s.t.} \mathbf{M}\mathbf{u}_{CT} = \mathbf{f},$$

where $\mathbf{M}$ is a system matrix, $\mathbf{f}$ is the (line integral) CT data (after preprocessing), and $\|\cdot\|_{\mathrm{TV}}$ represents a total variation (TV) transformation.

Embodiment 27. The machine-readable medium according to any of embodiments 25-26, wherein reconstructing an MRI image $\mathbf{u}_{\mathrm{MRI}}$ from the MRI data comprises using the following equation:

$$\min_{\mathbf{u}_{MRI}} \|\mathbf{u}_{MRI}\|_{TV} \quad \text{s.t.} \mathbf{R}\mathbf{F}\mathbf{u}_{MRI} = \mathbf{g},$$

where $\mathbf{F}$ denotes the Fourier transform, $\mathbf{R}$ is a sampling mask in the k-space, $\mathbf{g}$ is the MRI data, and $\|\cdot\|_{\mathrm{TV}}$ represents a total variation (TV) transformation.

Embodiment 28. The machine-readable medium stem according to any of embodiments 25-27, wherein estimating the corresponded CT-MRI image comprises using a structural coupling (SC) method.

Embodiment 29. The machine-readable medium according to embodiment 28, wherein the SC method comprises:

a) decomposing $\mathbf{u}_{\mathrm{CT}}$ into patches $\mathbf{p}^{j}_{\mathrm{CT}} = \mathbf{E}_j\, \mathbf{u}_{\mathrm{CT}}$;

b) decomposing $\mathbf{u}_{\mathrm{MRI}}$ into patches $\mathbf{p}^{j}_{\mathrm{MRI}} = \mathbf{E}_j\, \mathbf{u}_{\mathrm{MRI}}$;

c) optimizing the following equation by finding K-best suitable patches $\left\{\mathbf{p}^{j}_{CT,i}\right\}$ and $\left\{\mathbf{p}^{j}_{MRI,i}\right\}$, and their weights $\{w_i\}$ in $\mathbf{T}_{\mathrm{CT}}$ and $\mathbf{T}_{\mathrm{MRI}}$ to represent $\mathbf{p}^{j}_{\mathrm{CT}}$ and $\mathbf{p}^{j}_{\mathrm{MRI}}$

$$\min_{\beta_i} \left\| p_{MRI} - \sum_i w_i T_{MRI} \beta_i \right\|_2^2 + \left\| p_{CT} - \sum_i w_i T_{CT} \beta_i \right\|_2^2,$$

where w_i equals the average of CT and MRI weightings calculated according to the below equation, $w_i = (w_{\mathrm{CT},i} + w_{\mathrm{MRI},i})/2$, and β_i identifies surrounding high-dimensional data points,

$$w'_{*,i} = \exp\left(-\|\mathbf{p}_* - \mathbf{p}_{*,i}\|_2^2 / h^2\right) \text{ and } w_{*,i} = w'_{*,i} / \sum_i^K w'_{*,i},$$

where h is an empirical value that controls contributions of involved patches, and K is the number of surrounding data points;

d) estimating CT and MRI image patches with the corresponded CT and MRI image pairs in $\mathbf{T}_{\mathrm{CT\text{-}MRI}}$ and new weights $\{w_i\}$,

$$\mathbf{p}^{j}_{\mathrm{new,CT}} \approx \sum_{i}^{K} w_i \mathbf{p}^{j}_{\mathrm{CT},i}, \mathbf{p}^{j}_{\mathrm{new,MRI}} \approx \sum_{i}^{K} w_i \mathbf{p}^{j}_{\mathrm{MRI},i};$$

e) estimating the corresponded CT image with $\mathbf{p}^{j}_{\mathrm{new,CT}}$,

$$\mathbf{u}^{est}_{\mathrm{CT}} = \left(\sum_{j} \mathbf{E}^{T}_{j} \mathbf{E}_{j}\right)^{-1} \left(\sum_{j} \mathbf{E}^{T}_{j} \mathbf{p}^{j}_{\mathrm{new,CT}}\right); \text{ and}$$

f) estimating the corresponded CT image with $\mathbf{p}^{j}_{\mathrm{new,CT}}$,

$$\mathbf{u}^{est}_{\mathrm{MRI}} = \left(\sum_{j} \mathbf{E}^{T}_{j} \mathbf{E}_{j}\right)^{-1} \left(\sum_{j} \mathbf{E}^{T}_{j} \mathbf{p}^{j}_{\mathrm{new,MRI}}\right).$$

Embodiment 30. The machine-readable medium according to any of embodiments 25-29, wherein reconstructing the CT image $\mathbf{u}_{\mathrm{CT}}$ with $\mathbf{u}^{\mathrm{est}}_{\mathrm{CT}}$ and the CT data comprises using the following equation,

$$\min_{\mathbf{u}_{CT}} (1-\alpha) \|\mathbf{u}_{\mathrm{CT}}\|_{\mathrm{TV}} + \alpha \|\mathbf{u}_{\mathrm{CT}} - \mathbf{u}^{\mathrm{est}}_{\mathrm{CT}}\|_{\mathrm{TV}} \text{ s.t.} \mathbf{M}\mathbf{u}_{\mathrm{CT}} = \mathbf{f},$$

where $\mathbf{M}$ is a system matrix, $\mathbf{f}$ is the (line integral) CT data (after preprocessing), α is a relaxation parameter, and $\|\cdot\|_{\mathrm{TV}}$ represents a total variation (TV) transformation.

Embodiment 31. The machine-readable medium according to any of embodiments 25-30, wherein reconstructing the MRI image $\mathbf{u}_{\mathrm{MRI}}$ with $\mathbf{u}^{\mathrm{est}}_{\mathrm{MRI}}$ and the MRI data comprises using the following equation,

$$\min_{\mathbf{u}_{MRI}} (1-\alpha) \|\mathbf{u}_{\mathrm{MRI}}\|_{\mathrm{TV}} + \alpha \|\mathbf{u}_{\mathrm{MRI}} - \mathbf{u}^{\mathrm{est}}_{\mathrm{MRI}}\|_{\mathrm{TV}}$$
$$\text{s.t.} \mathbf{F}\mathbf{u}_{\mathrm{MRI}} = \mathbf{g},$$

where $\mathbf{F}$ denotes the Fourier transform, $\mathbf{R}$ is a sampling mask in the k-space, $\mathbf{g}$ is the MRI data, α is a relaxation parameter, and $\|\cdot\|_{\mathrm{TV}}$ represents a total variation (TV) transformation.

Embodiment 32. The machine-readable medium according to any of embodiments 25-31, wherein steps iv) through vii) can be formulated as follows,

$$\min_{(\mathbf{u}_{CT},\mathbf{u}_{MRI},\beta)} \|\mathbf{u}_{CT}\|_{TV} + \lambda\|\mathbf{u}_{MRI}\|_{TV} + \gamma\sum_j\left(\left\|\mathbf{E}_j\mathbf{u}_{MRI} - \sum_i w_i\mathbf{T}_{MRI}\beta_{j,i}\right\|_2^2 + \left\|\mathbf{E}_j\mathbf{u}_{CT} - \sum_i w_i\mathbf{T}_{CT}\beta_{j,i}\right\|_2^2\right)$$

$$\text{s.t.}\,\mathbf{M}\mathbf{u}_{CT} = \mathbf{f},\quad \mathbf{RF}\mathbf{u}_{MRI} = \mathbf{g}$$

,

where **E** is an operator to extract patches from an image, β determines which patch is selected for linear approximation by assigning appropriate weighting factors $\{w_i\}$, **M** is a system matrix, **f** is the (line integral) CT data (after preprocessing), **F** denotes the Fourier transform, **R** is a sampling mask in the k-space, **g** is the MRI data, and $\|\cdot\|_{TV}$ represents a total variation (TV) transformation.

Embodiment 33. The machine-readable medium according to any of embodiments 25-32, wherein estimating the corresponded CT-MRI image comprises using an SC method implemented using a hashing method to accelerate the patch searching process.

Embodiment 34. The machine-readable medium according to any of embodiments 25-33, wherein the method of reconstructing CT and MRI images further comprises utilizing prior knowledge of CT images.

Embodiment 35. The machine-readable medium according to embodiment 34, wherein the prior knowledge of CT images comprises information from a CT image atlas.

Embodiment 36. The machine-readable medium according to any of embodiments 34-35, wherein the prior knowledge of CT images is utilized in step i).

Embodiment 37. The machine-readable medium according to any of embodiments 25-36, wherein the method of reconstructing CT and MRI images further comprises utilizing prior knowledge of MRI images.

Embodiment 38. The machine-readable medium according to embodiment 37, wherein the prior knowledge of MRI images comprises information from an MRI image atlas.

Embodiment 39. The machine-readable medium according to any of embodiments 37-38, wherein the prior knowledge of MRI images is utilized in step i).

Embodiment 40. The machine-readable medium according to any of embodiments 25-39, wherein the CT data comprises only a few-view set of CT data.

Embodiment 41. The machine-readable medium according to any of embodiments 25-40, wherein the method of reconstructing CT and MRI images comprises using an SC method and a compressive sensing (CS) method.

Embodiment 42. A method of reconstructing CT and MRI images, the method comprising:

i) reconstructing a CT image $\mathbf{u}_{CT}$ from CT data;

ii) reconstructing an MRI image $\mathbf{u}_{MRI}$ from MRI data;

iii) setting an iteration step $k = 0$;

iv) transforming a CT-MRI dataset $\mathbf{T}_{CT\text{-}MRI}$ by the $\mathbf{u}_{CT}$ and $\mathbf{u}_{MRI}$;

v) estimating the corresponded CT-MRI image $\mathbf{u}\frac{\text{est}}{\text{CT}}$ and $\mathbf{u}\frac{\text{est}}{\text{MRI}}$ according to $\mathbf{u}_{CT}$ and $\mathbf{u}_{MRI}$ aided by the CT-MRI dataset $\mathbf{T}_{CT\text{-}MRI}$;

vi) reconstructing the CT image $\mathbf{u}_{CT}$ with $\mathbf{u}\frac{\text{est}}{\text{CT}}$ and the CT data;

vii) reconstructing the MRI image $\mathbf{u}_{MRI}$ with $\mathbf{u}\frac{\text{est}}{\text{MRI}}$ and the MRI data;

viii) setting $k = k + 1$; and

ix) repeating steps iv) – viii) until meeting stop criteria, at which point the current $\mathbf{u}\frac{\text{est}}{\text{CT}}$ is the reconstructed CT image and the current $\mathbf{u}\frac{\text{est}}{\text{MRI}}$ is the reconstructed MRI image.

Embodiment 43. The method according to embodiment 42, wherein reconstructing a CT image $\mathbf{u}_{CT}$ from the CT data comprises using the following equation:

$$\min_{\mathbf{u}_{CT}} \|\mathbf{u}_{CT}\|_{TV} \ \text{s.t.} \mathbf{M}\mathbf{u}_{CT} = \mathbf{f}$$,

where $\mathbf{M}$ is a system matrix, $\mathbf{f}$ is the (line integral) CT data (after preprocessing), and $\|\cdot\|_{TV}$ represents a total variation (TV) transformation.

Embodiment 44. The method according to any of embodiments 42-43, wherein reconstructing an MRI image $\mathbf{u}_{MRI}$ from the MRI data comprises using the following equation:

$$\min_{\mathbf{u}_{MRI}} \|\mathbf{u}_{MRI}\|_{TV} \text{ s.t.} \mathbf{RFu}_{MRI} = \mathbf{g},$$

where **F** denotes the Fourier transform, **R** is a sampling mask in the k-space, **g** is the MRI data, and $\|\cdot\|_{TV}$ represents a total variation (TV) transformation.

Embodiment 45. The method stem according to any of embodiments 42-44, wherein estimating the corresponded CT-MRI image comprises using a structural coupling (SC) method.

Embodiment 46. The method according to embodiment 45, wherein the SC method comprises:

a) decomposing $\mathbf{u}_{CT}$ into patches $\mathbf{p}^j_{CT} = \mathbf{E}_j \mathbf{u}_{CT}$;

b) decomposing $\mathbf{u}_{MRI}$ into patches $\mathbf{p}^j_{MRI} = \mathbf{E}_j \mathbf{u}_{MRI}$;

c) optimizing the following equation by finding K-best suitable patches $\left\{\mathbf{p}^j_{CT,i}\right\}$ and $\left\{\mathbf{p}^j_{MRI,i}\right\}$, and their weights $\{w_i\}$ in $\mathbf{T}_{CT}$ and $\mathbf{T}_{MRI}$ to represent $\mathbf{p}^j_{CT}$ and $\mathbf{p}^j_{MRI}$

$$\min_{\beta_i} \left\| p_{MRI} - \sum_i w_i T_{MRI} \beta_i \right\|_2^2 + \left\| p_{CT} - \sum_i w_i T_{CT} \beta_i \right\|_2^2,$$

where w_i equals the average of CT and MRI weightings calculated according to the below equation, $w_i = (w_{CT,i} + w_{MRI,i})/2$, and β_i identifies surrounding high-dimensional data points,

$$w'_{*,i} = \exp\left(-\|\mathbf{p}_* - \mathbf{p}_{*,i}\|_2^2 / h^2\right) \text{ and } w_{*,i} = w'_{*,i} / \sum_i^K w'_{*,i},$$

where h is an empirical value that controls contributions of involved patches, and K is the number of surrounding data points;

d) estimating CT and MRI image patches with the corresponded CT and MRI image pairs in $\mathbf{T}_{CT\text{-}MRI}$ and new weights $\{w_i\}$,

$$\mathbf{p}^{j}_{\mathrm{new,CT}} \approx \sum_{i}^{K} w_i \mathbf{p}^{j}_{\mathrm{CT},i}, \mathbf{p}^{j}_{\mathrm{new,MRI}} \approx \sum_{i}^{K} w_i \mathbf{p}^{j}_{\mathrm{MRI},i}$$
;

e) estimating the corresponded CT image with $\mathbf{p}^{j}_{\mathrm{new,CT}}$,

$$\mathbf{u}^{est}_{\mathrm{CT}} = \left(\sum_{j} \mathbf{E}_j^T \mathbf{E}_j\right)^{-1} \left(\sum_{j} \mathbf{E}_j^T \mathbf{p}^{j}_{\mathrm{new,CT}}\right)$$
; and

f) estimating the corresponded CT image with $\mathbf{p}^{j}_{\mathrm{new,CT}}$,

$$\mathbf{u}^{est}_{\mathrm{MRI}} = \left(\sum_{j} \mathbf{E}_j^T \mathbf{E}_j\right)^{-1} \left(\sum_{j} \mathbf{E}_j^T \mathbf{p}^{j}_{\mathrm{new,MRI}}\right).$$

Embodiment 47. The method according to any of embodiments 42-46, wherein reconstructing the CT image $\mathbf{u}_{\mathrm{CT}}$ with $\mathbf{u}\frac{\mathrm{est}}{\mathrm{CT}}$ and the CT data comprises using the following equation,

$$\min_{\mathbf{u}_{\mathrm{CT}}} (1-\alpha) \|\mathbf{u}_{\mathrm{CT}}\|_{\mathrm{TV}} + \alpha \left\|\mathbf{u}_{\mathrm{CT}} - \mathbf{u}^{\mathrm{est}}_{\mathrm{CT}}\right\|_{\mathrm{TV}} \ \mathrm{s.t.} \mathbf{M}\mathbf{u}_{\mathrm{CT}} = \mathbf{f}$$
,

where **M** is a system matrix, **f** is the (line integral) CT data (after preprocessing), α is a relaxation parameter, and $\|\cdot\|_{\mathrm{TV}}$ represents a total variation (TV) transformation.

Embodiment 48. The method according to any of embodiments 42-47, wherein reconstructing the MRI image $\mathbf{u}_{\mathrm{MRI}}$ with $\mathbf{u}\frac{\mathrm{est}}{\mathrm{MRI}}$ and the MRI data comprises using the following equation,

$$\min_{\mathbf{u}_{\mathrm{MRI}}} (1-\alpha) \|\mathbf{u}_{\mathrm{MRI}}\|_{\mathrm{TV}} + \alpha \left\|\mathbf{u}_{\mathrm{MRI}} - \mathbf{u}^{\mathrm{est}}_{\mathrm{MRI}}\right\|_{\mathrm{TV}}$$

$$\mathrm{s.t.} \mathbf{F}\mathbf{u}_{\mathrm{MRI}} = \mathbf{g}$$
,

where **F** denotes the Fourier transform, **R** is a sampling mask in the k-space, **g** is the MRI data, α is a relaxation parameter, and $\|\cdot\|_{\mathrm{TV}}$ represents a total variation (TV) transformation.

Embodiment 49. The method according to any of embodiments 42-48, wherein steps iv) through vii) can be formulated as follows,

$$\min_{(\mathbf{u}_{CT},\mathbf{u}_{MRI},\beta)} \|\mathbf{u}_{CT}\|_{TV} + \lambda\|\mathbf{u}_{MRI}\|_{TV} + \gamma\sum_j \left(\left\| \mathbf{E}_j\mathbf{u}_{MRI} - \sum_i w_i \mathbf{T}_{MRI}\beta_{j,i} \right\|_2^2 + \left\| \mathbf{E}_j\mathbf{u}_{CT} - \sum_i w_i \mathbf{T}_{CT}\beta_{j,i} \right\|_2^2 \right)$$

$$\text{s.t.}\,\mathbf{M}\mathbf{u}_{CT} = \mathbf{f},\quad \mathbf{R}\mathbf{F}\mathbf{u}_{MRI} = \mathbf{g}$$

,

where **E** is an operator to extract patches from an image, β determines which patch is selected for linear approximation by assigning appropriate weighting factors $\{w_i\}$, **M** is a system matrix, **f** is the (line integral) CT data (after preprocessing), **F** denotes the Fourier transform, **R** is a sampling mask in the k-space, **g** is the MRI data, and $\|\cdot\|_{TV}$ represents a total variation (TV) transformation.

Embodiment 50. The method according to any of embodiments 42-49, wherein estimating the corresponded CT-MRI image comprises using an SC method implemented using a hashing method to accelerate the patch searching process.

Embodiment 51. The method according to any of embodiments 42-50, wherein the method of reconstructing CT and MRI images further comprises utilizing prior knowledge of CT images.

Embodiment 52. The method according to embodiment 51, wherein the prior knowledge of CT images comprises information from a CT image atlas.

Embodiment 53. The method according to any of embodiments 51-52, wherein the prior knowledge of CT images is utilized in step i).

Embodiment 54. The method according to any of embodiments 42-53, wherein the method of reconstructing CT and MRI images further comprises utilizing prior knowledge of MRI images.

Embodiment 55. The method according to embodiment 54, wherein the prior knowledge of MRI images comprises information from an MRI image atlas.

Embodiment 56. The method according to any of embodiments 54-55, wherein the prior knowledge of MRI images is utilized in step i).

Embodiment 57. The method according to any of embodiments 42-56, wherein the CT data comprises only a few-view set of CT data.

Embodiment 58. The method according to any of embodiments 42-57, wherein the method of reconstructing CT and MRI images comprises using an SC method and a compressive sensing (CS) method.

Embodiment 59. A system for simultaneous computed tomography (CT)-magnetic resonance imaging (MRI), the system comprising:

a CT subsystem for obtaining CT data;

an MRI subsystem for obtaining MRI data;

at least one processor; and

a machine-readable medium, in operable communication with the CT subsystem, the MRI subsystem, and the at least one processor, having machine-executable instructions stored thereon that, when executed by the at least one processor, perform a method of reconstructing CT and MRI images,

wherein the MRI subsystem comprises superconducting magnets.

Embodiment 60. The system according embodiment 59, wherein the superconducting magnets are room temperature superconducting magnets.

Embodiment 61. The system according to any of embodiments 59-60, wherein the MRI subsystem comprises two donut shaped magnets facing each other.

Embodiment 62. The system according to any of embodiments 59-61, wherein the MRI subsystem comprises two hexagonal magnet arrays facing each other.

Embodiment 63. The system according to any of embodiments 59-62, wherein the CT subsystem and the MRI subsystem are seamlessly integrated with one another.

Embodiment 64. The system according to any of embodiments 59-63, wherein components of the CT subsystem are quasi-stationary.

Embodiment 65. The system according to embodiment 64, wherein X-ray sources and detectors of the CT subsystem are distributed face-to-face along a circle.

Embodiment 66. The system according to any of embodiments 59-65, wherein the method of reconstructing CT and MRI images is the method according to any of embodiments 42-58.

A greater understanding of the present invention and of its many advantages may be had from the following examples, given by way of illustration. The following examples are illustrative of some of the methods, applications, embodiments and variants of the present invention. They are, of course, not to be considered as limiting the invention. Numerous changes and modifications can be made with respect to the invention.

EXAMPLE 1

Numerical simulations were performed with representative CT and MRI datasets to evaluate the results of the simultaneous CT-MRI image reconstruction approaches as described herein. In the simultaneous CT-MRI scanner, there was a limited number of X-ray sources in the CT subsystem, and a low-background magnetic field in the MRI subsystem. This cost-effective starting point actually posed an interesting challenge to investigate few-view CT and low resolution MRI coupling using a simultaneous CT-MRI image reconstruction algorithm.

In the simulations, CT and MRI datasets were derived from various sources: 1) established numerical phantoms (modified NCAT phantom (mNCAT) – see also Segars et al., Development and application of the new dynamic Nurbs-based Cardiac-Torso (NCAT) phantom, J. Nucl. Med., vol. 42, pp. 7p–7p, 2001; which is hereby incorporated by reference herein in its entirety); 2) the visible human project (VHP) (Ackerman, The visible human project, Proc. IEEE, vol. 86, no. 3, pp. 504–511, Mar. 1998; which is hereby incorporated by reference herein in its entirety); and 3) *in vivo* multimodality porcine imaging studies. In these experiments, identical samples were sequentially imaged by CT and MRI scanners.

Figure 3a shows a ground truth CT image (left), a ground truth MRI image (center), and a registration result image (right) for the modified NCAT phantom (mNCAT). Figure 3b shows a ground truth CT image (left), a ground truth MRI image (center), and a registration result image (right) for the visible human project phantom

(VHP). Figure 3c shows a ground truth CT image (left), a ground truth MRI image (center), and a registration result image (right) for the *in vivo* porcine sample.

In the numerical phantom experiment, the CT and MRI datasets have perfect spatial registration, as shown in Figure 3a. In the other two real-dataset experiments, the CT and MRI scans were performed sequentially; thus, there were small non-rigid movements between their CT and MRI datasets, and their volumes were in different voxel sizes. Hence, a rigid registration and interpolation process was incorporated to align the CT and MRI datasets, as shown in Figure 3. In the VHP experiment (Figure 3b), the MRI dataset was composed of T2-weighted images. In the porcine multimodality imaging study (Figure 3c), dynamic trans-axial CT and MRI images were collected. Sequential CT and MRI images were acquired at the Yale University of the porcine lower extremity of an anesthetized animal in a fixed position, with the full approval of the Institutional Animal Care and Use Committee. The high-resolution porcine CT images of the lower extremities were acquired on a 64-slice CT scanner (Discovery VCT, GE Healthcare) following administration of iodinated contrast (Omnipaque 350 mgI/ml) to define vascular anatomy. MRI time-off-light and phase velocity images were acquired on a 1.5-T MR system (Sonata, Siemens) as non-contrast alternative approaches to define vascular anatomy and flow physiology respectively.

To simulate a simultaneous CT-MRI scan, the CT and MRI images in each experiment were re-projected and re-sampled according to appropriate imaging protocols. In the CT subsystem, the number of X-ray sources was set to 10 in the mNCAT experiment, and 15 sources were assumed in each of the VHP and porcine experiments. Without the loss of generality, only fan-beam geometry was considered. There were 512 channels per detector array for the numerical phantom, and 400 in each of the VHP and porcine experiments. In the MRI subsystem, the k-space was sampled in a low-frequency area (see Figure 5) due to the low-background field utilized in the combined CT-MRI design. Figures 5a, 5b, and 5c show images of low magnetic field measurements in an MRI sub-system for the mNCAT, the VHP, and the porcine sample, respectively. Referring to Figures 5a-5c, sampling patterns in the k-space are shown under sampling rates of 92.5%, 82.7%, and 89.0%, respectively.

Reconstructed images in mNCAT, VHP, and porcine experiments comprised 256×256, 200 × 200, 320 × 320 pixels, respectively. During the offline process for the simultaneous CT-MRI reconstruction, three tables of paired CT-MRI image patches, $\boldsymbol{T}_{\mathrm{CT-MRI}}^{m\mathrm{NCAT}}$, $\mathbf{T}_{\mathrm{CT-MRI}}^{VHP}$, and $\mathbf{T}_{\mathrm{CT-MRI}}^{\mathrm{porcine}}$ were constructed with CT and MRI slices from mNCAT, VHP, and porcine datasets, respectively. It should be noted that there was no overlap between the images used for training CT-MRI patch tables and the images tested for simultaneous CT-MRI reconstruction.

For comparison, the conventional TV-based approach was implemented and applied for separate CT and MRI reconstructions. Both the conventional and proposed algorithms were implemented in the Split–Bregman framework. Images were reconstructed with competing algorithms and quantitatively compared in terms of the root-mean-square error (RMSE) and the structural similarity index (SSIM). The RMSE quantifies the difference between the reconstructed image and the ground truth. The SSIM measures similarity between a reconstructed image and the ground truth. The higher the structural similarity between the two images, the closer the SSIM value approaches to 1. In each experiment, RMSE was used to quantify the differences between the reconstructed and ground truth images with varying patch size (p_n) in $\mathbf{T}_{\mathrm{CT-MRI}}$ to choose an optimal value.

Figures 6a and 6b show CT images for the mNCAT simulation, reconstructed using total variation (TV)-based reconstruction and simultaneous CT-MRI reconstruction according to an embodiment of the subject invention, respectively. Figures 6c and 6d show MRI images for the mNCAT simulation, reconstructed using TV-based reconstruction and simultaneous CT-MRI reconstruction according to an embodiment of the subject invention, respectively. Figures 6e-6h show images of the residual errors relative to ground truth for the reconstructions of Figures 6a-6d, respectively. Figures 6a-6d are displayed in [0,1], and Figures 6e-6h are displayed in [-0.15, 0.15].

Figures 7a, 7b, and 7c show plots of root-mean-square error (RMSE) with respect to patch size ($\sqrt{p_n}$), relaxation parameter (α), and iteration index (k), respectively, for simultaneous CT-MRI construction in the mNCAT experiment. Referring to Figures 7a-7c, RMSE quantifies the differences between the reconstructed and ground truth images with respect to various patch sizes and relaxation parameter values, as well as the intermediate results as a function of the iteration index k (with $\sqrt{p_n} = 5$). In each of Figures 7a and 7b, the square points (upper section of plot) are for CT, and the circle points (lower section of plot) are for MRI. In Figure 7c, the square points (upper section of plot) are for CT-MRI-based CT reconstruction, and the circle points (lower section of plot) are for CT-MRI-based MRI reconstruction, the upper dotted line is for TV-based CT reconstruction, and the lower dotted line is for TV-based MRI reconstruction.

Figures 8a and 8b show plots of RMSE with respect to various registration errors $(\Delta x, \Delta y)$ for CT images and MRI images, respectively, in simultaneous CT-MRI construction in the mNCAT experiment. Figures 8c and 8d show plots of RMSE with respect to various noise levels for simultaneous CT-MRI construction (squares) and TV-based reconstruction ("x" data points) for CT images and MRI images, respectively, in the mNCAT experiment. The RMSE of Figures 8a and 8b quantifies the differences between the reconstructed and ground truth images with respective to various registration errors between CT and MRI images, respectively, and the RMSE of Figures 8c and 8d quantifies the differences between the reconstructed and ground truth images at different noise levels.

Figures 9a and 9b show CT images for the VHP simulation, reconstructed using TV-based reconstruction and simultaneous CT-MRI reconstruction according to an embodiment of the subject invention, respectively. Figures 9c and 9d show MRI images for the VHP simulation, reconstructed using TV-based reconstruction and simultaneous CT-MRI reconstruction according to an embodiment of the subject invention, respectively. Figures 9e-9h show images of the residual errors relative to ground truth for the reconstructions of Figures 9a-9d, respectively. Figures 9a-9d are displayed in [0,1], and Figures 9e-9h are displayed in [-0.2, 0.2].

Figures 10a-10c show local enlarged views of a ground truth CT image, a reconstructed CT image using TV-based reconstruction, and a reconstructed CT image using simultaneous CT-MRI reconstruction, respectively, for the VHP experiment. Figures 10d-10f show local enlarged views of a ground truth MRI image, a reconstructed MRI image using TV-based reconstruction, and a reconstructed MRI image using simultaneous CT-MRI reconstruction, respectively, for the VHP experiment.

Figures 11a and 11b show plots of RMSE with respect to patch size ($\sqrt{p_n}$) and iteration index (k), respectively, for simultaneous CT-MRI construction in the VHP experiment. Referring to Figures 11a and 11b, RMSE quantifies the differences between the reconstructed and ground truth images with respect to various patch sizes, as well as the intermediate results as a function of the iteration index k (with $\sqrt{p_n} = 15$). In Figure 11a, the circle points (upper section of plot) are for CT, and the square points (lower section of plot) are for MRI. In Figure 11b, the square points (upper section of plot) are for CT-MRI-based CT reconstruction, and the circle points (lower section of plot) are for CT-MRI-based MRI reconstruction, the upper dotted line is for TV-based CT reconstruction, and the lower dotted line is for TV-based MRI reconstruction.

Figures 12a and 12b show CT images for the porcine sample simulation, reconstructed using TV-based reconstruction and simultaneous CT-MRI reconstruction according to an embodiment of the subject invention, respectively. Figures 12c and 12d show MRI images for the porcine sample simulation, reconstructed using TV-based reconstruction and simultaneous CT-MRI reconstruction according to an embodiment of the subject invention, respectively. Figures 12e-12h show images of the residual errors relative to ground truth for the reconstructions of Figures 12a-12d, respectively. Figures 12a-12d are displayed in [0,1], Figures 12 e and 12f are displayed in [-0.3, 0.3], and Figures 12g and 12h are displayed in [-0.2, 0.2].

Figures 13a-13c show local enlarged views of a ground truth CT image, a reconstructed CT image using TV-based reconstruction, and a reconstructed CT image using simultaneous CT-MRI reconstruction, respectively, for the porcine sample experiment. Figures 13d-13f show local enlarged views of a ground truth MRI image, a reconstructed MRI image using TV-based reconstruction, and a reconstructed MRI image using simultaneous CT-MRI reconstruction, respectively, for the porcine sample experiment. Veins show as black and arteries show as white, demonstrating improved definition of small vascular structures.

Figures 14a and 14b show plots of RMSE with respect to patch size ($\sqrt{p_n}$) and iteration index (k), respectively, for simultaneous CT-MRI construction in the porcine sample experiment. Referring to Figures 14a and 14b, RMSE quantifies the differences between the reconstructed and ground truth images with respect to various patch sizes, as well as the intermediate results as a function of the iteration index k (with $\sqrt{p_n} = 15$).

In Figure 14a, the square points (upper section of plot) are for CT, and the circle points (lower section of plot) are for MRI. In Figure 14b, the square points (upper section of plot) are for CT-MRI-based CT reconstruction, and the circle points (lower section of plot) are for CT-MRI-based MRI reconstruction, the upper dotted line is for TV-based CT reconstruction, and the lower dotted line is for TV-based MRI reconstruction.

Figures 15a and 15b show a quantitative summary of the RMSE and structural similarity index (SSIM), respectively, for the mNCAT, VHP, and porcine sample experiments. In each data grouping (mNCAT, VHP, and porcine in each of Figures 15a and 15b), the left-most bar is for MRI result with CS, the second-from-the-left bar is for MRI result with SC and CS, the second-from-the-right bar is for CT result with CS, and the right-most bar is for CT result with SC and CS.

Based on the results, (e.g., Figure 7a), the optimal patch size was 5 × 5 pixels for the mNCAT experiment. The same approach was applied to the VHP and porcine experiments, both of which yielded the optimal patch size 15×15 pixels, as shown in Figures 11a and 14a, respectively. In each modality-specific reconstruction, the relaxation parameter α was used to balance the regularization effects of TV in an image and TV between images in Equations (7) and (8). Figure 7b shows the RMSE results with different α values. The optimized setting of the parameter α is affected by many factors, such as estimation accuracy, measurement noise, and others. Without loss of generality, in our experiments, α was empirically set to $\alpha = 0.5$.

With the well-trained CT-MRI image pair table, the simultaneous CT-MRI reconstruction method was compared with the conventional TV-based method, and the residual errors relative to the ground truths were displayed for the mNCAT, VHP, and porcine experiments in Figures 6, 9, and 12, respectively. Enlarged views of local regions, denoted by a red box in Figures 9 and 12, were plotted and compared with the ground truth images for VHP and porcine experiments in Figures 10 and 13, respectively. In Figure 8, an error analysis on the mNCAT experiment was performed. Registration errors between CT and MRI images were considered, represented by $(\Delta x, \Delta y)$ in the unit of pixel. Figures 8a and 8b show the results for different registration errors, and Figures 8c and 8d present the results from 3%, 5%, and 10% noisy measurements. In the experiments, the Gaussian-type noise was added into both the CT and MRI measurements.

Referring again to Figures 6, 8, 9, 11, and 12, it is clear that there are less intensity fluctuations in the residual errors of images reconstructed with the simultaneous CT-MRI reconstruction method, as compared with the conventional TV-based reconstruction methods. The RMSE index quantified results are shown in Figures 7c, 11b, and 14b. The intermediate reconstruction results of the proposed method, quantified with RMSE, are plotted with respect to the iteration index k for comparison. The results suggest that the simultaneous CT-MRI reconstruction algorithm has a fast convergence speed: two outer iterations appeared optimal in the experiments. In each loop, two optimization problems (see Equations (6) and (7)) were involved, which are started with zero initial guesses and accordingly estimated images. As compared with conventional iterative reconstructions for CT and MRI, the simultaneous CT-MRI reconstruction method can require an extra patch searching step and two iterations.

In Figures 10 and 11, local regions in the CT images from the TV-based and simultaneous CT-MRI reconstructions are enlarged and compared with the ground truth images. By utilizing the physical correlation between CT and MRI images, the simultaneous CT-MRI performance was good even though the view number of the CT subsystem was significantly lower than that of a conventional CT scan.

The reconstructions for the mNCAT, VHP, and porcine experiments were quantitatively compared. The results are summarized in Figure 15. In these three experiments, the simultaneous CT-MRI image reconstruction using the SC and CS framework always provided better reconstructions compared with the individual reconstructions.

EXAMPLE 2

A numerical simulation was run to perform simultaneous CT-MRI image reconstruction. CT and MRI datasets were derived from the Visible Human Project (VHP). The MRI dataset included $T2$-weighted images. The CT and MRI images were deformed to be different from the atlas and reprojected to simulate CT and MRI measurements. In the CT setup, 15 sources were assumed. In the MRI setup, the k-space was spirally sampled only in a low-frequency area.

Figure 22 shows images of the interior scan with 15 views. Each image in the first row is CT, and each image in the second row is for MRI. The first column is ground truth for the entire scan; the second column is ground truth for the ROI in the circle in the first column images; the third column is using separate CT (first row) and MRI (second row) reconstruction; and the fourth column is using joint reconstruction. Referring to Figure 22, the results from the joint CT-MRI reconstruction were good.

When the term “about” is used herein, in conjunction with a numerical value, it is understood that the value can be in a range of 95% of the value to 105% of the value, i.e. the value can be +/- 5% of the stated value. For example, “about 1 kg” means from 0.95 kg to 1.05 kg.

It should be understood that the examples and embodiments described herein are for illustrative purposes only and that various modifications or changes in light thereof will be suggested to persons skilled in the art and are to be included within the spirit and purview of this application.

All patents, patent applications, provisional applications, and publications referred to or cited herein (including those in the “References” section) are incorporated by reference in their entirety, including all figures and tables, to the extent they are not inconsistent with the explicit teachings of this specification.

REFERENCES

1. CDC Data and Statistics, 2015.
2. D. Fausti, R. I. Tobey, N. Dean, S. Kaiser, A. Dienst, M. C. Homann, S. Pyon, T. Takayama, H. Takagi, and A. Cavalleri, “Light-induced superconductivity in a Stripe-ordered cuprate,” Science 331, 189–191 (2011).
3. R. Mankowsky, A. Subedi, M. Forst, S. O. Mariager, M. Chollet, H. T. Lemke, J. S. Robinson, J. M. Glownia, M. P. Minitti, A. Frano, M. Fechner, N. A. Spaldin, T. Loew, B. Keimer, A. Georges, and A. Cavalleri, “Nonlinear lattice dynamics as a basis for enhanced superconductivity in YBa2Cu3O6.5,” Nature 516, 71–73 (2014).
4. C. Z. Cooley, J. P. Stockmann, B. D. Armstrong, M. Sarracanie, M. H. Lev, M. S. Rosen, and L. L. Wald, “Two-dimensional imaging in a lightweight portable MRI scanner without gradient coils,” Magn. Reson. Med. 73, 872–883 (2015).
5. D. Ma, V. Gulani, N. Seiberlich, K. Liu, J. L. Sunshine, J. L. Duerk, and M. A. Griswold, “Magnetic resonance fingerprinting,” Nature 495, 187–192 (2013).
6. G. Wang and H. Y. Yu, “The meaning of interior tomography,” Phys. Med. Biol. 58, R161–R186 (2013).
7. S. R. Cherry, “Multimodality Imaging: Beyond PET/CT and SPECT/CT,” Semin. Nucl. Med. 39, 348–353 (2009).
8. T. Pfluger, C. la Fougere, J. Stauss, R. Santos, C. Vollmar, and K. Hahn, “Combined scanners (PET/CT, SPECT/CT) versus multimodality imaging with separated systems,” Der Radiologe 44, 1105–1112 (2004).
9. D. Papathanassiou and J.-C. Liehn, “The growing development of multimodality imaging in oncology,” Crit. Rev. Oncol./Hematol. 68, 60–65 (2008).
10. J. C. Plana, M. Galderisi, A. Barac, M. S. Ewer, B. Ky, M. Scherrer-Crosbie, J. Ganame, I. A. Sebag, D. A. Agler, and L. P. Badano, “Expert consensus for multimodality imaging evaluation of adult patients during and after cancer therapy: A report from the American Society of Echocardiography and the European Association of Cardiovascular Imaging,” J. Am. Soc. Echocardiogr. 27, 911–939 (2014).
11. J. A. Schaar, F. Mastik, E. Regar, C. A. den Uil, F. J. Gijsen, J. J. Wentzel, P. W. Serruys, and A. F. van der Stehen, “Current diagnostic modalities for vulnerable plaque detection,” Curr. Pharm. Des. 13, 995–1001 (2007).
12. C. Yuan, T. S. Hatsukami, and K. D. Obrien, “High-resolution magnetic resonance imaging of normal and atherosclerotic human coronary arteries ex vivo: Discrimination of plaque tissue components,” J. Invest. Med. 49, 491–499 (2001).

13. J. C. Miller, M. H. Lev, L. H. Schwamm, J. H. Thrall, and S. I. Lee, "Functional CT and MRimaging for evaluation of acute stroke," J. Am. Coll. Radiol. 5, 67–70 (2008).
14. A. Li, Y. Zheng, J. Yu, Z. Wang, Y. Yang, W. Wu, D. Guo, and H. Ran, "Superparamagnetic perfluorooctylbromide nanoparticles as a multimodal contrast agent for US, MR, and CT imaging," Acta Radiol. 54, 278–283 (2013).
15. J. O'Connor, P. Tofts, K. Miles, L. Parkes, G. Thompson, and A. Jackson, "Dynamic contrast-enhanced imaging techniques: CT and MRI," Br. J. Radiol. 84, S112–S120 (2014).
16. J. Kallehauge, T. Nielsen, S. Haack, D. A. Peters, S. Mohamed, L. Fokdal, J. C. Lindegaard, D. C. Hansen, F. Rasmussen, and K. Tanderup, "Voxelwise comparison of perfusion parameters estimated using dynamic contrast enhanced (DCE) computed tomography and DCE-magnetic resonance imaging in locally advanced cervical cancer," Acta Oncol. 52, 1360–1368 (2013).
17. C. Cuenod and D. Balvay, "Perfusion and vascular permeability: Basic concepts and measurement in DCE-CT and DCE-MRI," Diagn. Interventional Imaging 94, 1187–1204 (2013).
18. C. S. Ng, J. C. Waterton, V. Kundra, D. Brammer, M. Ravoori, L. Han, W. Wei, S. Klumpp, V. E. Johnson, and E. F. Jackson, "Reproducibility and comparison of DCE-MRI and DCE-CT perfusion parameters in a rat tumor model," Technol. Cancer Res. Treat. 11, 279–288 (2012).
19. M. A. Jacobs, R. Ouwerkerk, A. C. Wolf, E. Gabrielson, H. Warzecha, S. Jeter, D. A. Bluemke, R.Wahl, and V. Stearns, "Monitoring of neoadjuvant chemotherapy using multiparametric, 23Na sodium MR, and multimodality (PET/CT/MRI) imaging in locally advanced breast cancer," Breast Cancer Res. Treat. 128, 119–126 (2011).
20. M. A. Jacobs, A. C. Wolf, K. Macura, V. Stearns, R. Ouwerkerk, R. El Khouli, D. A. Bluemke, and R. Wahl, "Multiparametric and multimodality functional radiological imaging for breast cancer diagnosis and early treatment response assessment," J. Natl. Cancer Inst. Monogr. 2015, 40–46.
21. J. S. Suri, C. Yuan, and D. L. Wilson, Plaque Imaging: Pixel to Molecular Level (IOS, 2005).
22. G. Wang, Y. B. Ye, and H. Y. Yu, "Approximate and exact cone-beam reconstruction with standard and non-standard spiral scanning," Phys. Med. Biol. 52, R1–R13 (2007).

23. F. Natterer, The Mathematics of Computerized Tomography (B.G. Teubner, Stuttgart, 1986).
24. Y. Ye, H. Yu,Y. Wei, and G. Wang, "A general local reconstruction approach based on a truncated hilbert transform," Int. J. Biomed. Imaging 2007, 63634.
25. H. Kudo, M. Courdurier, F. Noo, and M. Defrise, "Tiny a priori knowledge solves the interior problem in computed tomography," Phys. Med. Biol. 53, 2207–2231 (2008).
26. H. Yu, J. Yang, M. Jiang, and G. Wang, "Supplemental analysis on compressed sensing based interior tomography," Phys. Med. Biol. 54, N425–N432 (2009).
27. W. Han, H. Yu, and G. Wang, "A general total variation minimization theorem for compressed sensing based interior tomography," Int. J. Biomed. Imaging 2009, 125871.
28. H.Yu and G.Wang, "Compressed sensing based interior tomography," Phys. Med. Biol. 54, 2791–2805 (2009).
29. G.Wang and H.Y.Yu, "Can interior tomography outperform lambda tomography?" Proc. Natl. Acad. Sci. U. S. A. 107, E92–E93 (2010).
30. H. Yu, G. Wang, J. Hsieh, D. W. Entrikin, S. Ellis, B. Liu, and J. J. Carr, "Compressive sensing-based interior tomography: Preliminary clinical application," J. Comput. Assisted Tomogr. 35, 762–764 (2011).
31. J. Yang, H. Yu, M. Jiang, and G. Wang, "High-order total variation minimization for interior SPECT," Inverse Probl. 28, 015001(2012).
32. H. Yu, J. Yang, M. Jiang, and G. Wang, "Interior SPECT- exact and stable ROI reconstruction from uniformly attenuated local projections," Commun. Numer. Methods Eng. 25, 693–710 (2009).
33. R. Paquin, P. Pelupessy, and G. Bodenhausen, "Cross-encoded magnetic resonance imaging in inhomogeneous fields," J. Magn. Reson. 201, 199–204 (2009).
34. V. E. Arpinar and B. M. Eyuboglu, "Magnetic resonance imaging in inhomogeneous magnetic fields with noisy signal," in 4th European Conference of the International Federation for Medical and Biological Engineering (2009), Vol. 22, pp. 410–413.
35. R. Fahrig, K. Butts, J. A. Rowlands, R. Saunders, J. Stanton, G. M. Stevens, B. L. Daniel, Z. Wen, D. L. Ergun, and N. J. Pelc, "A truly hybrid interventional MR/x-ray system: Feasibility demonstration," J. Magn. Reson. Imaging 13, 294–300 (2001).
36. R. Fahrig, Z. Wen, A. Ganguly, G. DeCrescenzo, J. A. Rowlands, G. M. Stevens, R. F. Saunders, and N. J. Pelc, "Performance of a static-anode/flatpanel x-ray

fluoroscopy system in a diagnostic strength magnetic field: A truly hybrid x-ray/MR imaging system," Med. Phys. 32, 1775–1784 (2005).

37. Z. Wen, R. Fahrig, S. Conolly, and N. J. Pelc, "Investigation of electron trajectories of an x-ray tube in magnetic fields of MR scanners," Med. Phys. 34, 2048–2058 (2007).
38. Z.Wen, R. Fahrig, S. T.Williams, and N. J. Pelc, "Shimming with permanent magnets for the x-ray detector in a hybrid x-ray/MRsystem," Med. Phys. 35, 3895–3902 (2008).
39. A. Jena, S. Taneja, and A. Jha, "Simultaneous PET/MRI: Impact on cancer management-A comprehensive review of cases," Indian J. Radiol. Imaging 24, 107–116 (2014).
40. M. Hofmann, B. Pichler, B. Scholkopf, and T. Beyer, "Towards quantitative PET/MRI: A review of MR-based attenuation correction techniques," Eur. J. Nucl. Med. Mol. Imaging 36(Suppl. 1), S93–S104 (2009).
41. D. Faul, Fully Integrated MRI and PET Imaging, 2013.
42. S.Vandenberghe and P. K. Marsden, "PET-MRI:Areviewof challenges and solutions in the development of integrated multimodality imaging," Phys.Med. Biol. 60, R115–R154 (2015).
43. B.W. Raaymakers, J. J. Lagendijk, J. Overweg, J. G.Kok, A. J. Raaijmakers, E. M. Kerkhof, R.W. van der Put, I. Meijsing, S. P. Crijns, F. Benedosso, M. van Vulpen, C.H. de Graa↵, J. Allen, and K. J. Brown, "Integrating a 1.5 T MRI scanner with a 6 MV accelerator: Proof of concept," Phys. Med. Biol. 54, N229–N237 (2009).
44. S. Crijns and B. Raaymakers, "From static to dynamic 1.5 T MRI-Linac prototype: Impact of gantry position related magnetic field variation on image fidelity," Phys. Med. Biol. 59, 3241–3247 (2014).
45. F. Tang, H. S. Lopez, F. Freschi, E. Smith, Y. Li, M. Fuentes, F. Liu, M. Repetto, and S. Crozier, "Skin and proximity e↵ects in the conductors of split gradient coils for a hybrid Linac-MRI scanner," J. Magn. Reson. 242, 86–94 (2014).
46. L. Liu, A. Trakic, H. Sanchez-Lopez, F. Liu, and S. Crozier, "An analysis of the gradient-induced electric fields and current densities in human models when situated in a hybrid MRI-LINAC system," Phys. Med. Biol. 59, 233–245 (2014).
47. A. Trakic, L. Limei, H. Sanchez lopez, L. Zilberti, L. Feng, and S. Crozier, "Numerical safety study of currents induced in the patient during rotations in the static field produced by a hybrid MRI-LINAC system," IEEE Trans. Biomed. Eng. 61, 784–793 (2014).

48. Z. Q. Chen, X. Jin, L. Li, and G. Wang, “A limited-angle CT reconstruction method based on anisotropic TV minimization,” Phys. Med. Biol. 58, 2119–2141 (2013).
49. 73M. J. Ehrhardt, K. Thielemans, L. Pizarro, D. Atkinson, S. Ourselin, B. F. Hutton, and S. R. Arridge, “Joint reconstruction of PETMRI by exploiting structural similarity,” Inverse Probl. 31, 015001 (2015).
50. J. Sjolund, D. Forsberg, M. Andersson, and H. Knutsson, “Generating patient specific pseudo-CT of the head from MR using atlas-based regression,” Phys. Med. Biol. 60, 825–839 (2015).
51. S. T. Roweis and L. K. Saul, “Nonlinear dimensionality reduction by locally linear embedding,” Science 290, 2323–2326 (2000).
52. M. T. Truijman, R. M. Kwee, R. H. van Hoof, E. Hermeling, R. J. van Oostenbrugge,W. H. Mess,W. H. Backes, M. J. Daemen, J. Bucerius, J. E. Wildberger, and M. E. Kooi, “Combined 18F-FDG PET-CT and DCE-MRI to assess inflammation and microvascularization in atherosclerotic plaques,” Stroke 44, 3568–3570 (2013).
53. W. Theodore *et al.*, “Pathology of temporal lobe foci correlation with CT, MRI, and PET,” *Neurology*, vol. 40, pp. 797–797, 1990.
54. A. E. Hanbidge, “Cancer of the pancreas: The best image for early detection—CT, MRI, PET or US?” *Can. J. Gastroenterol.*, vol. 16, pp. 101–105, 2002.
55. H. Stefan *et al.*, “Functional and morphological abnormalities in temporal lobe epilepsy: A comparison of interictal and ictal EEG, CT,MRI, SPECT and PET,” *J. Neurol.*, vol. 234, pp. 377–384, 1987.
56. C. P. Karger *et al.*, “Stereotactic imaging for radiotherapy: Accuracy of CT,MRI, PET and SPECT,” *Phys.Med. Biol.*, vol. 48, pp. 211–221, 2003.
57. S. R. Cherry, “Multimodality imaging: Beyond PET/CT and SPECT/CT,” in *Proc. Semin. Nucl. Med.*, 2009, pp. 348–353.
58. W. Cong *et al.*, “X-ray micro-modulated luminescence tomography (XMLT),” *Opt. Exp.*, vol. 22, pp. 5572–5580, 2014.
59. T. Beyer *et al.*, “A combined PET/CT scanner for clinical oncology,”*J. Nucl. Med.*, vol. 41, pp. 1369–1379, 2000. [8] P. G. Kluetz *et al.*, “Combined PET/CT imaging in oncology: Impact on patient management,” *Clin. Positron Imag.*, vol. 3, pp. 223–230, 2000.
60. T. M. Blodgett *et al.*, “PET/CT: Form and function 1,” *Radiology*, vol. 242, pp. 360–385, 2007.

61. A. Boss *et al.*, “Hybrid PET/MRI of intracranial masses: Initial experiences and comparison to PET/CT,” *J. Nucl. Med.*, vol. 51, pp. 1198–1205, 2010.
62. M. S. Judenhofer *et al.*, “Simultaneous PET-MRI: A new approach for functional and morphological imaging,” *Nature Med.*, vol. 14, pp. 459–465, 2008.
63. D. A. Torigian *et al.*, “PET/MR imaging: Technical aspects and potential clinical applications,” *Radiology*, vol. 267, pp. 26–44, 2013.
64. G. Wang *et al.*, “Towards omni-tomography—Grand fusion of multiple modalities for simultaneous interior tomography,” *PloS One*, vol. 7, p. e39700, 2012.
65. G. Wang *et al.*, “Marriage of CT and MRI for vulnerable plaque characterization,”*Imag. Med.*, vol. 5, pp. 95–97, 2013.
66. Y. Lu *et al.*, “Unified dual-modality image reconstruction with dual dictionaries,”*Proc. SPIE, Opt. Eng. Appl.*, vol. 8506, pp. 85061V-1–85061V-7, 2012.
67. C. K. Glide-Hurst *et al.*, “MRI/CT is the future of radiotherapy treatment planning,” *Med. Phys.*, vol. 41, p. 110601, 2014.
68. Y. Xi *et al.*, “United iterative reconstruction for spectral computed tomography,”*IEEE Trans. Med. Imag.*, vol. 34, no. 3, pp. 769–778, Mar. 2015.
69. Y. Xi *et al.*, “A hybrid CT-MRI reconstruction method,” presented at the IEEE Int. Symp. Biomedical Imaging, Beijing, China, 2014.
70. G. Wang, “First CT-MRI Scanner for multi-dimensional synchrony and multi-physical coupling,” *arXiv preprint*, vol. 1402, p. 2647, 2014.
71. G. Wang and H. Yu, “The meaning of interior tomography,” *Phys. Med. Biol.*, vol. 58, pp. R161–R181, 2013.
72. H. Yu *et al.*, “Compressive sampling based interior reconstruction for dynamic carbon nanotube micro-CT,” *J. X-Ray Sci. Technol.*, vol. 17, pp. 295–303, 2009.
73. F. Knoll *et al.*, “Joint reconstruction of simultaneously acquired MRPET data with multi sensor compressed sensing based on a joint sparsity constraint,” *EJNMMI Phys.*, vol. 1, pp. 1–2, 2014.
74. S. T. Roweis and L. K. Saul, “Nonlinear dimensionality reduction by locally linear embedding,” *Science*, vol. 290, pp. 2323–2326, 2000.
75. E. M. Haacke *et al.*, *Magnetic Resonance Imaging*. New York, NY, USA: Wiley, 1999.
76. G. Wang *et al.*, “An outlook on X-ray CT research and development,”*Med. Phys.*, vol. 35, pp. 1051–1064, 2008.

77. R. Baraniuk, “Compressive sensing,” *IEEE Signal Process. Mag.*, vol. 24, no. 4, pp. 118–121, Jul. 2007.
78. H. Yu and G. Wang, “Compressed sensing based interior tomography,” *Phys. Med. Biol.*, vol. 54, pp. 2791–2805, 2009.
79. L. I. Rudin *et al.*, “Nonlinear total variation based noise removal algorithms,”*Phys. D, Nonlinear Phenom.*, vol. 60, pp. 259–268, 1992.
80. A. Chambolle, “An algorithm for total variation minimization and applications,”*J. Math. Imag. Vis.*, vol. 20, pp. 89–97, 2004.
81. A. Myronenko and S. Xubo, “Intensity-based image registration by minimizing residual complexity,” *IEEE Trans. Med. Imag.*, vol. 29, no. 11, pp. 1882–1891, Nov. 2010.
82. T. Goldstein and S. Osher, “The split Bregman method for L1-regularized problems,” *SIAM J. Imag. Sci.*, vol. 2, pp. 323–343, 2009.
83. W. P. Segars et al., “Development and application of the new dynamic Nurbs-based Cardiac-Torso (NCAT) phantom,” *J. Nucl. Med.*, vol. 42, pp.7p–7p, 2001.
84. M. J. Ackerman, “The visible human project,” *Proc. IEEE*, vol. 86, no. 3, pp. 504–511, Mar. 1998.
85. N. Levinson, “The Wiener RMS (root mean square) error criterion in filter design and prediction,” *J. Math. Phys. Mass. Inst. Tech.*, vol. 25, pp.261–278, 1947.
86. Z. Wang *et al.*, “Image quality assessment: From error visibility to structural similarity,” *IEEE Trans. Image Process.*, vol. 13, no. 4, pp. 600–612, Apr. 2004.
87. M. Elad and M. Aharon, “Image denoising via sparse and redundant representations over learned dictionaries,” *IEEE Trans. Image Process.*, vol. 15, no. 12, pp. 3736–3745, Dec. 2006.
88. Q. Xu *et al.*, “Low-dose X-ray CT reconstruction via dictionary learning,”*IEEE Trans. Med. Imag.*, vol. 31, no. 9, pp. 1682–1697, Sep. 2012.
89. Wang et al., International Patent Application Publication No. WO2016/106348.
90. Wang et al., U.S. Patent Application Publication No. 2015/0157286.
91. Wang et al., U.S. Patent Application Publication No. 2015/0170361.
92. Wang et al., U.S. Patent Application Publication No. 2015/0193927.
93. Wang et al., International Patent Application Publication No. WO2015/164405.
94. Wang et al., U.S. Patent Application Publication No. 2016/0113602.
95. Wang et al., U.S. Patent Application Publication No. 2016/0135769.
96. Wang et al., U.S. Patent Application Publication No. 2016/0166852.

97. Wang et al., International Patent Application Publication No. WO2016/106348.
98. Wang et al., International Patent Application No. PCT/US2016/014769.
99. Wang et al., International Patent Application No. PCT/US2016/023460.
100. Wang et al., International Patent Application No. PCT/US2016/036057.
101. Wang et al., International Patent Application No. PCT/US2016/043154.
102. Wang et al., International Patent Application No. PCT/US2016/044287.

CLAIMS

What is claimed is:

1. A system for simultaneous computed tomography (CT)-magnetic resonance imaging (MRI), the system comprising:

a CT subsystem for obtaining CT data;

an MRI subsystem for obtaining MRI data;

at least one processor; and

a machine-readable medium, in operable communication with the CT subsystem, the MRI subsystem, and the at least one processor, having machine-executable instructions stored thereon that, when executed by the at least one processor, perform a method of reconstructing CT and MRI images, the method comprising:

i) reconstructing a CT image $\mathbf{u}_{\mathrm{CT}}$ from the CT data;

ii) reconstructing an MRI image $\mathbf{u}_{\mathrm{MRI}}$ from the MRI data;

iii) setting an iteration step $k = 0$;

iv) transforming a CT-MRI dataset $\mathbf{T}_{\mathrm{CT\text{-}MRI}}$ by the $\mathbf{u}_{\mathrm{CT}}$ and $\mathbf{u}_{\mathrm{MRI}}$;

v) estimating the corresponded CT-MRI image $\mathbf{u}\frac{\mathrm{est}}{\mathrm{CT}}$ and $\mathbf{u}\frac{\mathrm{est}}{\mathrm{MRI}}$ according to $\mathbf{u}_{\mathrm{CT}}$ and $\mathbf{u}_{\mathrm{MRI}}$ aided by the CT-MRI dataset $\mathbf{T}_{\mathrm{CT\text{-}MRI}}$;

vi) reconstructing the CT image $\mathbf{u}_{\mathrm{CT}}$ with $\mathbf{u}\frac{\mathrm{est}}{\mathrm{CT}}$ and the CT data;

vii) reconstructing the MRI image $\mathbf{u}_{\mathrm{MRI}}$ with $\mathbf{u}\frac{\mathrm{est}}{\mathrm{MRI}}$ and the MRI data;

viii) setting $k = k + 1$; and

ix) repeating steps iv) – viii) until meeting stop criteria, at which point the current $\mathbf{u}\frac{\mathrm{est}}{\mathrm{CT}}$ is the reconstructed CT image and the current $\mathbf{u}\frac{\mathrm{est}}{\mathrm{MRI}}$ is the reconstructed MRI image.

2. The system according to claim 1, wherein reconstructing a CT image $\mathbf{u}_{\mathrm{CT}}$ from the CT data comprises using the following equation:

$$\min_{\mathbf{u}_{CT}} \|\mathbf{u}_{CT}\|_{TV} \ \text{s.t.} \mathbf{M}\mathbf{u}_{CT} = \mathbf{f}$$
,

where $\mathbf{M}$ is a system matrix, $\mathbf{f}$ is the (line integral) CT data (after preprocessing), and $\|\cdot\|_{TV}$ represents a total variation (TV) transformation.

3. The system according to any of claims 1-2, wherein reconstructing an MRI image $\mathbf{u}_{MRI}$ from the MRI data comprises using the following equation:

$$\min_{\mathbf{u}_{MRI}} \|\mathbf{u}_{MRI}\|_{TV} \quad \text{s.t.} \mathbf{RFu}_{MRI} = \mathbf{g},$$

where $\mathbf{F}$ denotes the Fourier transform, $\mathbf{R}$ is a sampling mask in the k-space, $\mathbf{g}$ is the MRI data, and $\|\cdot\|_{TV}$ represents a total variation (TV) transformation.

4. The system according to any of claims 1-3, wherein estimating the corresponded CT-MRI image comprises using a structural coupling (SC) method.

5. The system according to claim 4, wherein the SC method comprises:

a) decomposing $\mathbf{u}_{CT}$ into patches $\mathbf{p}^j_{CT} = \mathbf{E}_j\ \mathbf{u}_{CT}$;

b) decomposing $\mathbf{u}_{MRI}$ into patches $\mathbf{p}^j_{MRI} = \mathbf{E}_j\ \mathbf{u}_{MRI}$;

c) optimizing the following equation by finding K-best suitable patches $\{\mathbf{p}^j_{CT,i}\}$ and $\{\mathbf{p}^j_{MRI,i}\}$, and their weights $\{w_i\}$ in $\mathbf{T}_{CT}$ and $\mathbf{T}_{MRI}$ to represent $\mathbf{p}^j_{CT}$ and $\mathbf{p}^j_{MRI}$

$$\min_{\beta_i} \left\| p_{MRI} - \sum_i w_i T_{MRI} \beta_i \right\|_2^2 + \left\| p_{CT} - \sum_i w_i T_{CT} \beta_i \right\|_2^2,$$

where w_i equals the average of CT and MRI weightings calculated according to the below equation, $w_i = (w_{CT,i} + w_{MRI,i})/2$, and β_i identifies surrounding high-dimensional data points,

$$w'_{*,i} = \exp\left(-\|\mathbf{p}_* - \mathbf{p}_{*,i}\|_2^2 / h^2\right) \text{ and } w_{*,i} = w'_{*,i} / \sum_i^K w'_{*,i},$$

where h is an empirical value that controls contributions of involved patches, and K is the number of surrounding data points;

d) estimating CT and MRI image patches with the corresponded CT and MRI image pairs in $\mathbf{T}_{CT\text{-}MRI}$ and new weights $\{w_i\}$,

$$\mathbf{p}^j_{new,CT} \approx \sum_i^K w_i \mathbf{p}^j_{CT,i},\ \mathbf{p}^j_{new,MRI} \approx \sum_i^K w_i \mathbf{p}^j_{MRI,i};$$

e) estimating the corresponded CT image with $\mathbf{p}^j_{\text{new,CT}}$,

$$\mathbf{u}_{\mathrm{CT}}^{est} = \left(\sum_j \mathbf{E}_j^T \mathbf{E}_j\right)^{-1} \left(\sum_j \mathbf{E}_j^T \mathbf{p}^j_{\mathrm{new,CT}}\right)$$; and

f) estimating the corresponded CT image with $\mathbf{p}^j_{\text{new,CT}}$,

$$\mathbf{u}_{\mathrm{MRI}}^{est} = \left(\sum_j \mathbf{E}_j^T \mathbf{E}_j\right)^{-1} \left(\sum_j \mathbf{E}_j^T \mathbf{p}^j_{\mathrm{new,MRI}}\right).$$

6. The system according to any of claims 1-5, wherein reconstructing the CT image $\mathbf{u}_{\text{CT}}$ with $\mathbf{u}_{\text{CT}}^{\text{est}}$ and the CT data comprises using the following equation,

$$\min_{\mathbf{u}_{\mathrm{CT}}} (1-\alpha)\left\|\mathbf{u}_{\mathrm{CT}}\right\|_{\mathrm{TV}} + \alpha\left\|\mathbf{u}_{\mathrm{CT}} - \mathbf{u}_{\mathrm{CT}}^{\mathrm{est}}\right\|_{\mathrm{TV}} \ \mathrm{s.t.}\mathbf{M}\mathbf{u}_{\mathrm{CT}} = \mathbf{f},$$

where $\mathbf{M}$ is a system matrix, $\mathbf{f}$ is the (line integral) CT data (after preprocessing), α is a relaxation parameter, and $\|\cdot\|_{\text{TV}}$ represents a total variation (TV) transformation.

7. The system according to any of claims 1-6, wherein reconstructing the MRI image $\mathbf{u}_{\text{MRI}}$ with $\mathbf{u}_{\text{MRI}}^{\text{est}}$ and the MRI data comprises using the following equation,

$$\min_{\mathbf{u}_{\mathrm{MRI}}} (1-\alpha)\left\|\mathbf{u}_{\mathrm{MRI}}\right\|_{\mathrm{TV}} + \alpha\left\|\mathbf{u}_{\mathrm{MRI}} - \mathbf{u}_{\mathrm{MRI}}^{\mathrm{est}}\right\|_{\mathrm{TV}}$$

$$\mathrm{s.t.}\mathbf{F}\mathbf{u}_{\mathrm{MRI}} = \mathbf{g},$$

where $\mathbf{F}$ denotes the Fourier transform, $\mathbf{R}$ is a sampling mask in the k-space, $\mathbf{g}$ is the MRI data, α is a relaxation parameter, and $\|\cdot\|_{\text{TV}}$ represents a total variation (TV) transformation.

8. The system according to any of claims 1-7, wherein steps iv) through vii) can be formulated as follows,

$$\min_{(\mathbf{u}_{CT},\mathbf{u}_{MRI},\beta)} \|\mathbf{u}_{CT}\|_{TV} + \lambda\|\mathbf{u}_{MRI}\|_{TV} + \gamma\sum_j \left(\left\|\mathbf{E}_j\mathbf{u}_{MRI} - \sum_i w_i\mathbf{T}_{MRI}\beta_{j,i}\right\|_2^2 + \left\|\mathbf{E}_j\mathbf{u}_{CT} - \sum_i w_i\mathbf{T}_{CT}\beta_{j,i}\right\|_2^2\right)$$

$$\text{s.t.}\,\mathbf{M}\mathbf{u}_{CT} = \mathbf{f},\quad \mathbf{R}\mathbf{F}\mathbf{u}_{MRI} = \mathbf{g},$$

where **E** is an operator to extract patches from an image, β determines which patch is selected for linear approximation by assigning appropriate weighting factors $\{w_i\}$, **M** is a system matrix, **f** is the (line integral) CT data (after preprocessing), **F** denotes the Fourier transform, **R** is a sampling mask in the k-space, **g** is the MRI data, and $\|\cdot\|_{TV}$ represents a total variation (TV) transformation.

9. The system according to any of claims 1-8, wherein estimating the corresponded CT-MRI image comprises using an SC method implemented using a hashing method to accelerate the patch searching process.

10. The system according to any of claims 1-9, wherein the method of reconstructing CT and MRI images further comprises utilizing prior knowledge of CT images.

11. The system according to claim 10, wherein the prior knowledge of CT images comprises information from a CT image atlas.

12. The system according to any of claims 10-11, wherein the prior knowledge of CT images is utilized in step i).

13. The system according to any of claims 1-12, wherein the method of reconstructing CT and MRI images further comprises utilizing prior knowledge of MRI images.

14. The system according to claim 13, wherein the prior knowledge of MRI images comprises information from an MRI image atlas.

15. The system according to any of claims 13-14, wherein the prior knowledge of MRI images is utilized in step i).

16. The system according to any of claims 1-15, wherein the MRI subsystem comprises superconducting magnets.

17. The system according claim 16, wherein the superconducting magnets are room temperature superconducting magnets.

18. The system according to any of claims 1-17, wherein the MRI subsystem comprises two donut shaped magnets facing each other.

19. The system according to any of claims 1-18, wherein the MRI subsystem comprises two hexagonal magnet arrays facing each other.

20. The system according to any of claims 1-19, wherein the CT subsystem and the MRI subsystem are seamlessly integrated with one another.

21. The system according to any of claims 1-20, wherein components of the CT subsystem are quasi-stationary.

22. The system according to claim 22, wherein X-ray sources and detectors of the CT subsystem are distributed face-to-face along a circle.

23. The system according to any of claims 1-22, wherein the CT data comprises only a few-view set of CT data.

24. The system according to any of claims 1-23, wherein the method of reconstructing CT and MRI images comprises using an SC method and a compressive sensing (CS) method.

25. A machine-readable medium, having machine-executable instructions stored thereon that, when executed by at least one processor, perform a method of reconstructing CT and MRI images, the method comprising:

i) reconstructing a CT image $\mathbf{u}_{CT}$ from CT data;

ii) reconstructing an MRI image $\mathbf{u}_{MRI}$ from MRI data;

iii) setting an iteration step $k = 0$;

iv) transforming a CT-MRI dataset $\mathbf{T}_{CT\text{-}MRI}$ by the $\mathbf{u}_{CT}$ and $\mathbf{u}_{MRI}$;

v) estimating the corresponded CT-MRI image $\mathbf{u}_{\mathrm{CT}}^{\mathrm{est}}$ and $\mathbf{u}_{\mathrm{MRI}}^{\mathrm{est}}$ according to $\mathbf{u}_{CT}$ and $\mathbf{u}_{MRI}$ aided by the CT-MRI dataset $\mathbf{T}_{CT\text{-}MRI}$;

vi) reconstructing the CT image $\mathbf{u}_{CT}$ with $\mathbf{u}_{\mathrm{CT}}^{\mathrm{est}}$ and the CT data;

vii) reconstructing the MRI image $\mathbf{u}_{MRI}$ with $\mathbf{u}_{\mathrm{MRI}}^{\mathrm{est}}$ and the MRI data;

viii) setting $k = k + 1$; and

ix) repeating steps iv) – viii) until meeting stop criteria, at which point the current $\mathbf{u}_{\mathrm{CT}}^{\mathrm{est}}$ is the reconstructed CT image and the current $\mathbf{u}_{\mathrm{MRI}}^{\mathrm{est}}$ is the reconstructed MRI image.

26. The machine-readable medium according to claim 25, wherein reconstructing a CT image $\mathbf{u}_{CT}$ from the CT data comprises using the following equation:

$$\min_{\mathbf{u}_{CT}} \|\mathbf{u}_{CT}\|_{TV} \ \text{s.t.} \mathbf{M}\mathbf{u}_{CT} = \mathbf{f},$$

where $\mathbf{M}$ is a system matrix, $\mathbf{f}$ is the (line integral) CT data (after preprocessing), and $\|\cdot\|_{TV}$ represents a total variation (TV) transformation.

27. The machine-readable medium according to any of claims 25-26, wherein reconstructing an MRI image $\mathbf{u}_{MRI}$ from the MRI data comprises using the following equation:

$$\min_{\mathbf{u}_{MRI}} \|\mathbf{u}_{MRI}\|_{TV} \ \ \text{s.t.} \mathbf{RFu}_{MRI} = \mathbf{g},$$

where **F** denotes the Fourier transform, **R** is a sampling mask in the k-space, **g** is the MRI data, and $\|\cdot\|_{TV}$ represents a total variation (TV) transformation.

28. The machine-readable medium stem according to any of claims 25-27, wherein estimating the corresponded CT-MRI image comprises using a structural coupling (SC) method.

29. The machine-readable medium according to claim 28, wherein the SC method comprises:

a) decomposing $\mathbf{u}_{CT}$ into patches $\mathbf{p}^j_{CT} = \mathbf{E}_j \mathbf{u}_{CT}$;

b) decomposing $\mathbf{u}_{MRI}$ into patches $\mathbf{p}^j_{MRI} = \mathbf{E}_j \mathbf{u}_{MRI}$;

c) optimizing the following equation by finding K-best suitable patches $\{\mathbf{p}^j_{CT,i}\}$ and $\{\mathbf{p}^j_{MRI,i}\}$, and their weights $\{w_i\}$ in $\mathbf{T}_{CT}$ and $\mathbf{T}_{MRI}$ to represent $\mathbf{p}^j_{CT}$ and $\mathbf{p}^j_{MRI}$

$$\min_{\beta_i} \left\| p_{MRI} - \sum_i w_i T_{MRI} \beta_i \right\|_2^2 + \left\| p_{CT} - \sum_i w_i T_{CT} \beta_i \right\|_2^2,$$

where w_i equals the average of CT and MRI weightings calculated according to the below equation, $w_i = (w_{CT,i} + w_{MRI,i})/2$, and β_i identifies surrounding high-dimensional data points,

$$w'_{*,i} = \exp\left(-\|\mathbf{p}_* - \mathbf{p}_{*,i}\|_2^2 / h^2\right) \text{ and } w_{*,i} = w'_{*,i} / \sum_i^K w'_{*,i},$$

where h is an empirical value that controls contributions of involved patches, and K is the number of surrounding data points;

d) estimating CT and MRI image patches with the corresponded CT and MRI image pairs in $\mathbf{T}_{CT\text{-}MRI}$ and new weights $\{w_i\}$,

$$\mathbf{p}^j_{new,CT} \approx \sum_i^K w_i \mathbf{p}^j_{CT,i}, \mathbf{p}^j_{new,MRI} \approx \sum_i^K w_i \mathbf{p}^j_{MRI,i};$$

e) estimating the corresponded CT image with $\mathbf{p}^j_{\text{new,CT}}$,

$$\mathbf{u}_{\mathrm{CT}}^{est} = \left(\sum_j \mathbf{E}_j^T \mathbf{E}_j\right)^{-1} \left(\sum_j \mathbf{E}_j^T \mathbf{p}_{\mathrm{new,CT}}^j\right)$$

; and

f) estimating the corresponded CT image with $\mathbf{p}^j_{\text{new,CT}}$,

$$\mathbf{u}_{\mathrm{MRI}}^{est} = \left(\sum_j \mathbf{E}_j^T \mathbf{E}_j\right)^{-1} \left(\sum_j \mathbf{E}_j^T \mathbf{p}_{\mathrm{new,MRI}}^j\right).$$

30. The machine-readable medium according to any of claims 25-29, wherein reconstructing the CT image $\mathbf{u}_{\mathrm{CT}}$ with $\mathbf{u}\frac{\text{est}}{\text{CT}}$ and the CT data comprises using the following equation,

$$\min_{\mathbf{u}_{CT}} (1-\alpha)\left\|\mathbf{u}_{CT}\right\|_{TV} + \alpha\left\|\mathbf{u}_{CT} - \mathbf{u}_{CT}^{est}\right\|_{TV} \text{ s.t.} \mathbf{M}\mathbf{u}_{CT} = \mathbf{f}$$

,

where $\mathbf{M}$ is a system matrix, $\mathbf{f}$ is the (line integral) CT data (after preprocessing), α is a relaxation parameter, and $\|\cdot\|_{\mathrm{TV}}$ represents a total variation (TV) transformation.

31. The machine-readable medium according to any of claims 25-30, wherein reconstructing the MRI image $\mathbf{u}_{\mathrm{MRI}}$ with $\mathbf{u}\frac{\text{est}}{\text{MRI}}$ and the MRI data comprises using the following equation,

$$\min_{\mathbf{u}_{MRI}} (1-\alpha)\left\|\mathbf{u}_{MRI}\right\|_{TV} + \alpha\left\|\mathbf{u}_{MRI} - \mathbf{u}_{MRI}^{est}\right\|_{TV}$$

$$\text{s.t.} \mathbf{F}\mathbf{u}_{MRI} = \mathbf{g}$$

,

where $\mathbf{F}$ denotes the Fourier transform, $\mathbf{R}$ is a sampling mask in the k-space, $\mathbf{g}$ is the MRI data, α is a relaxation parameter, and $\|\cdot\|_{\mathrm{TV}}$ represents a total variation (TV) transformation.

32. The machine-readable medium according to any of claims 25-31, wherein steps iv) through vii) can be formulated as follows,

$$\min_{(\mathbf{u}_{CT},\mathbf{u}_{MRI},\beta)} \|\mathbf{u}_{CT}\|_{TV} + \lambda\|\mathbf{u}_{MRI}\|_{TV} + \gamma\sum_j \left(\left\| \mathbf{E}_j\mathbf{u}_{MRI} - \sum_i w_i \mathbf{T}_{MRI}\beta_{j,i} \right\|_2^2 + \left\| \mathbf{E}_j\mathbf{u}_{CT} - \sum_i w_i \mathbf{T}_{CT}\beta_{j,i} \right\|_2^2 \right)$$
$$\text{s.t.}\ \mathbf{M}\mathbf{u}_{CT} = \mathbf{f},\quad \mathbf{RF}\mathbf{u}_{MRI} = \mathbf{g}$$
,

where **E** is an operator to extract patches from an image, β determines which patch is selected for linear approximation by assigning appropriate weighting factors $\{w_i\}$, **M** is a system matrix, **f** is the (line integral) CT data (after preprocessing), **F** denotes the Fourier transform, **R** is a sampling mask in the k-space, **g** is the MRI data, and $\|\cdot\|_{TV}$ represents a total variation (TV) transformation.

33. The machine-readable medium according to any of claims 25-32, wherein estimating the corresponded CT-MRI image comprises using an SC method implemented using a hashing method to accelerate the patch searching process.

34. The machine-readable medium according to any of claims 25-33, wherein the method of reconstructing CT and MRI images further comprises utilizing prior knowledge of CT images.

35. The machine-readable medium according to claim 34, wherein the prior knowledge of CT images comprises information from a CT image atlas.

36. The machine-readable medium according to any of claims 34-35, wherein the prior knowledge of CT images is utilized in step i).

37. The machine-readable medium according to any of claims 25-36, wherein the method of reconstructing CT and MRI images further comprises utilizing prior knowledge of MRI images.

38. The machine-readable medium according to claim 37, wherein the prior knowledge of MRI images comprises information from an MRI image atlas.

39. The machine-readable medium according to any of claims 37-38, wherein the prior knowledge of MRI images is utilized in step i).

40. The machine-readable medium according to any of claims 25-39, wherein the CT data comprises only a few-view set of CT data.

41. The machine-readable medium according to any of claims 25-40, wherein the method of reconstructing CT and MRI images comprises using an SC method and a compressive sensing (CS) method.

42. A method of reconstructing CT and MRI images, the method comprising:

i) reconstructing a CT image $\mathbf{u}_{\mathrm{CT}}$ from CT data;

ii) reconstructing an MRI image $\mathbf{u}_{\mathrm{MRI}}$ from MRI data;

iii) setting an iteration step $k = 0$;

iv) transforming a CT-MRI dataset $\mathbf{T}_{\text{CT-MRI}}$ by the $\mathbf{u}_{\mathrm{CT}}$ and $\mathbf{u}_{\mathrm{MRI}}$;

v) estimating the corresponded CT-MRI image $\mathbf{u}\frac{\mathrm{est}}{\mathrm{CT}}$ and $\mathbf{u}\frac{\mathrm{est}}{\mathrm{MRI}}$ according to $\mathbf{u}_{\mathrm{CT}}$ and $\mathbf{u}_{\mathrm{MRI}}$ aided by the CT-MRI dataset $\mathbf{T}_{\text{CT-MRI}}$;

vi) reconstructing the CT image $\mathbf{u}_{\mathrm{CT}}$ with $\mathbf{u}\frac{\mathrm{est}}{\mathrm{CT}}$ and the CT data;

vii) reconstructing the MRI image $\mathbf{u}_{\mathrm{MRI}}$ with $\mathbf{u}\frac{\mathrm{est}}{\mathrm{MRI}}$ and the MRI data;

viii) setting $k = k + 1$; and

ix) repeating steps iv) – viii) until meeting stop criteria, at which point the current $\mathbf{u}\frac{\mathrm{est}}{\mathrm{CT}}$ is the reconstructed CT image and the current $\mathbf{u}\frac{\mathrm{est}}{\mathrm{MRI}}$ is the reconstructed MRI image.

43. The method according to claim 42, wherein reconstructing a CT image $\mathbf{u}_{\mathrm{CT}}$ from the CT data comprises using the following equation:

$$\min_{\mathbf{u}_{\mathrm{CT}}} \|\mathbf{u}_{\mathrm{CT}}\|_{\mathrm{TV}} \;\; \mathrm{s.t.}\, \mathbf{M}\mathbf{u}_{\mathrm{CT}} = \mathbf{f} \quad ,$$

where $\mathbf{M}$ is a system matrix, $\mathbf{f}$ is the (line integral) CT data (after preprocessing), and $\|\cdot\|_{TV}$ represents a total variation (TV) transformation.

44. The method according to any of claims 42-43, wherein reconstructing an MRI image $\mathbf{u}_{MRI}$ from the MRI data comprises using the following equation:

$$\min_{\mathbf{u}_{MRI}} \|\mathbf{u}_{MRI}\|_{TV} \quad \text{s.t.} \mathbf{RFu}_{MRI} = \mathbf{g},$$

where $\mathbf{F}$ denotes the Fourier transform, $\mathbf{R}$ is a sampling mask in the k-space, $\mathbf{g}$ is the MRI data, and $\|\cdot\|_{TV}$ represents a total variation (TV) transformation.

45. The method stem according to any of claims 42-44, wherein estimating the corresponded CT-MRI image comprises using a structural coupling (SC) method.

46. The method according to claim 45, wherein the SC method comprises:

a) decomposing $\mathbf{u}_{CT}$ into patches $\mathbf{p}^j_{CT} = \mathbf{E}_j\, \mathbf{u}_{CT}$;

b) decomposing $\mathbf{u}_{MRI}$ into patches $\mathbf{p}^j_{MRI} = \mathbf{E}_j\, \mathbf{u}_{MRI}$;

c) optimizing the following equation by finding K-best suitable patches $\left\{\mathbf{p}^j_{CT,i}\right\}$ and $\left\{\mathbf{p}^j_{MRI,i}\right\}$, and their weights $\{w_i\}$ in $\mathbf{T}_{CT}$ and $\mathbf{T}_{MRI}$ to represent $\mathbf{p}^j_{CT}$ and $\mathbf{p}^j_{MRI}$

$$\min_{\beta_i} \left\| p_{MRI} - \sum_i w_i T_{MRI} \beta_i \right\|_2^2 + \left\| p_{CT} - \sum_i w_i T_{CT} \beta_i \right\|_2^2,$$

where w_i equals the average of CT and MRI weightings calculated according to the below equation, $w_i = (w_{CT,i} + w_{MRI,i})/2$, and β_i identifies surrounding high-dimensional data points,

$$w'_{*,i} = \exp\left(-\left\|\mathbf{p}_* - \mathbf{p}_{*,i}\right\|_2^2 / h^2\right) \text{ and } w_{*,i} = w'_{*,i} / \sum_i^K w'_{*,i},$$

where h is an empirical value that controls contributions of involved patches, and K is the number of surrounding data points;

d) estimating CT and MRI image patches with the corresponded CT and MRI image pairs in $\mathbf{T}_{CT\text{-}MRI}$ and new weights $\{w_i\}$,

$$\mathbf{p}^j_{\mathrm{new,CT}} \approx \sum_i^K w_i \mathbf{p}^j_{\mathrm{CT},i}, \mathbf{p}^j_{\mathrm{new,MRI}} \approx \sum_i^K w_i \mathbf{p}^j_{\mathrm{MRI},i}$$;

e) estimating the corresponded CT image with $\mathbf{p}^j_{\mathrm{new,CT}}$,

$$\mathbf{u}^{est}_{\mathrm{CT}} = \left(\sum_j \mathbf{E}^T_j \mathbf{E}_j\right)^{-1} \left(\sum_j \mathbf{E}^T_j \mathbf{p}^j_{\mathrm{new,CT}}\right)$$; and

f) estimating the corresponded CT image with $\mathbf{p}^j_{\mathrm{new,CT}}$,

$$\mathbf{u}^{est}_{\mathrm{MRI}} = \left(\sum_j \mathbf{E}^T_j \mathbf{E}_j\right)^{-1} \left(\sum_j \mathbf{E}^T_j \mathbf{p}^j_{\mathrm{new,MRI}}\right).$$

47. The method according to any of claims 42-46, wherein reconstructing the CT image $\mathbf{u}_{\mathrm{CT}}$ with $\mathbf{u}^{\mathrm{est}}_{\mathrm{CT}}$ and the CT data comprises using the following equation,

$$\min_{\mathbf{u}_{CT}} (1-\alpha) \left\|\mathbf{u}_{CT}\right\|_{TV} + \alpha \left\|\mathbf{u}_{CT} - \mathbf{u}^{est}_{CT}\right\|_{TV} \text{ s.t.} \mathbf{M}\mathbf{u}_{CT} = \mathbf{f}$$,

where $\mathbf{M}$ is a system matrix, $\mathbf{f}$ is the (line integral) CT data (after preprocessing), α is a relaxation parameter, and $\|\cdot\|_{TV}$ represents a total variation (TV) transformation.

48. The method according to any of claims 42-47, wherein reconstructing the MRI image $\mathbf{u}_{\mathrm{MRI}}$ with $\mathbf{u}^{\mathrm{est}}_{\mathrm{MRI}}$ and the MRI data comprises using the following equation,

$$\min_{\mathbf{u}_{MRI}} (1-\alpha) \left\|\mathbf{u}_{MRI}\right\|_{TV} + \alpha \left\|\mathbf{u}_{MRI} - \mathbf{u}^{est}_{MRI}\right\|_{TV}$$
$$\text{s.t.} \mathbf{F}\mathbf{u}_{MRI} = \mathbf{g}$$,

where $\mathbf{F}$ denotes the Fourier transform, $\mathbf{R}$ is a sampling mask in the k-space, $\mathbf{g}$ is the MRI data, α is a relaxation parameter, and $\|\cdot\|_{TV}$ represents a total variation (TV) transformation.

49. The method according to any of claims 42-48, wherein steps iv) through vii) can be formulated as follows,

$$\min_{(\mathbf{u}_{CT},\mathbf{u}_{MRI},\beta)} \|\mathbf{u}_{CT}\|_{TV} + \lambda\|\mathbf{u}_{MRI}\|_{TV} + \gamma\sum_j \left(\left\|\mathbf{E}_j\mathbf{u}_{MRI} - \sum_i w_i\mathbf{T}_{MRI}\beta_{j,i}\right\|_2^2 + \left\|\mathbf{E}_j\mathbf{u}_{CT} - \sum_i w_i\mathbf{T}_{CT}\beta_{j,i}\right\|_2^2\right)$$

$$\text{s.t.}\,\mathbf{M}\mathbf{u}_{CT} = \mathbf{f},\quad \mathbf{R}\mathbf{F}\mathbf{u}_{MRI} = \mathbf{g},$$

where **E** is an operator to extract patches from an image, β determines which patch is selected for linear approximation by assigning appropriate weighting factors $\{w_i\}$, **M** is a system matrix, **f** is the (line integral) CT data (after preprocessing), **F** denotes the Fourier transform, **R** is a sampling mask in the k-space, **g** is the MRI data, and $\|\cdot\|_{TV}$ represents a total variation (TV) transformation.

50. The method according to any of claims 42-49, wherein estimating the corresponded CT-MRI image comprises using an SC method implemented using a hashing method to accelerate the patch searching process.

51. The method according to any of claims 42-50, wherein the method of reconstructing CT and MRI images further comprises utilizing prior knowledge of CT images.

52. The method according to claim 51, wherein the prior knowledge of CT images comprises information from a CT image atlas.

53. The method according to any of claims 51-52, wherein the prior knowledge of CT images is utilized in step i).

54. The method according to any of claims 42-53, wherein the method of reconstructing CT and MRI images further comprises utilizing prior knowledge of MRI images.

55. The method according to claim 54, wherein the prior knowledge of MRI images comprises information from an MRI image atlas.

56. The method according to any of claims 54-55, wherein the prior knowledge of MRI images is utilized in step i).

57. The method according to any of claims 42-56, wherein the CT data comprises only a few-view set of CT data.

58. The method according to any of claims 42-57, wherein the method of reconstructing CT and MRI images comprises using an SC method and a compressive sensing (CS) method.

59. A system for simultaneous computed tomography (CT)-magnetic resonance imaging (MRI), the system comprising:

a CT subsystem for obtaining CT data;

an MRI subsystem for obtaining MRI data;

at least one processor; and

a machine-readable medium, in operable communication with the CT subsystem, the MRI subsystem, and the at least one processor, having machine-executable instructions stored thereon that, when executed by the at least one processor, perform a method of reconstructing CT and MRI images,

wherein the MRI subsystem comprises superconducting magnets.

60. The system according claim 59, wherein the superconducting magnets are room temperature superconducting magnets.

61. The system according to any of claims 59-60, wherein the MRI subsystem comprises two donut shaped magnets facing each other.

62. The system according to any of claims 59-61, wherein the MRI subsystem comprises two hexagonal magnet arrays facing each other.

63. The system according to any of claims 59-62, wherein the CT subsystem and the MRI subsystem are seamlessly integrated with one another.

64. The system according to any of claims 59-63, wherein components of the CT subsystem are quasi-stationary.

65. The system according to claim 64, wherein X-ray sources and detectors of the CT subsystem are distributed face-to-face along a circle.

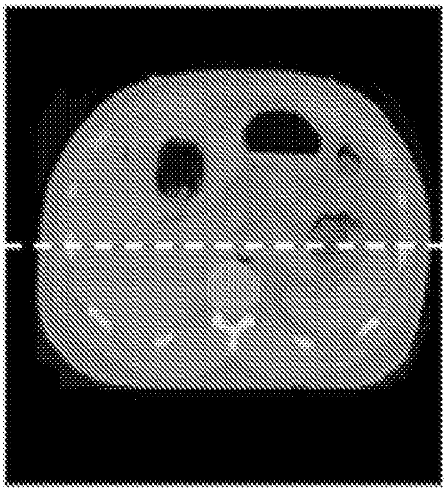

Fig. 1a

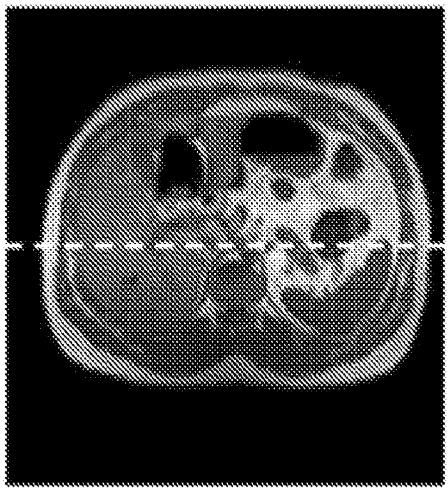

Fig. 1b

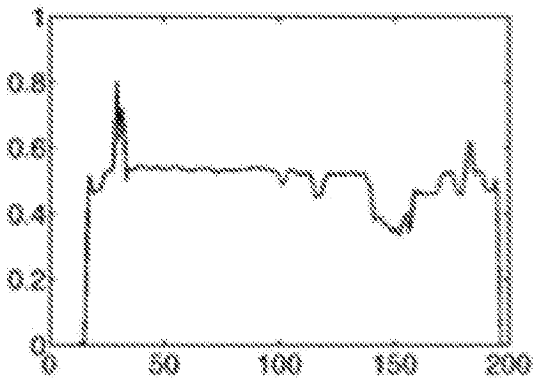

Fig. 1c

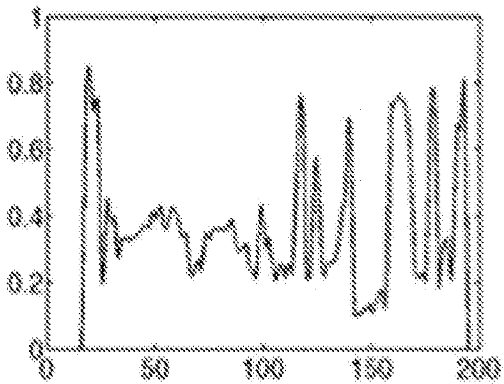

Fig. 1d

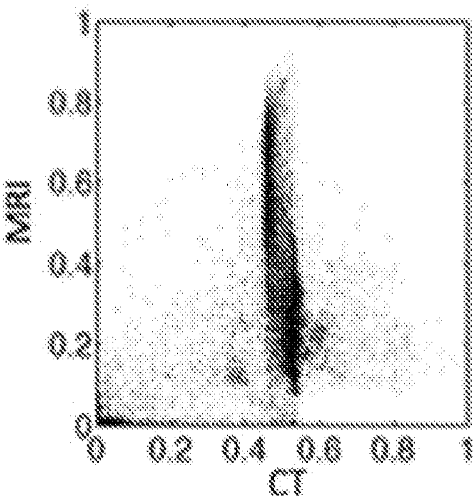

Fig. 1e

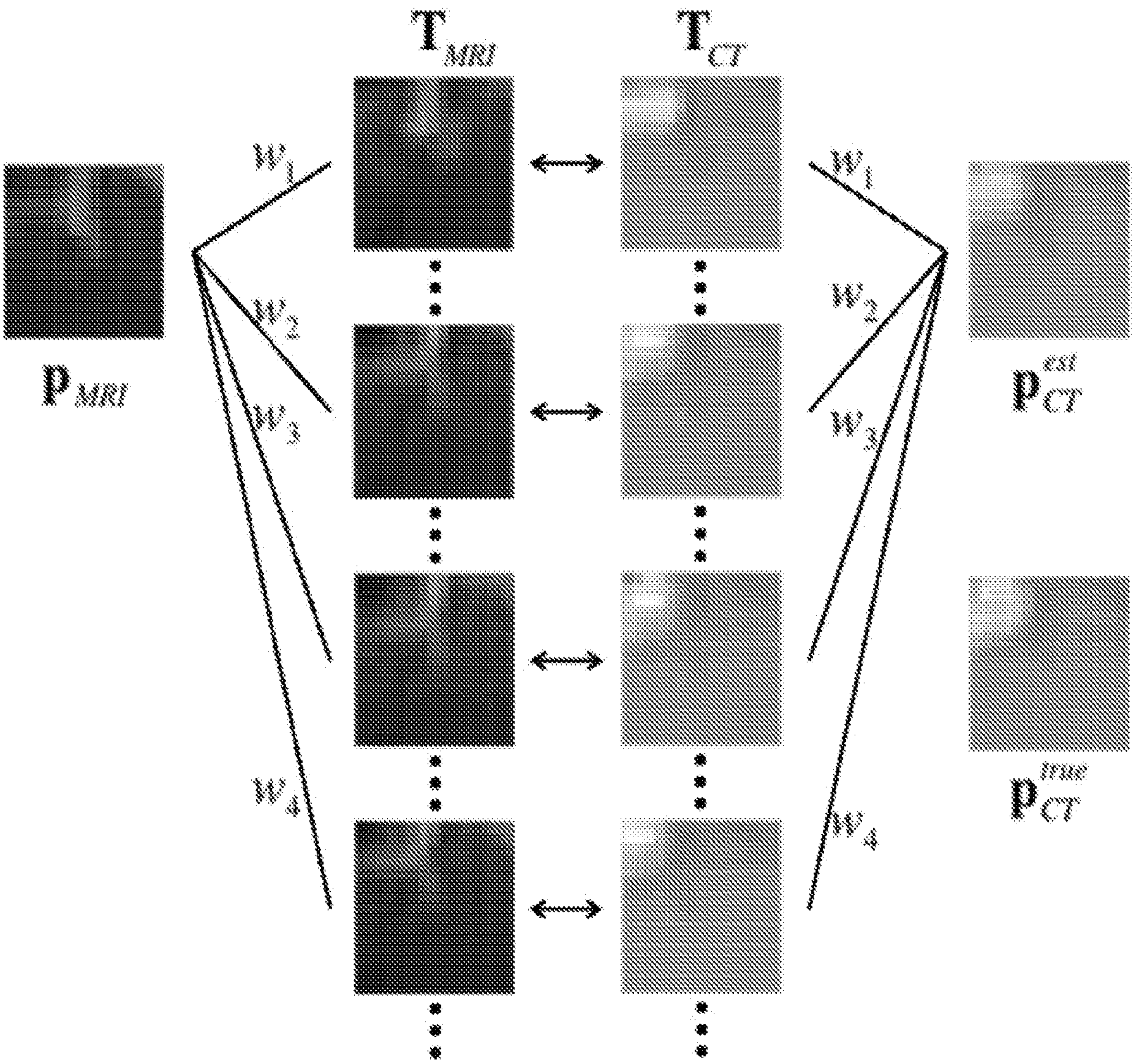
$\mathbf{T}_{MRI}$
$\mathbf{T}_{CT}$
w_1
w_2
w_3
w_4
w_1
w_2
w_3
w_4
$\mathbf{p}_{MRI}$
$\mathbf{p}_{CT}^{est}$
$\mathbf{p}_{CT}^{true}$

FIG. 2

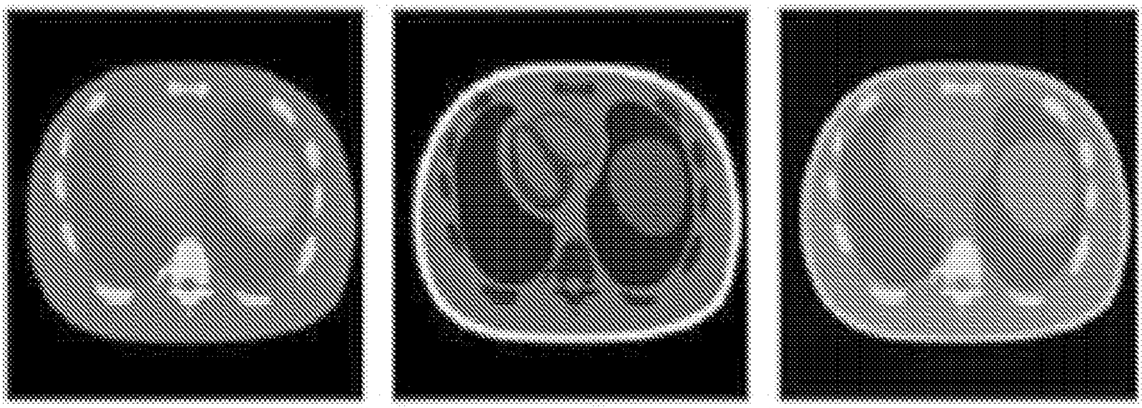

FIG. 3a

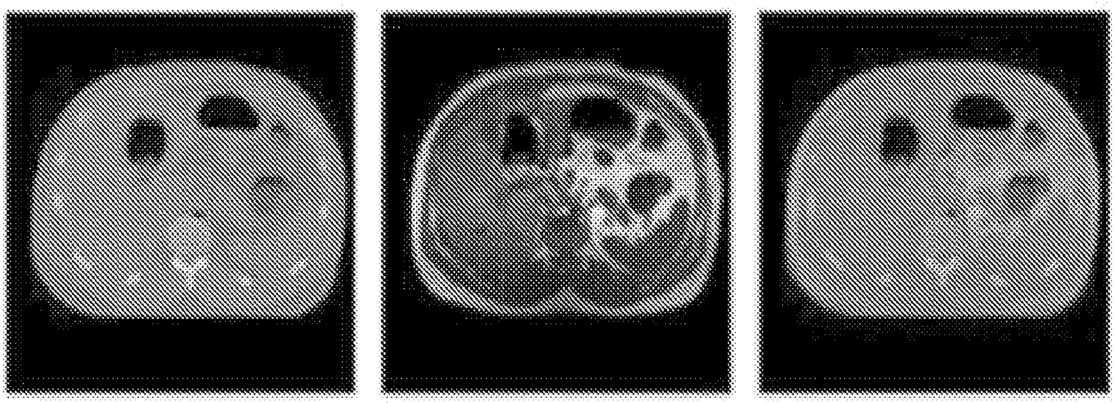

FIG. 3b

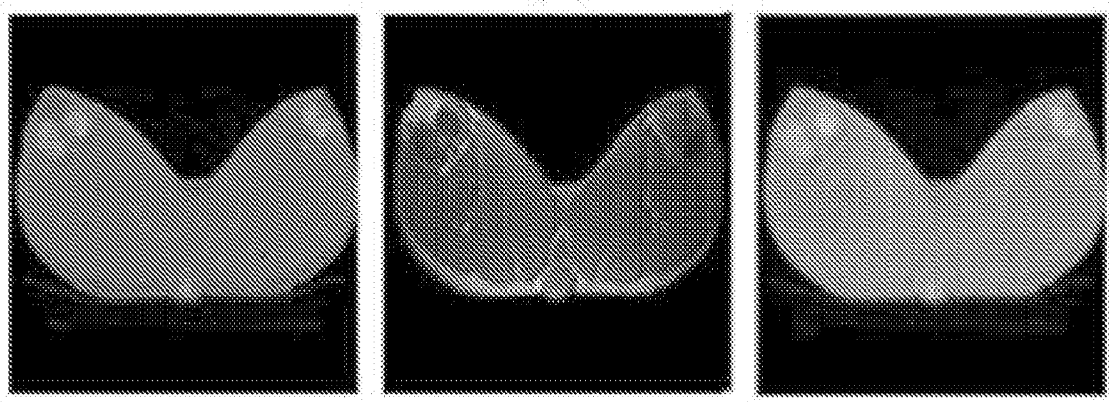

FIG. 3c

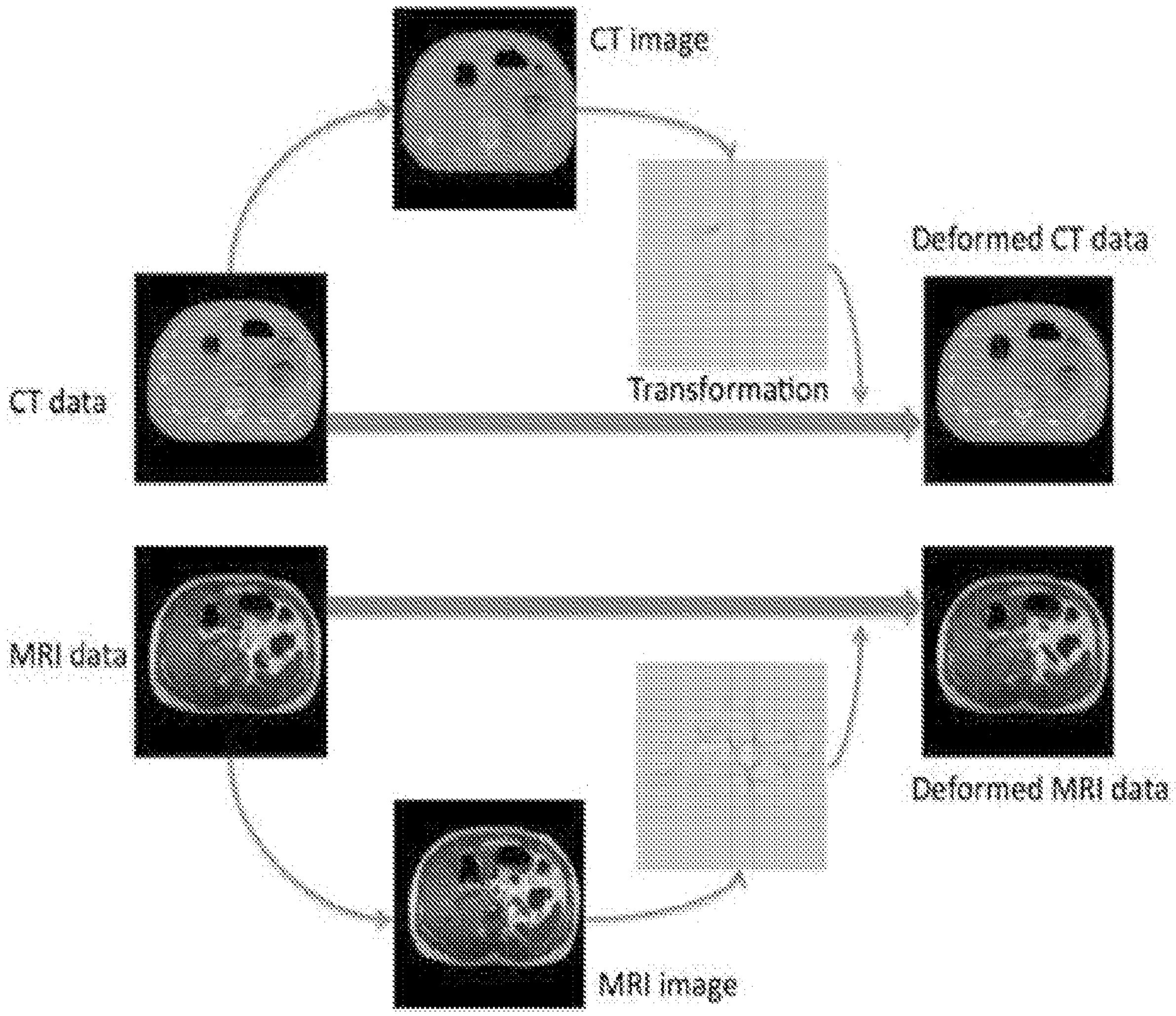
CT image
Deformed CT data
CT data
Transformation
MRI data
Deformed MRI data
MRI image

FIG. 4

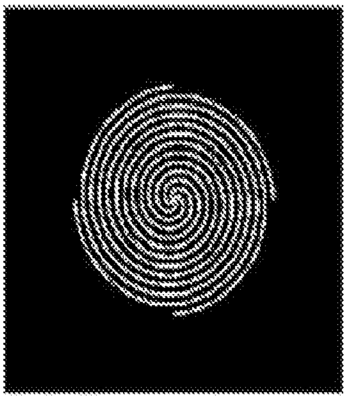
Fig. 5a

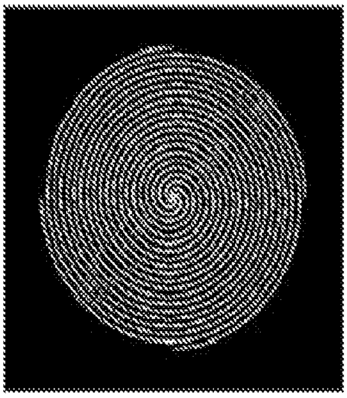
Fig. 5b

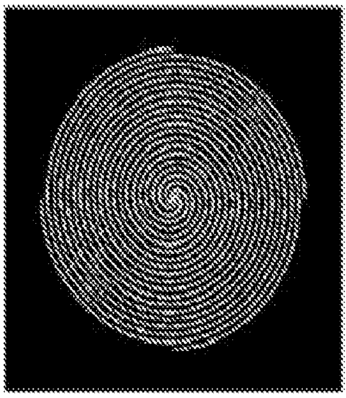
Fig. 5c

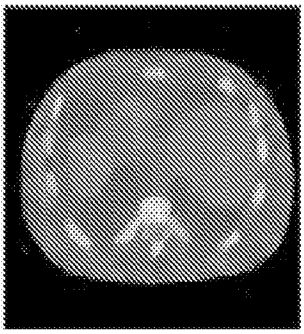
Fig. 6a

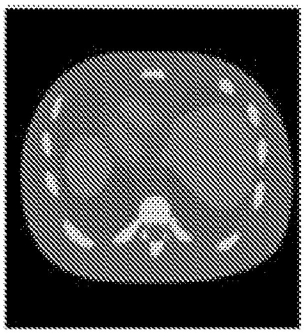
Fig. 6b

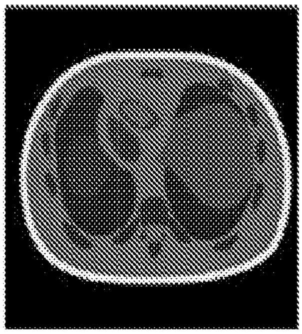
Fig. 6c

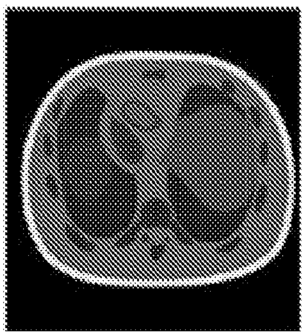
Fig. 6d

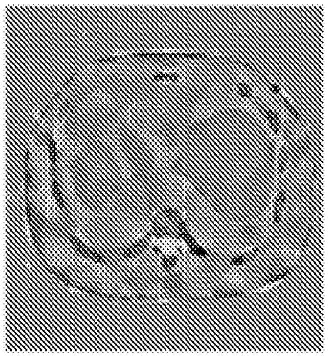
Fig. 6e

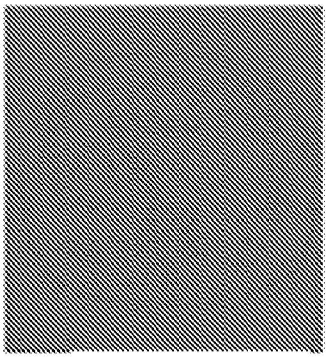
Fig. 6f

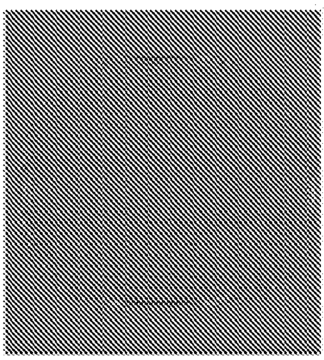
Fig. 6g

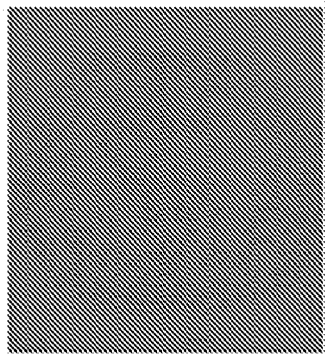
Fig. 6h

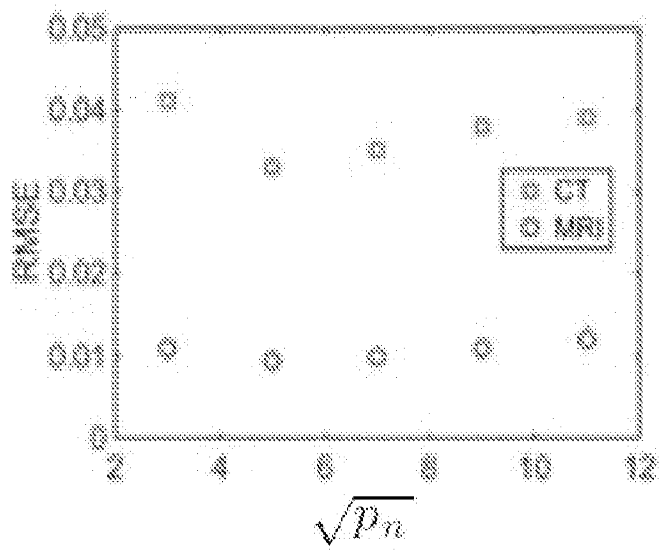

Fig. 7a

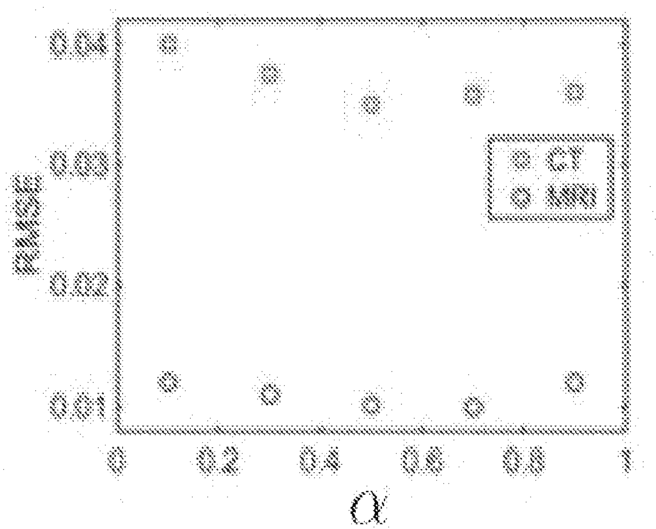

Fig. 7b

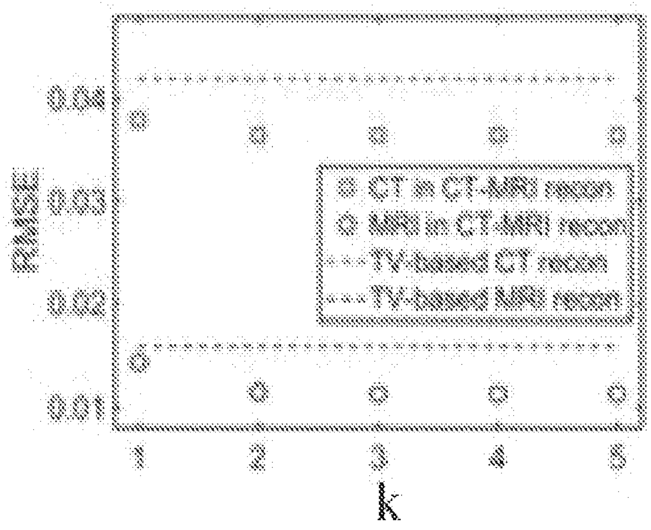

Fig. 7c

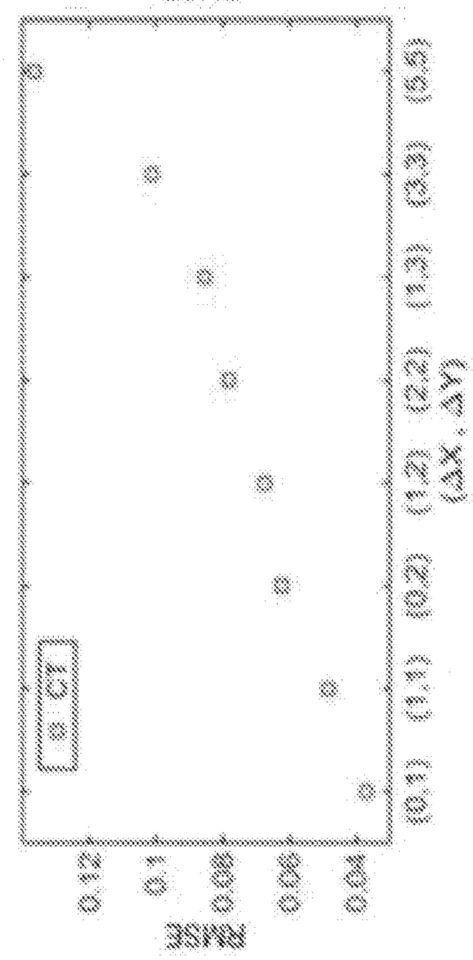

FIG. 8a

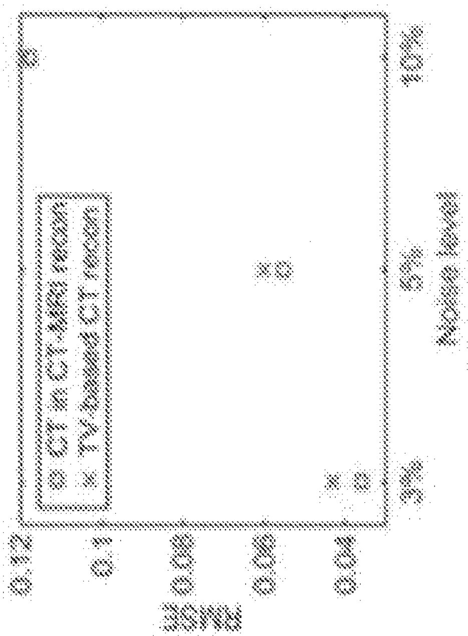

FIG. 8b

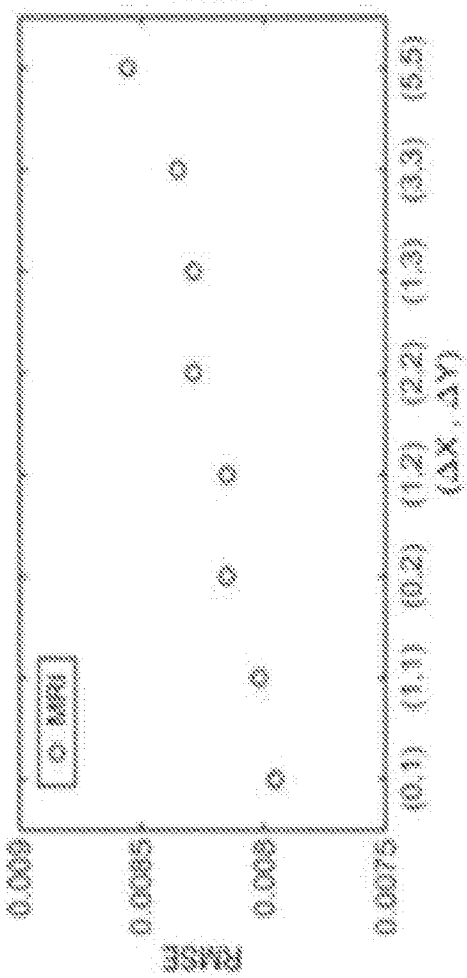

FIG. 8c

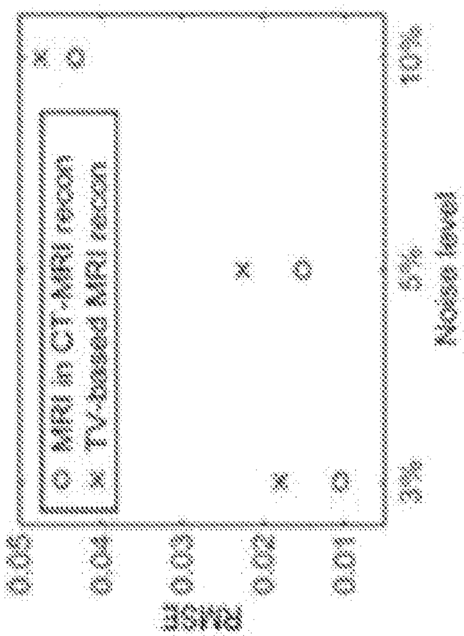

FIG. 8d

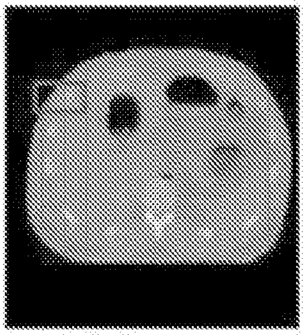
FIG. 9a

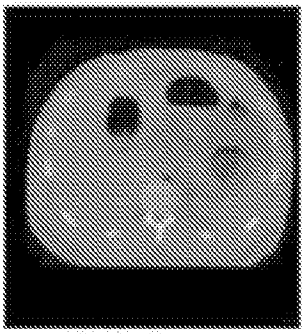
FIG. 9b

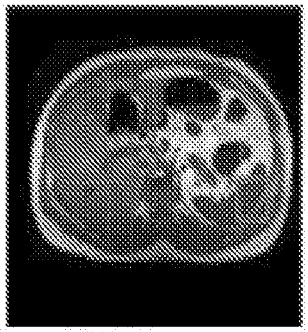
FIG. 9c

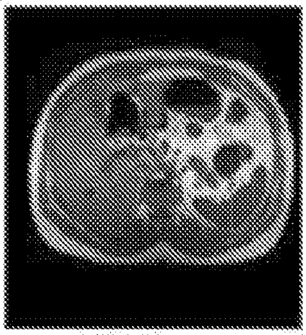
FIG. 9d

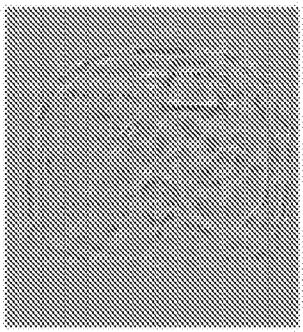
FIG. 9e

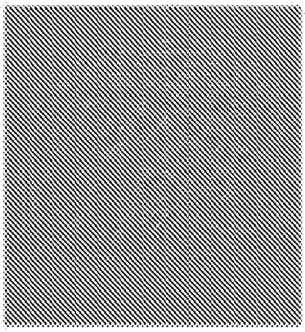
FIG. 9f

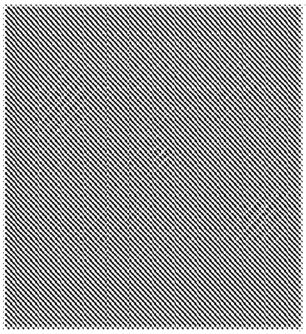
FIG. 9g

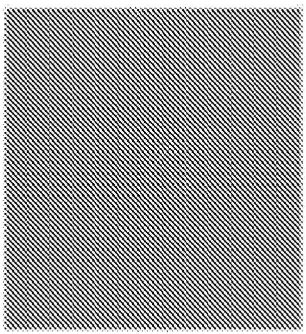
FIG. 9h

CT

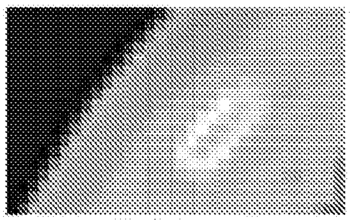
FIG. 10a

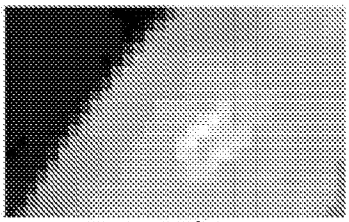
FIG. 10b

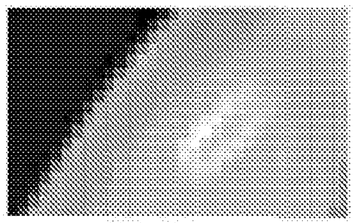
FIG. 10c

MRI

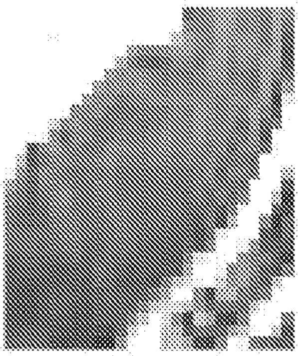
FIG. 10d

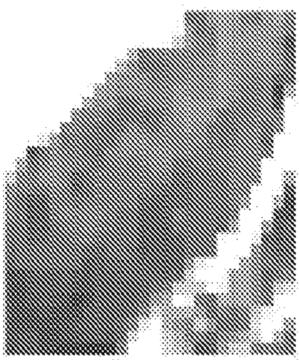
FIG. 10e

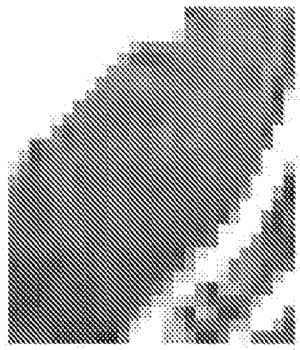
FIG. 10f

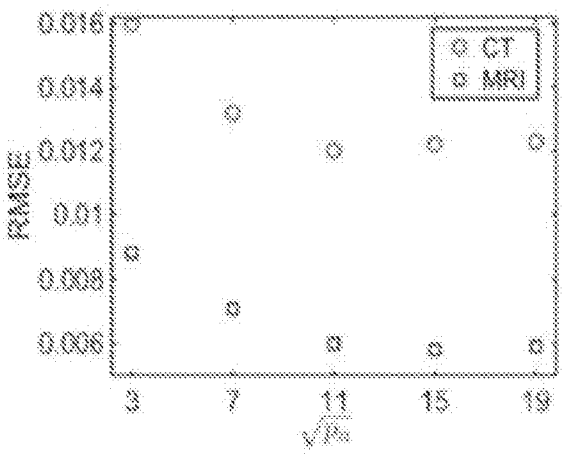

FIG. 11a

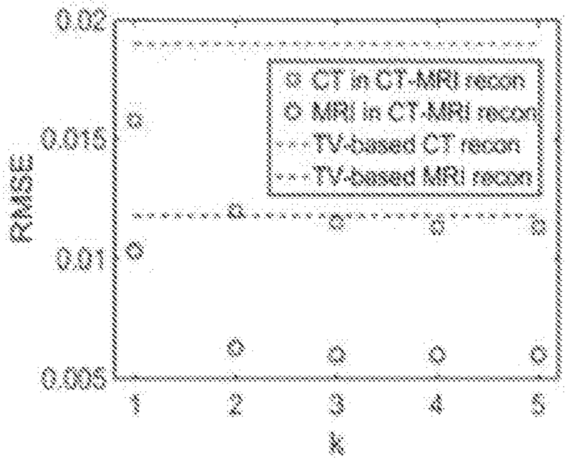

FIG. 11b


FIG. 12a


FIG. 12b

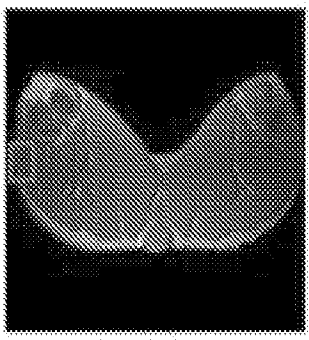
FIG. 12c

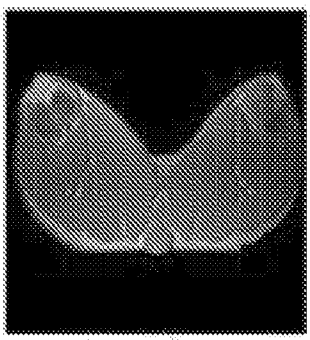
FIG. 12d

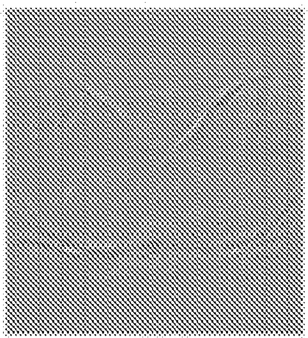
FIG. 12e

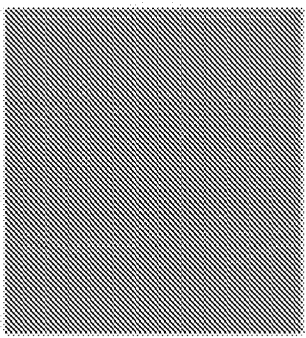
FIG. 12f

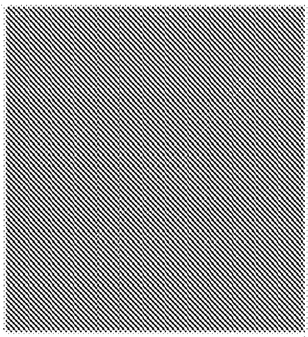
FIG. 12g

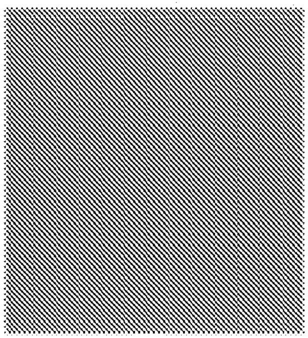
FIG. 12h

CT

FIG. 13a
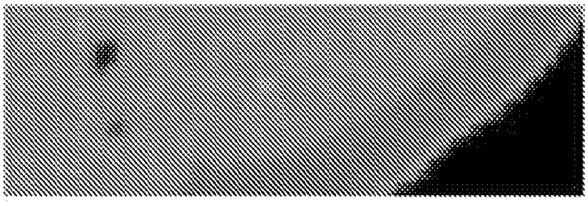

FIG. 13b
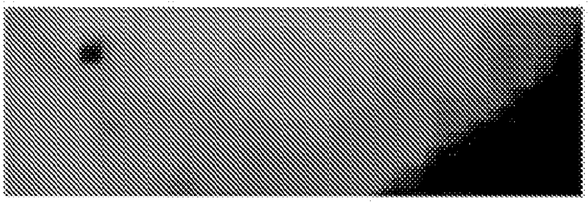

FIG. 13c
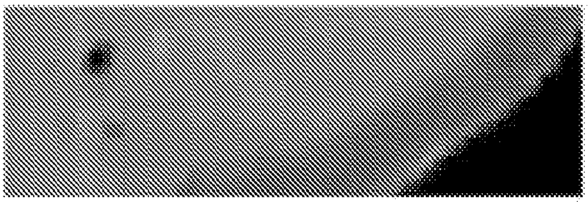

MRI

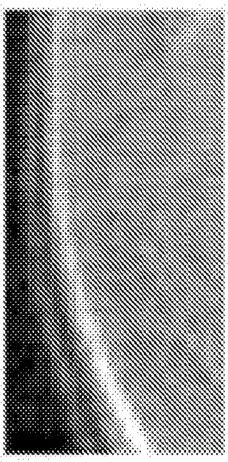
FIG. 13d

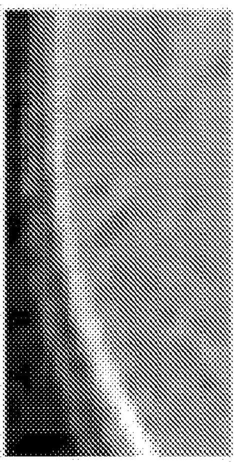
FIG. 13e

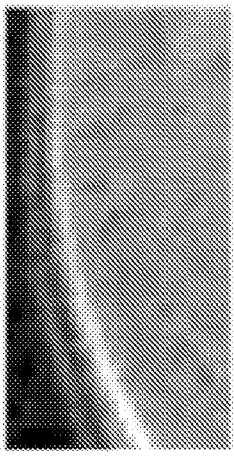
FIG. 13f

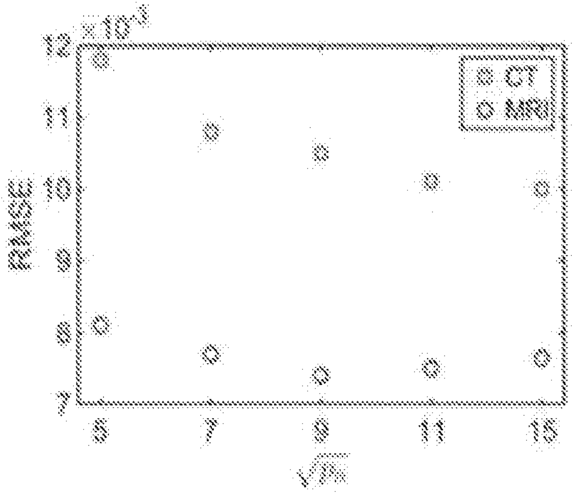

FIG. 14a

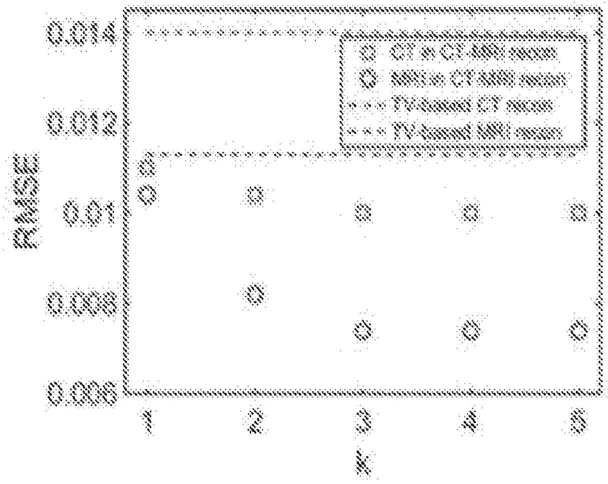

FIG. 14b

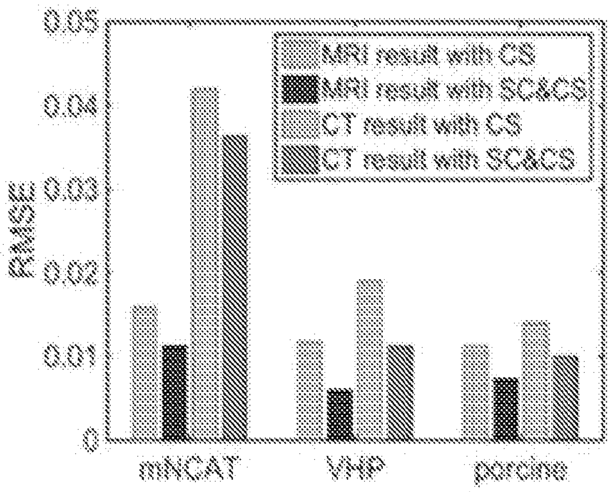

FIG. 15a

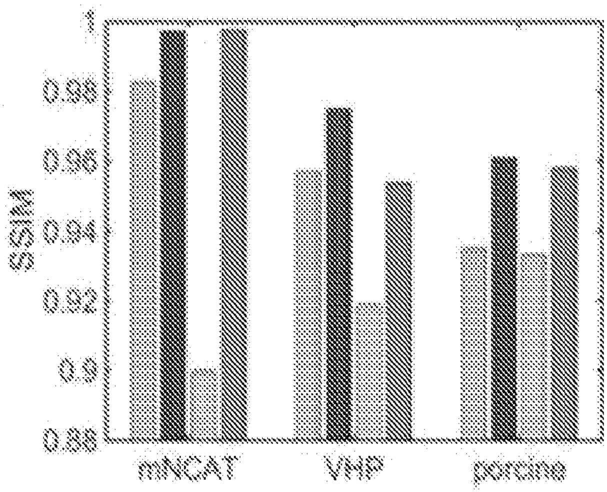

FIG. 15b

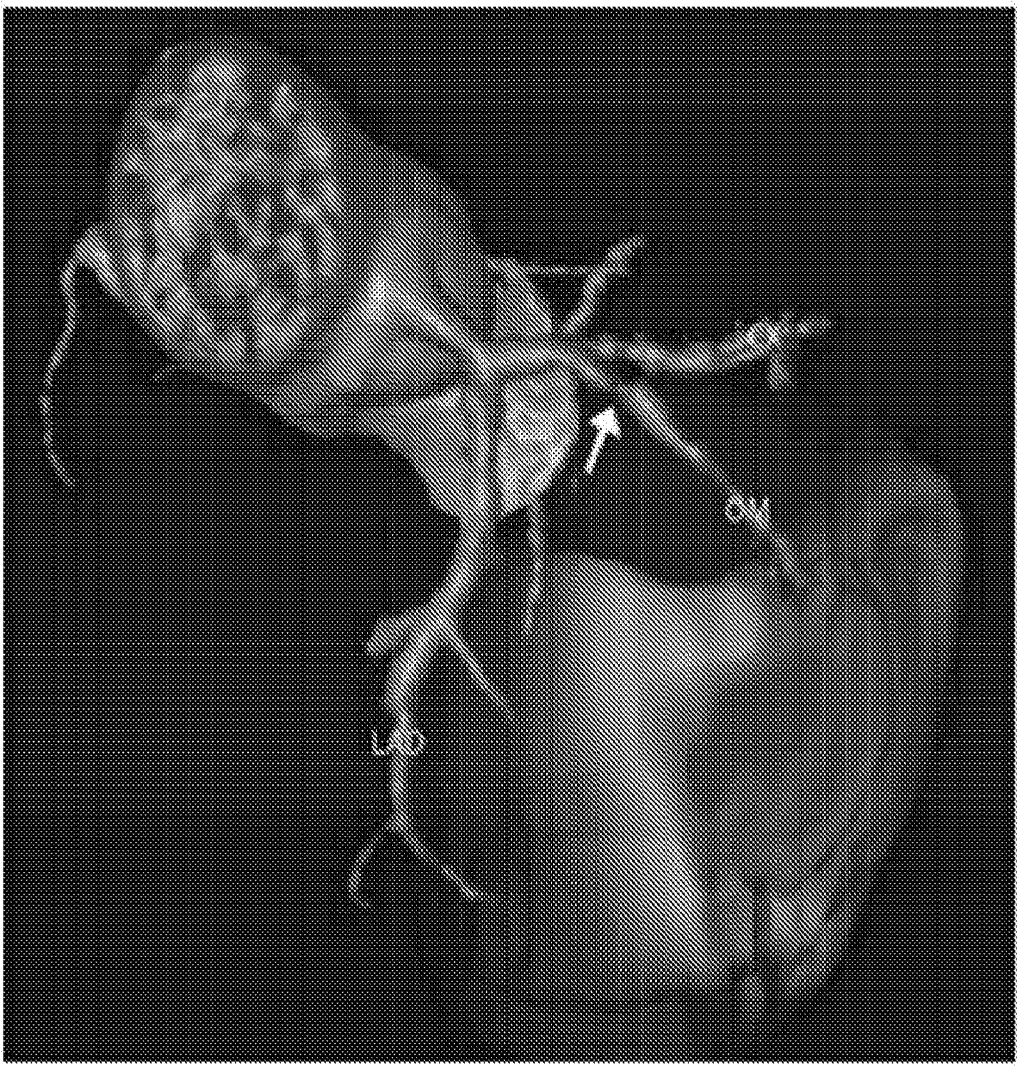

FIG. 16a

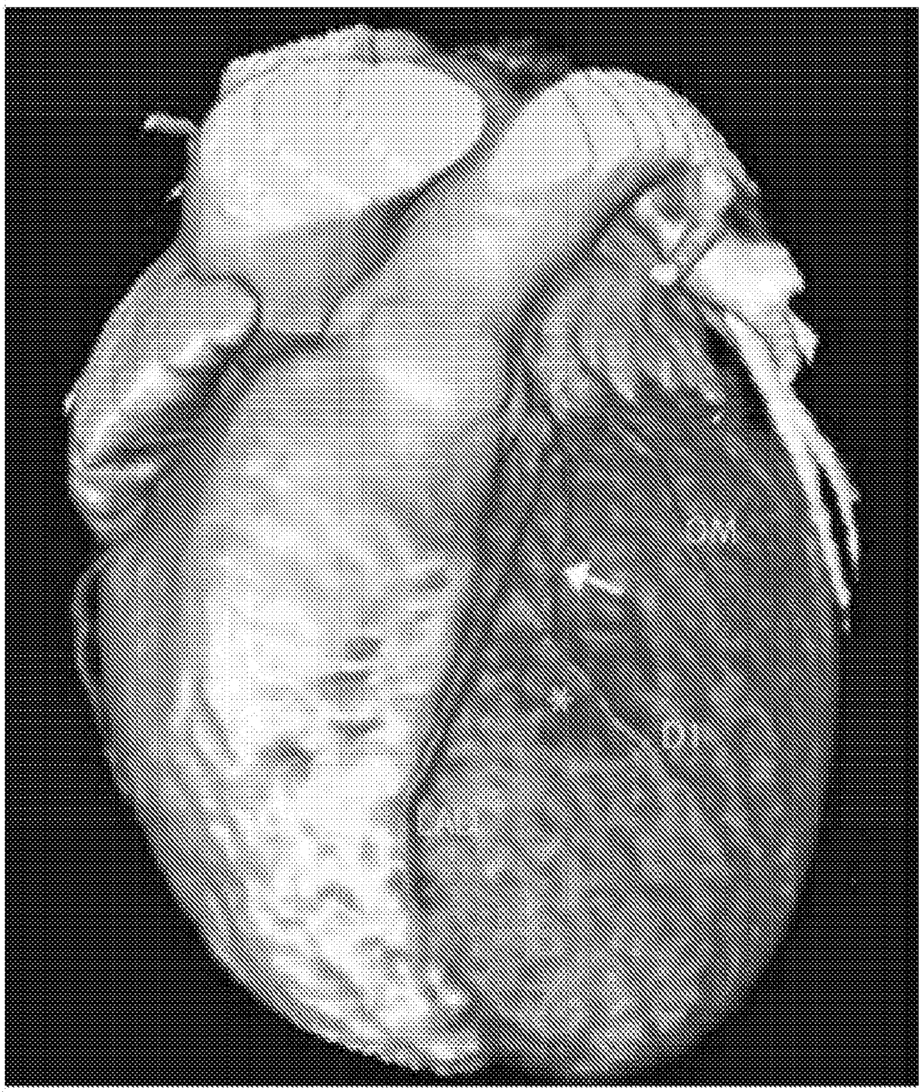

FIG. 16b

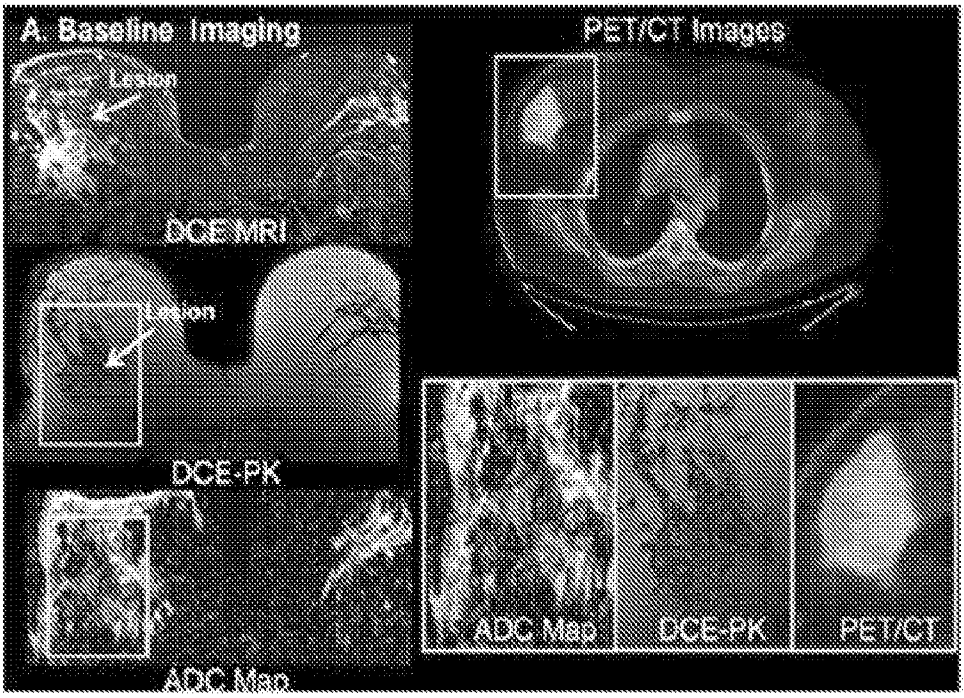

FIG. 17a

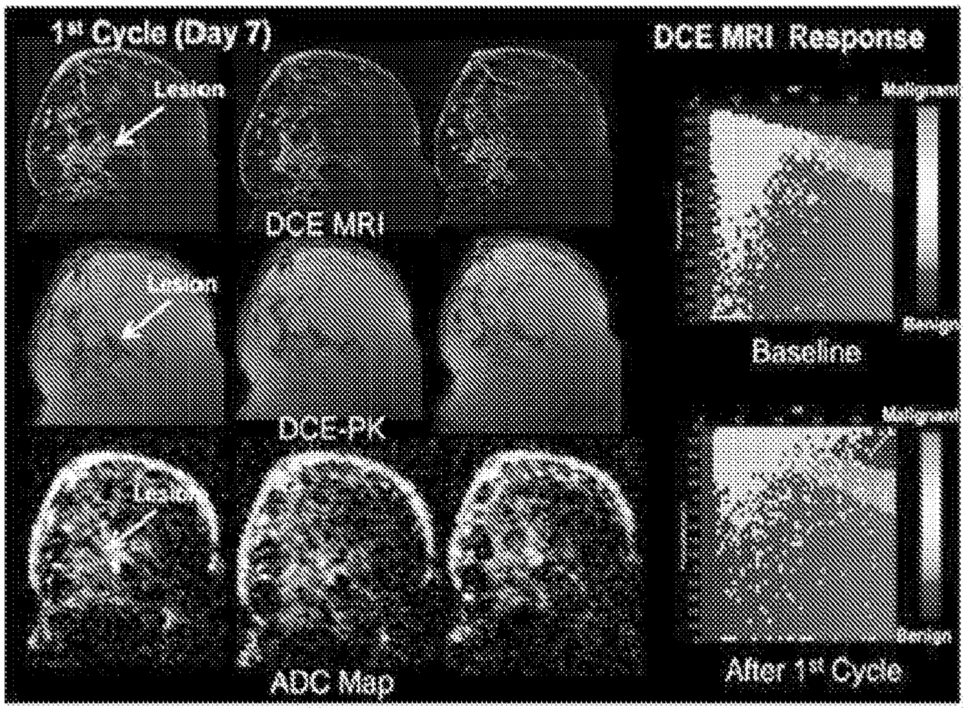

FIG. 17b

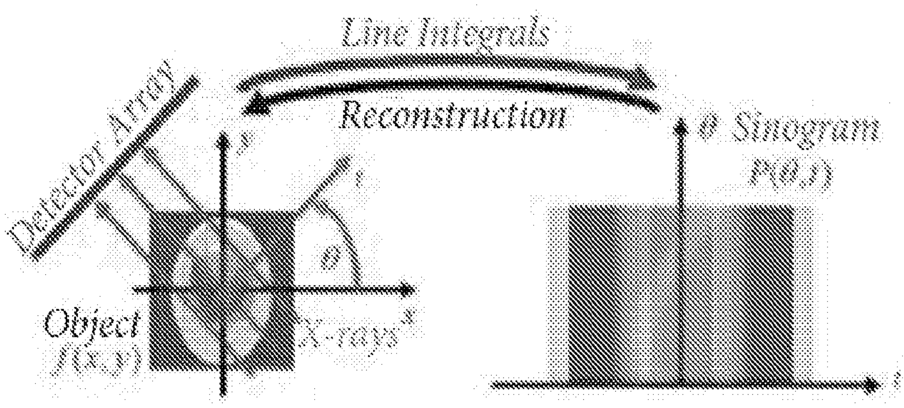

FIG. 18a

FIG. 18b

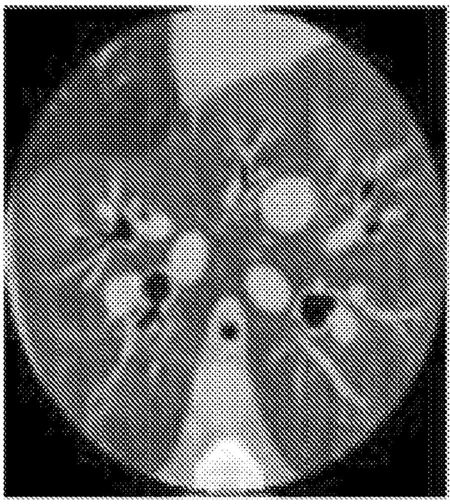

FIG. 18c

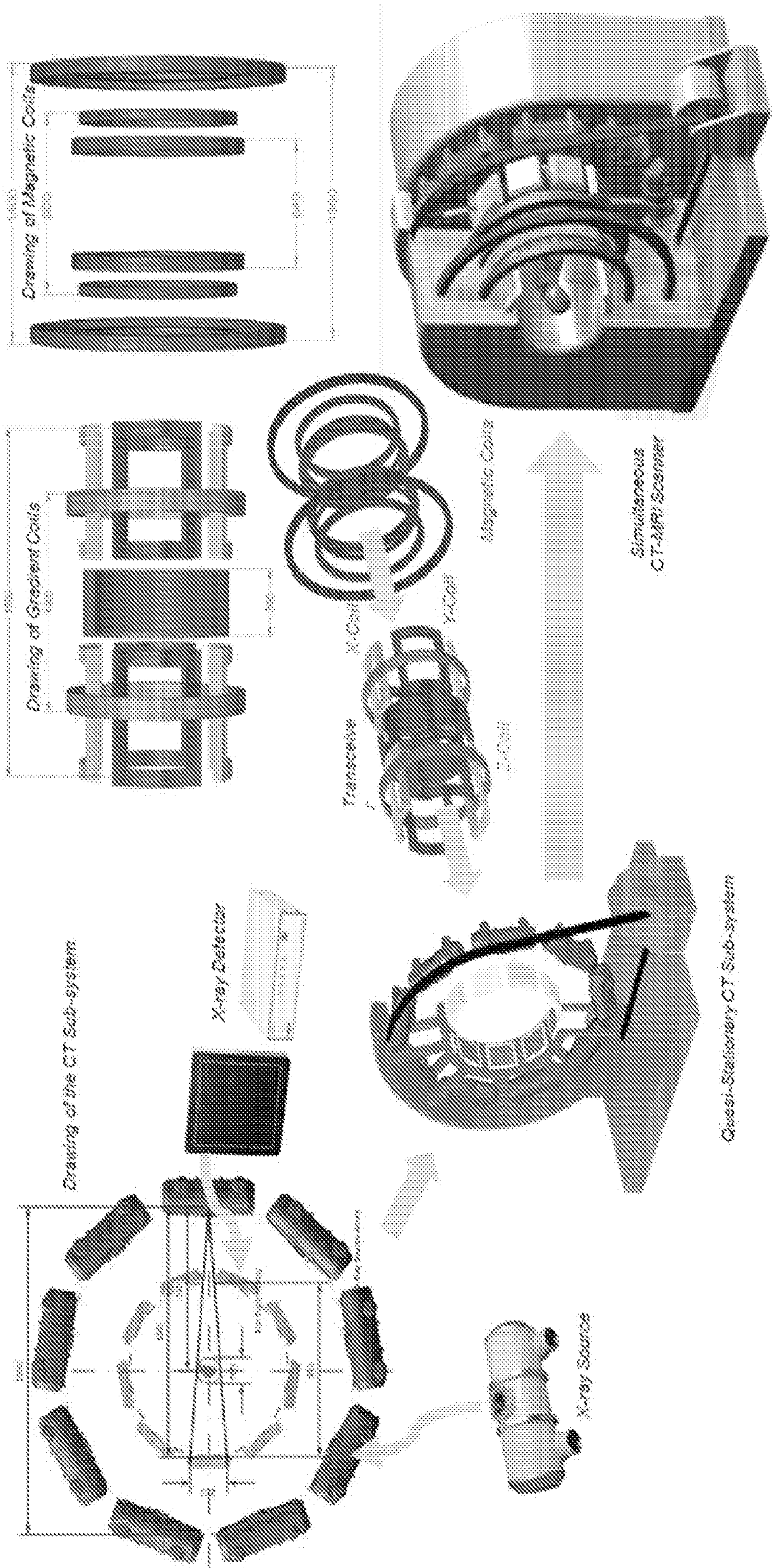
Drawing of Magnetic Coils
Drawing of Gradient Coils
Magnetic Coils
Simultaneous CT-MRI Scanner
X-Coil
Y-Coil
Z-Coil
Drawing of the CT Sub-system
X-ray Detector
Quasi-Stationary CT Sub-system
X-ray Source

FIG. 19

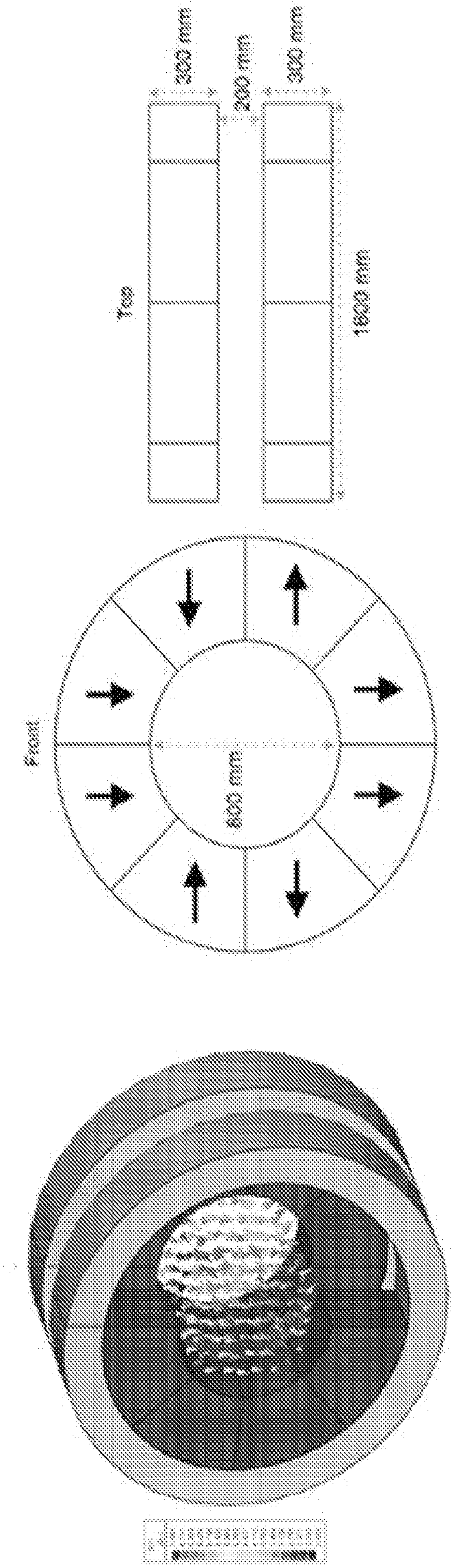

FIG. 20a

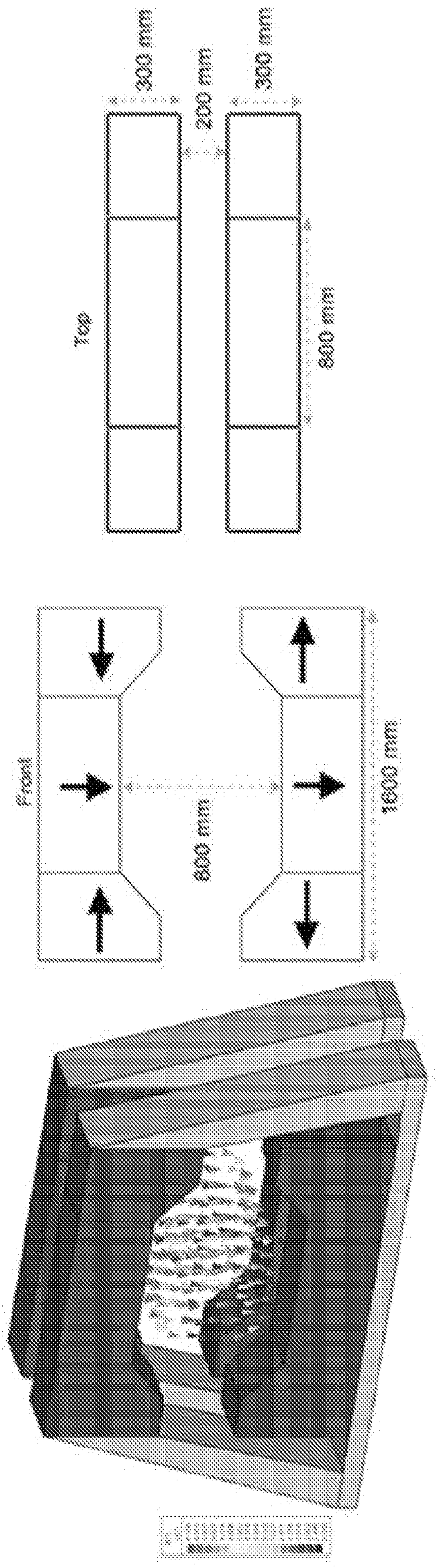

FIG. 20b

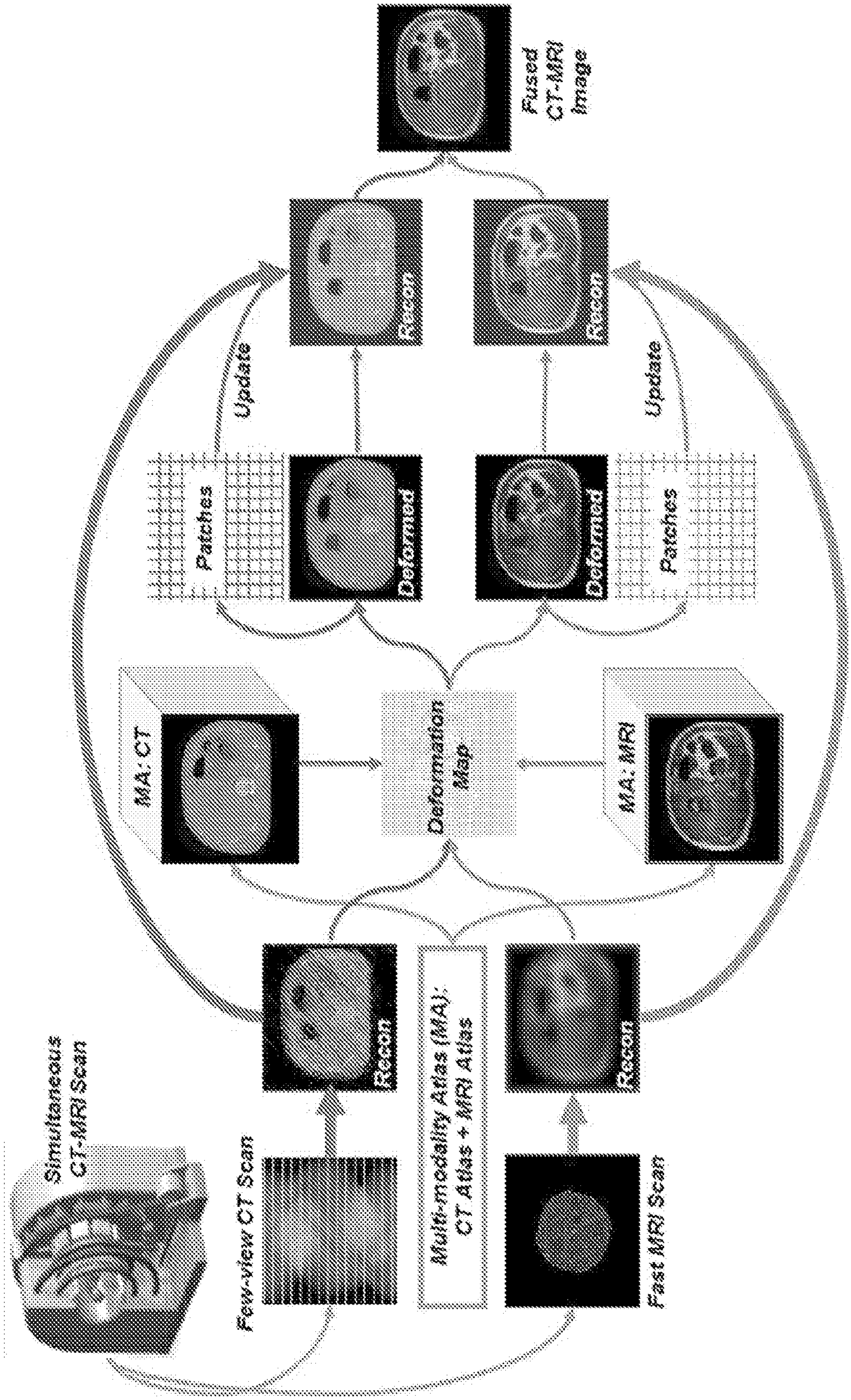
Simultaneous CT-MRI Scan
Few-view CT Scan
Multi-modality Atlas (MA): CT Atlas + MRI Atlas
Fast MRI Scan
Recon
Recon
MA: CT
Deformation Map
MA: MRI
Patches
Deformed
Deformed
Patches
Update
Update
Recon
Recon
Fused CT-MRI Image

FIG. 21

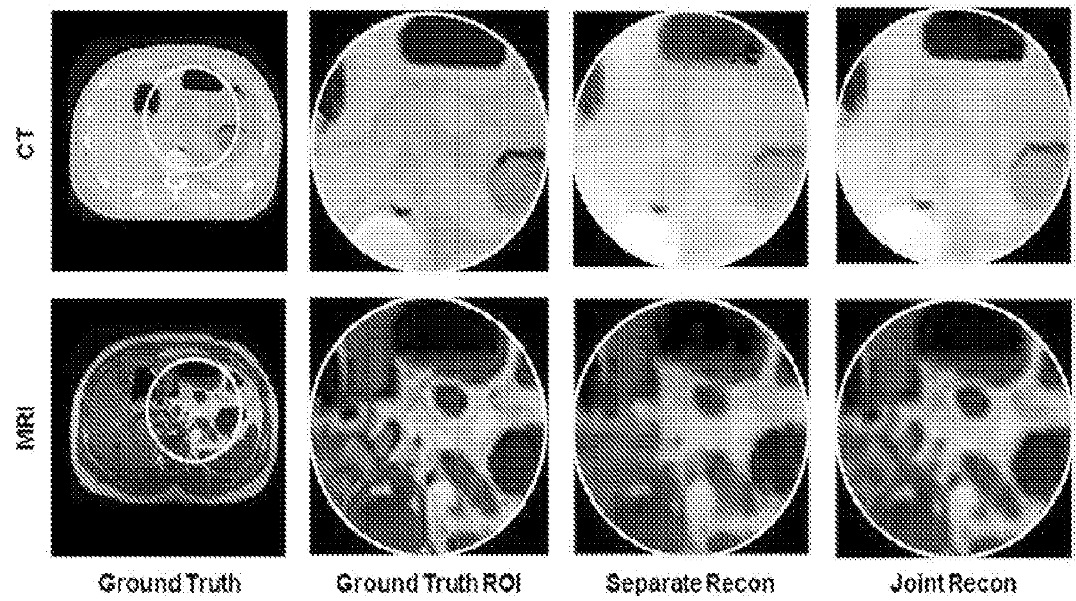
CT
MRI
Ground Truth
Ground Truth ROI
Separate Recon
Joint Recon

FIG. 22

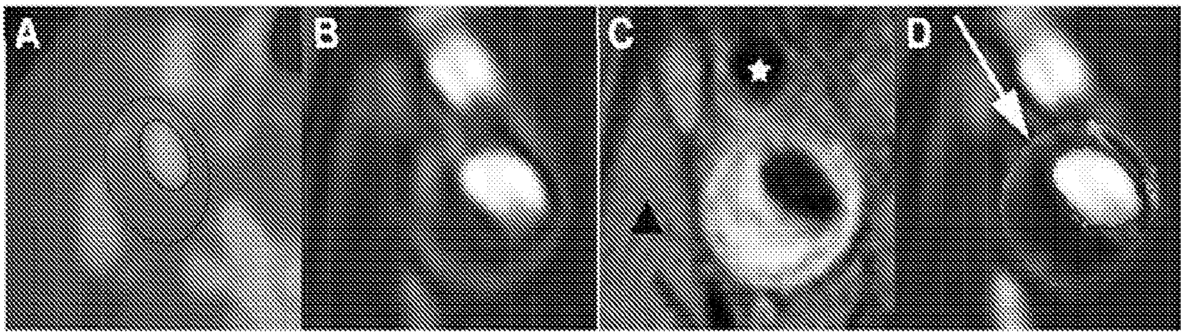
A
B
C
D

FIG. 23

INTERNATIONAL SEARCH REPORT

International application No.
PCT/US2016/051755

A. CLASSIFICATION OF SUBJECT MATTER

A61B 5/00(2006.01)i, A61B 6/03(2006.01)i, A61B 5/055(2006.01)i

According to International Patent Classification (IPC) or to both national classification and IPC

B. FIELDS SEARCHED

Minimum documentation searched (classification system followed by classification symbols)
A61B 5/00; G06K 9/36; G06T 11/00; A61B 6/03; A61B 6/00; G01R 33/44; G06T 7/00; A61B 5/055

Documentation searched other than minimum documentation to the extent that such documents are included in the fields searched
Korean utility models and applications for utility models
Japanese utility models and applications for utility models

Electronic data base consulted during the international search (name of data base and, where practicable, search terms used)
eKOMPASS(KIPO internal) & Keywords: CT, MRI, image, superconducting magnet

C. DOCUMENTS CONSIDERED TO BE RELEVANT

Category*	Citation of document, with indication, where appropriate, of the relevant passages	Relevant to claim No.
Y A	WO 2015-081079 A1 (HENRY FORD INNOVATION INSTITUTE) 04 June 2015 See abstract, paragraphs [29]-[57], claims 1-9 and figures 6,7.	59-61 1-3,22,25-27,42-44
Y	US 2015-0230766 A1 (WANG et al.) 20 August 2015 See abstract, paragraphs [85]-[99] and figures 9A-10B.	59-61
Y	US 2012-0098538 A1 (SHEN et al.) 26 April 2012 See abstract, paragraph [30] and figure 3.	60
A	US 2015-0092907 A1 (GE MEDICAL SYSTEMS GLOBAL TECHNOLOGY CO. LLC) 02 April 2015 See abstract, paragraphs [21]-[37],[51],[53] and figures 1-3.	1-3,22,25-27,42-44,59-61
A	US 2011-0116724 A1 (BILGIN et al.) 19 May 2011 See abstract, paragraphs [54]-[57], claims 1-4,10,11 and figure 2.	1-3,22,25-27,42-44,59-61

☐ Further documents are listed in the continuation of Box C.

☒ See patent family annex.

* Special categories of cited documents:
"A" document defining the general state of the art which is not considered to be of particular relevance
"E" earlier application or patent but published on or after the international filing date
"L" document which may throw doubts on priority claim(s) or which is cited to establish the publication date of another citation or other special reason (as specified)
"O" document referring to an oral disclosure, use, exhibition or other means
"P" document published prior to the international filing date but later than the priority date claimed
"T" later document published after the international filing date or priority date and not in conflict with the application but cited to understand the principle or theory underlying the invention
"X" document of particular relevance; the claimed invention cannot be considered novel or cannot be considered to involve an inventive step when the document is taken alone
"Y" document of particular relevance; the claimed invention cannot be considered to involve an inventive step when the document is combined with one or more other such documents,such combination being obvious to a person skilled in the art
"&" document member of the same patent family

Date of the actual completion of the international search
27 December 2016 (27.12.2016)

Date of mailing of the international search report
27 December 2016 (27.12.2016)

Name and mailing address of the ISA/KR
International Application Division
Korean Intellectual Property Office
189 Cheongsa-ro, Seo-gu, Daejeon, 35208, Republic of Korea
Facsimile No. +82-42-481-8578

Authorized officer
KIM, Yeon Kyung
Telephone No. +82-42-481-3325

INTERNATIONAL SEARCH REPORT

International application No.
PCT/US2016/051755

Box No. II Observations where certain claims were found unsearchable (Continuation of item 2 of first sheet)

This international search report has not been established in respect of certain claims under Article 17(2)(a) for the following reasons:

1. ☐ Claims Nos.:
because they relate to subject matter not required to be searched by this Authority, namely:

2. ☒ Claims Nos.: 5,11,14,17,29,35,38,46,52,55,65
because they relate to parts of the international application that do not comply with the prescribed requirements to such an extent that no meaningful international search can be carried out, specifically:
Claims 5, 11, 14, 17, 29, 35, 38, 46, 52, 55, 65 are unclear, because they refer to multiple dependent claims which do not comply with PCT Rule 6.4(a).

3. ☒ Claims Nos.: 4,6-10,12,13,15,16,18-21,23,24,28,30-34,36,37,39-41,45,47-51,53,54,56-58,62-64
because they are dependent claims and are not drafted in accordance with the second and third sentences of Rule 6.4(a).

Box No. III Observations where unity of invention is lacking (Continuation of item 3 of first sheet)

This International Searching Authority found multiple inventions in this international application, as follows:

1. ☐ As all required addtional search fees were timely paid by the applicant, this international search report covers all searchable claims.

2. ☐ As all searchable claims could be searched without effort justifying an additional fees, this Authority did not invite payment of any additional fees.

3. ☐ As only some of the required additional search fees were timely paid by the applicant, this international search report covers only those claims for which fees were paid, specifically claims Nos.:

4. ☐ No required additional search fees were timely paid by the applicant. Consequently, this international search report is restricted to the invention first mentioned in the claims; it is covered by claims Nos.:

Remark on Protest

☐ The additional search fees were accompanied by the applicant's protest and, where applicable, the payment of a protest fee.

☐ The additional search fees were accompanied by the applicant's protest but the applicable protest fee was not paid within the time limit specified in the invitation.

☐ No protest accompanied the payment of additional search fees.

Patent document cited in search report	Publication date	Patent family member(s)	Publication date
WO 2015-081079 A1	04/06/2015	None	
US 2015-0230766 A1	20/08/2015	WO 2014-047518 A1	27/03/2014
US 2012-0098538 A1	26/04/2012	CN 102456460 A	16/05/2012
		CN 102456460 B	06/07/2016
		GB 2484788 A	25/04/2012
		GB 2484788 B	29/06/2016
		US 8604793 B2	10/12/2013
US 2015-0092907 A1	02/04/2015	CN 104517263 A	15/04/2015
		JP 2015-066445 A	13/04/2015
		US 9443295 B2	13/09/2016
US 2011-0116724 A1	19/05/2011	US 8760572 B2	24/06/2014